

**UNIVERSIDADE DE SÃO PAULO
INSTITUTO DE FÍSICA DE SÃO CARLOS**

Vinicius Massami Mikuni

**Measurement of cosmic ray electrons and positrons with
the AMS-02 experiment.**

São Carlos

2017

Vinicius Massami Mikuni

**Measurement of cosmic ray electrons and positrons with
the AMS-02 experiment.**

Dissertation presented to the Graduate Program in Physics at the Instituto de Física de São Carlos, Universidade de São Paulo, to obtain the degree of Master in Science.

Concentration area: Basic Physics

Advisor: Prof. Dr. Manuela Vecchi

Corrected Version
(Original version available on the Program Unit)

São Carlos
2017

I AUTHORIZE THE REPRODUCTION AND DISSEMINATION OF TOTAL OR PARTIAL COPIES OF THIS DOCUMENT, BY CONVENCIONAL OR ELECTRONIC MEDIA FOR STUDY OR RESEARCH PURPOSE, SINCE IT IS REFERENCED.

Cataloguing data revised by the Library and Information Service
of the IFSC, with information provided by the author

Mikuni, Vinicius Massami

Measurement of cosmic ray electrons and positrons
with the AMS-02 experiment / Vinicius Massami
Mikuni; advisor Manuela Vecchi - revised version --
São Carlos 2017.
88 p.

Dissertation (Master's degree - Graduate Program
in Basic Physics) -- Instituto de Física de São
Carlos, Universidade de São Paulo - Brasil , 2017.

1. AMS-02. 2. Electron. 3. Positron. 4. Cosmic
ray flux. 5. Solar modulation. I. Vecchi, Manuela,
advisor. II. Title.

To my family and friends.

In special to the one who I knew longer than all, but is not here anymore.

ACKNOWLEDGEMENTS

First and foremost, thanks to my family for supporting and believing in my dreams. I also would like to express my sincere gratitude to my advisor Prof. Manuela Vecchi for the continuous support of my Masters study and research, for her patience, motivation, enthusiasm, and immense knowledge. My deepest gratitude to my friends whose enthusiasm were key to motivate me to be who I am. My sincere thanks to all my professors, who guided me to where I stand today. Last but not the least, I would like to thank FAPESP (Processes: 2016/10222-9 and 2016/16141-0) for supporting my research.

*“It is not knowledge, but the act of learning,
not possession but the act of getting there,
which grants the greatest enjoyment.”*

Carl Friedrich Gauss

ABSTRACT

MIKUNI, V. M. **Measurement of cosmic ray electrons and positrons with the AMS-02 experiment..** 2017. 88p. Dissertation (Master in Science) - Instituto de Física de São Carlos, Universidade de São Paulo, São Carlos, 2017.

The Alpha Magnetic Spectrometer (AMS-02) is a high-energy particle physics detector operating on the International Space Station (ISS) since May 2011. Since its launch, the AMS-02 provided a large amount of data whose precision was never before achieved, opening a new path for the study of cosmic rays (CRs).

The first published results of AMS-02¹⁻³ show tension with the current understanding of the cosmic ray theory, particularly at higher energies. These tensions are directly linked to many fundamental questions like the dark matter nature, the CR origin and their propagation through the galaxy. This work presents the measurement of the electron flux and the positron flux in primary cosmic rays, based on the data collected between May 2011 and November 2016, an extended data set with respect to the published AMS-02 results.³ The results extend the energy range explored up to 1 TeV for electrons and up to 700 GeV for positrons, being consistent with the published results when using the same data set. A discrepancy between the new measurement and the published flux is observed in the low energy region of the electron flux, while the positron flux is in good agreement. This can be explained by a charge dependent solar modulation effect. This hypothesis was investigated by studying the time evolution of the fluxes, focusing on the energy region below 40 GeV, where an electron and positron flux is computed over 74 time bins of 27 days width, corresponding to the sun's rotation period as seen from the Earth. The time dependent analysis confirms hints of charge dependent solar modulation, that are also observed by other independent analysis that have been carried out in parallel within the collaboration.

Keywords: AMS-02. Electron. Positron. Cosmic ray flux. Solar modulation.

RESUMO

MIKUNI, V. M. **Medição de elétrons e pósitrons em raios cósmicos com o experimento AMS-02.** 2017. 88p. Dissertação (Mestrado em Ciências) - Instituto de Física de São Carlos, Universidade de São Paulo, São Carlos, 2017.

O Alpha Magnetic Spectrometer (AMS-02) é um experimento de física de partículas instalado na Estação Espacial Internacional (ISS) desde Maio de 2011. Desde seu lançamento, AMS-02 coleta uma quantidade de dados com tal precisão que até então nunca foram jamais vistos, abrindo o caminho para o estudo dos Raios Cósmicos (CRs). Os primeiros resultados publicados pelo AMS-02¹⁻³ apresentam tensões com o modelo atual da teoria de CRs, particularmente nas altas energias. Essas tensões são diretamente ligadas a diversas questões fundamentais como a natureza da Matéria Escura (DM), a origem dos CRs e suas propagações pela galáxia. Este trabalho apresenta a medição do fluxo de elétrons e pósitrons em CRs primários, baseando-se nos dados coletados entre Maio de 2011 e Novembro de 2016, período estendido com relação aos resultados publicados pelo AMS-02.³ Os resultados estendem o intervalo de energia explorado para 1 TeV para elétrons e 700 GeV para pósitrons, consistentes com os resultados publicados usando o mesmo período. Discrepância entre a nova medição e o fluxo publicado é observada na região de baixas energias para o fluxo de elétrons, enquanto o fluxo de pósitrons continua em bom acordo. O resultado pode ser explicado por uma dependência na carga causada pela modulação solar. Tal hipótese é investigada estudando-se a evolução temporal dos fluxos, focando-se no intervalo de energia abaixo de 40 GeV, onde um fluxo de elétrons e pósitrons é medido durante 74 intervalos temporais de 27 dias, correspondendo à rotação do sol vista da Terra. A análise dependente do tempo confirma a existência da dependência de carga da modulação solar, também observada por outras análises independentes que foram feitas dentro da colaboração.

Palavras-chave: AMS-02. Elétron. Pósitron. Fluxo de raios cósmicos. Modulação solar.

CONTENTS

1	INTRODUCTION	15
1.1	Cosmic rays sources	16
1.1.1	Propagation of galactic CR	17
1.1.2	Electron and positron propagation	18
1.1.3	Cosmic ray propagation in the heliosphere and the solar cycle	20
1.1.4	Cosmic ray propagation in the magnetosphere	22
1.1.5	Astrophysical interpretation of electron and positron fluxes	24
1.2	The Alpha Magnetic Spectrometer	28
1.2.1	Time Of Flight (TOF)	29
1.2.2	Transition radiation detector (TRD)	30
1.2.2.1	Lepton-hadron separation with TRD	31
1.2.3	AntiCoincidence Counter (ACC)	32
1.2.4	Permanent magnet (PM)	33
1.2.5	Silicon Tracker	34
1.2.6	Ring Imaging Cherenkov Detector (RICH)	36
1.2.7	Electromagnetic Calorimeter (ECAL)	38
1.2.7.1	Lepton-hadron separation with ECAL	41
2	ELECTRON AND POSITRON FLUX MEASUREMENT	43
2.1	Event Selection	43
2.2	Event counting method	45
2.3	Flux normalisation	49
2.4	Trigger Efficiency	49
2.5	Exposure Time	51
2.6	Acceptance	52
2.7	Flux Results	61
3	ELECTRON AND POSITRON FLUXES AS A FUNCTION OF TIME	65
3.1	Time dependent event counting	65
3.2	Time dependent exposure time	67
3.3	Time dependent effective acceptance	68
3.4	Results	73
3.5	Result interpretation	75
4	CONCLUSION	81

BIBLIOGRAPHY 83

1 INTRODUCTION

Cosmic rays (CRs) are high energetic particles normally produced outside of the Solar System, propagating within our Galaxy with velocities compatible with the speed of light and energies higher than those achieved by any particle physics accelerator in the Earth.

The particles flux, namely the number of particles per unit of energy, area, solid angle and time ($\Phi(E)$), measured in $GeV^{-1}m^{-2}sr^{-1}s^{-1}$ for proton cosmic rays is shown in Figure 1 as a function of energy. As a function of the energy, the CRs spectra dependence can be described by a power law $\Phi(E) \propto E^{-\gamma}$ with the spectral index γ ranging between 2.7 and 3.0 depending on the energy range and the species.

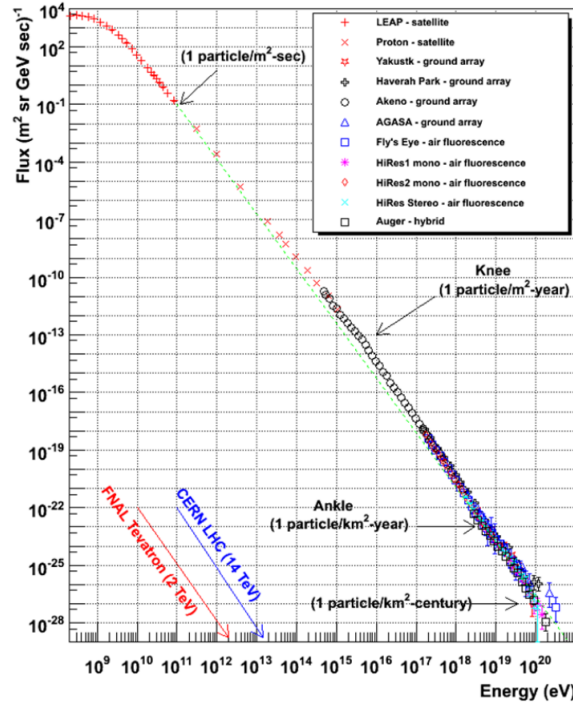


Figure 1 – Overall differential energy spectra of cosmic ray protons from various experiments. Interesting features in the spectrum are indicated like the *knee* at 10^{15} eV and the *ankle* at 10^{18} eV. The frequencies of arrival of particles of different energies are indicated, as well as the center of mass energies attainable in various accelerator experiments.

Source: [LONGAIR⁴](#)

The cosmic radiation is dominated by protons plus light nuclei. Below $\sim 10^6$ GeV, where most of the detected cosmic rays are generated inside the galaxy, the cosmic radiation is roughly composed of 98% by protons and Helium nuclei. The remaining 2% is composed by the other species like electrons, antiparticles and heavier nuclei. Besides the most abundant ordinary matter particles, a small fraction of antimatter particles (10000

times less abundant than protons), like e^+ and p^- , have been observed in the cosmic radiation. For energies below 30 GeV/nucleon the local CR spectra is affected by the Solar Wind, changing the power law behaviour. Magnetic fields at different scales and in different environments affect the acceleration and propagation of CRs. The particle rigidity defined as

$$R = \frac{pc}{Ze} \quad (1.1)$$

measures the resistance of a charged particle with momentum p and charge Ze to deviate in its trajectory because the effect of a magnetic field. For a given magnetic field, the motion of different particles with the same rigidity is the same.

1.1 Cosmic rays sources

The exact sources and acceleration mechanisms of CRs are still open problems. Even though electrons and positrons constitute only a small fraction of cosmic ray particles, their importance in astrophysical studies lies in their unique properties. TeV electrons accelerated at the sources are only able to travel distances in the order of few kpc due to energy losses that electrons undergo while travelling through the galaxy.⁵ Therefore, they can only be signatures of some nearby sources still inside the galaxy. This suggests that the features in the electron and positron spectrum are key to clarify the origins of cosmic rays and as well their propagation mechanisms. Even though the origin of galactic cosmic rays is still debatable, it is widely accepted that the main source comes from Supernova Remnants (SNR).⁶ In the energetic point of view, SNRs are able to explain the energy density of CRs. Assuming the scenario of a supernova (SN) explosion every 50 years in our Galaxy and an average energy budget of $\sim 10^{51}$ erg/explosion, the total power released by these events is about $\sim 5 \times 10^{41}$ erg/s. In order to explain the measured CR power measured in our Galaxy of $w_{CR} \sim 3 \times 10^{40}$ erg/s, only a conversion efficiency for the SN energy to the CR energy in the range of 1% to 10% is necessary, and well compatible with current SN models. The stochastic Fermi mechanisms⁷ of first and second order are able to explain how the shockwave produced by a SNR transfers energy to the particles, i.e. accelerates, CRs up to the energy range of the *knee* region (energies of order 10^{15} eV). This mechanism is appealing since it reproduces, without ad hoc hypothesis, the CR spectrum at the sources before being modified by the propagation in the Universe. Convincing evidences of observed for this process for both electrons and protons are the synchrotron radiation from electrons accelerated at the shockwave fronts in Supernova Remnants (SNR)⁸ and the π_0 lines that are produced by the interactions of accelerated protons with nearby molecular clouds. At higher energies, other mechanisms must be invoked for the acceleration of the CRs like shocks in AGN jets, galactic and extragalactic halos, magnetar, and others, since the Fermi mechanism is limited by the lifetime of the cosmic accelerator. However, this analysis aims to describe the electron and positron

fluxes in the GeV to TeV region, a range of energy in which the galactic sources are more important.

1.1.1 Propagation of galactic CR

After the production and acceleration, primary particles are injected into the Interstellar Medium (ISM) and start to propagate. The propagation is described mainly by the interaction with the medium and with magnetic turbulences. A common model used for the description of the CR propagation in the galaxy is described by a Fokker-Planck type equation⁹ of the type:

$$\frac{\partial \psi(\vec{r}, p, t)}{\partial t} = Q^{tot}(\vec{r}, p, t) + \vec{\nabla} \cdot (D_{xx} \vec{\nabla} \psi_i - \vec{V} \psi_i) + \frac{\partial}{\partial p} p^2 D_{pp} \frac{\partial}{\partial p} \frac{1}{p^2} \psi_i - \frac{\partial}{\partial p} [\dot{p} \psi_i - \frac{p}{3} (\vec{\nabla} \cdot \vec{V}) \psi_i] - \Gamma \psi_i \quad (1.2)$$

where $\psi(\vec{r}, p, t)$ represents the density per momentum units p at space-time coordinates (\vec{r}, t) for the i^{th} CR species. This equation is able to describe several phenomena:

- **Source:** the source term $Q^{tot}(\vec{r}, p, t)$ characterizes any possible production mechanism for primary CR particles. The spatial distribution of the CR sources is assumed to be correlated with the density of known astrophysical sources like pulsars and SNRs. The energy injection spectrum of the sources can be described also as a power law spectrum $\frac{\partial Q}{\partial p} \propto p^{-\Gamma}$.
- **Galactic magnetic field:** while propagating through the Galaxy, CRs are under the influence of interstellar magnetic fields. The bending of the charged particle direction in the magnetic field is determined by the particles rigidity, defined in Equation 1.1. Since this process is only rigidity dependent, different particles with the same rigidity are equally affected by the magnetic fields. The galactic magnetic field can be separated by a regular plus a turbulent component acting as perturbations of the regular field. The scattering of charged CRs plus random small fluctuations $\delta(B) \ll B^{10}$ leads to a diffusive motion. D_{xx} is the diffusion coefficient. $D_{xx} \propto R^\alpha$ addressing the turbulent nature of the perturbations. This mechanism is responsible for making charged CR fluxes isotropic, which means they cannot be traced back at the sources. Besides the spatial diffusion, the interaction of CRs with the turbulent galactic fields induces stochastic accelerations, known as "re-acceleration".¹¹
- **Convection:** this term is caused by the galactic wind that moves from the Galaxy bulk to the Galaxy's halo, affecting the motion of CRs.¹² Galactic winds are composed of a stream of charged particle radially out of the Galaxy's bulk, with velocities that grow linearly with the distance from the galactic plane. The effect of the stream, besides inducing a movement towards the external regions of the Galaxy, also induces adiabatic energy losses as the wind speed increases.

- **Nuclear processes:** Unstable nuclei can decay into other nuclear products, thus decreasing their density and increasing the product densities by a factor proportional to the decay probabilities.
- **Energy losses:** During the propagation in the ISM, CRs interact with the environment, losing energy.. Nuclei mainly lose energy due to ionisation. For lighter CRs, e^+ and e^- , other processes are also relevant like bremsstrahlung, synchrotron radiation, and inverse Compton scattering.

The steady state of Equation 1.2, $\frac{\partial \psi(\vec{r}, p, t)}{\partial t} = 0$, describes the general behaviour of the Local Interstellar Spectrum (LIS) for each species before entering the solar system. The equation can be solved both semi-analytically¹³ or numerically using dedicated packages like GALPROP¹⁴ or DRAGON.¹⁵

1.1.2 Electron and positron propagation

Equation 1.2 can be simplified in case of electrons and positrons, since the nuclear terms can be neglected. The simplified equation is:

$$\frac{\partial \psi_{e^\pm}(\vec{r}, p, t)}{\partial t} = q(\vec{r}, p, t) + D_{xx} \cdot \vec{\nabla}^2 \psi_{e^\pm} - \frac{\partial}{\partial p} \dot{p} \psi_{e^\pm} \quad (1.3)$$

this equation is possible to solve analytically under simplifying assumptions. Considering a steady state, and assuming a high amount of uniformly distributed sources, each injecting CR electrons with a power law spectrum ($N(E) \propto E^{-\gamma} \Rightarrow q(\vec{r}, p, t) = KE^{-\gamma}$) and neglecting diffusion Equation 1.3 is written as:

$$q(\vec{r}, p, t) = \frac{d}{dp} \dot{p} \psi_{e^\pm} \quad (1.4)$$

which assuming $\psi_{e^\pm}(\vec{r}, p, t) \rightarrow 0$ for $p \rightarrow \infty$ yields

$$\psi_{e^\pm}(\vec{r}, p, t) = \frac{Kp^{-(\gamma-1)}}{(\gamma-1) \cdot b(E)} \quad (1.5)$$

where

$$b(E) = -\frac{dE}{dt} \quad (1.6)$$

is the energy loss term suffered by electrons and positrons during propagation, meaning that the spectrum measured at the Earth is not the same spectrum that was created at the sources. To complete understand how the energy losses suffered by electrons and positrons while propagating in the ISM modulate the cosmic ray spectrum, the behaviour of $b(E)$ is necessary. The main processes of energy losses are:

- **ionisation:** The losses caused by ionisation have the form

$$\frac{dE}{dx} \propto \frac{1}{\gamma} \quad (1.7)$$

being γ the Lorentz factor. The energy loss per unit time is then proportional to $\ln E$:

$$-\left(\frac{dE}{dt}\right)_{ionisation} \propto \ln E. \quad (1.8)$$

- **Bremsstrahlung:** Bremsstrahlung is the electromagnetic radiation produced by the deceleration of electrons when deflected by an atomic nucleus. The energy loss rate by Bremsstrahlung is proportional to E :

$$-\left(\frac{dE}{dt}\right)_{bremsstrahlung} = 4nZ^2r_e^2\alpha c\bar{g}E \quad (1.9)$$

where Z is the charge of the nucleus, r_e is the electron radius, α is the fine structure constant and \bar{g} is a Gaunt factor, dependent on the state of the nuclei.

- **Synchrotron radiation:** The dominant channel of energy loss for high energy electrons, is the emission of high energy photons by electrons bending in a magnetic field. The energy loss rate by synchrotron radiation is proportional to E^2 :

$$-\left(\frac{dE}{dt}\right)_{synchrotron} = \frac{4}{3} \frac{c\sigma_T}{(m_e c^2)^2} U_{mag} E^2 \quad (1.10)$$

being c the speed of light, m_e the electron mass, σ_T the Thompson cross-section and $U_{mag} = B^2/2\mu_0$ the energy density of the magnetic field.

- **Inverse Compton scattering:** The process in which electrons scatter low energy photons to high energies. The energy loss rate by inverse Compton scattering in a radiation field of energy density U_{rad} is also proportional to E^2 , given by

$$-\left(\frac{dE}{dt}\right)_{inverseCompton} = \frac{4}{3} \frac{c\sigma_T}{(m_e c^2)^2} U_{rad} E^2 \quad (1.11)$$

Equations 1.10 and 1.11 have the same form and dependence on energy because in both cases, the particle is accelerated by the electric field induced by the relative motion of the particle.

Putting together the previously mentioned mechanisms $b(E)$ is of the form:

$$b(E) = -\frac{dE}{dt} = A.\ln E + B.E + C.E^2. \quad (1.12)$$

For energies $E > 0.1$ GeV the term proportional to E^2 dominates, which means that the main processes of energy losses for this analysis comes from synchrotron radiation and inverse Compton, both taking place in the diffusive halo of the galaxy. Using that $b(E) \propto E^2$, Equation 1.5 yields,

$$\psi_{e\pm}(\vec{r}, p, t) \propto E^{-(\gamma+1)}. \quad (1.13)$$

this means that $\psi_{e\pm}(\vec{r}, p, t)/\Phi(E) \propto E^{-1}$. For this reason, the distance travelled by electrons is small (below few kpc¹⁶). Therefore, the study of the electron flux is a good way to study the nearby universe since their sources should still be inside the Galaxy.

1.1.3 Cosmic ray propagation in the heliosphere and the solar cycle

Solar Wind is the term used to refer to the outflow of \sim keV charged particles from the Sun's atmosphere. This leads to global and temporal variations in the CRs flux intensity and in their energy as a function of position inside the Heliosphere (HS). This process is identified as solar modulation of cosmic rays.¹⁷ The solar activity is anti-correlated with the intensity of CRs, meaning that the fluxes of low energy particles arriving at Earth after traversing the HS decrease during periods of high solar activity and are at a maximum during phases of low solar activity. The reason for that is because the greater the solar activity, the greater the fluctuations in the interplanetary magnetic field which interferes in the propagation of particles with energies less than about 10 GeV/nucleon to the Earth.⁴

The Solar Wind energy density dominates over the Sun's magnetic field energy density. Therefore the Sun's magnetic field lines are stuck with the plasma, carrying them until the Termination Shock region, where the wind becomes subsonic. The combination of the radial ejection of the wind from the solar atmosphere plus the rotational movement of the Sun, tilted with respect to its magnetic dipole, results in a spiral structure of the magnetic field lines.¹⁸

The boundary of the HS is well outside the solar system, at distances greater than 100 astronomical units (AU). The Voyager 1 probe,¹⁹ launched in 1977, took 36 years to exit the HS and enter the interstellar space in 2013. In the 1800s astronomers realised that the appearance of sunspots, dark regions appearing on the surface of the Sun, was cyclic, with a period averaging about 11 years. As new features of the Sun (solar flares, prominences, coronal loops and coronal mass ejections) were discovered, it was found that they also were correlated with the frequency of sunspots. The sunspot number is now commonly accepted as a measure of solar activity. Solar activity itself has been linked to satellite failures, electrical power outages, and variations in Earth's climate.

The 11 year solar activity cycle induces adiabatic time dependent effects. Stochastic perturbations are induced by peaks of solar activity in the time scales going from hours to days. The long term effects can be modeled using the Force Field Approximation model,²⁰ which relates the unmodulated LIS flux (Φ_{LIS}) to the solar modulated flux (Φ_{mod}) as a function of energy E by the following relation:

$$\Phi_{mod} = \frac{E^2 - m^2}{(E + Ze\phi)^2 - m^2} \Phi_{LIS}(E + Ze\phi) \quad (1.14)$$

where m and Ze are the particles mass and charge respectively, while ϕ is the effective solar modulation potential which describes the typical energy losses of CR particles in the HS. Figure 2 shows an example of the the time dependence of cosmic nuclei energy spectra measured by Advanced Composition Explorer (ACE).

The Interplanetary Magnetic Field (IMF) has a defined polarity, defined by the direction of magnetic field in the northern and southern hemispheres of the HS (labeled as

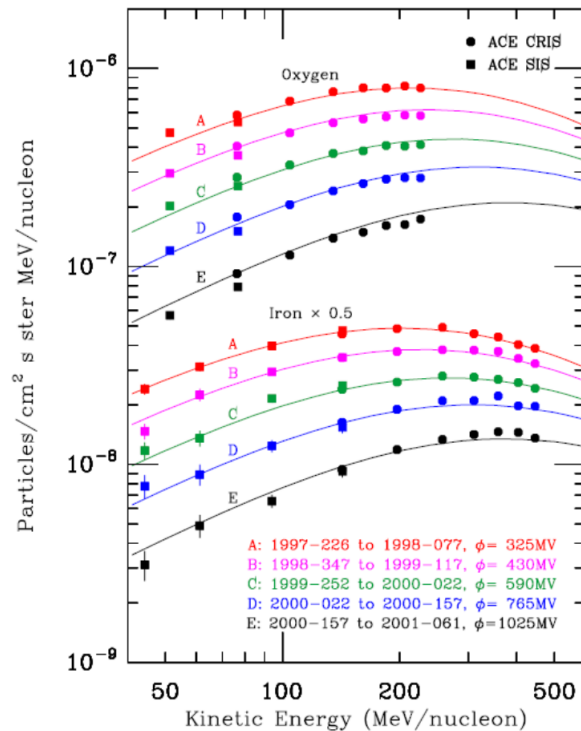


Figure 2 – Oxygen and iron energy spectra measured by ACE during five time periods from August 1997 through February 2001, fitted using a GCR propagation model.

Source: DAVIS et al.²¹

A in the following). During each period of extreme solar activity there is a reversal of the Heliospheric Magnetic Field (HMF), defining another important cycle of 22 years. Figure 3 illustrates observation of the 11 and 22 years cycles.

Additional short-term periodicities are the 25-27 days variation, due to solar rotation and the daily variation due to Earth's rotation (variations of the order $\sim 1\%$).

Superimposed to the average structure of the IMF field, random perturbations are present, due to transient random solar events, as flares and Coronal Mass Ejection (CMEs). CMEs are strong explosions carrying together magnetic field and plasma from the Sun's corona. CMEs originate from twisted magnetic field lines on the Sun's surface, made of plasmas trapped in the field of the corona. When these magnetic field lines erupt from active regions on the Sun (regions associated with sunspots and strong magnetic fields), they are often accompanied by large solar flares. CMEs travel with speeds in the range of 100 km/s to 3000 km/s, with typical speeds of 300 km/s. The fast CMEs can reach Earth in as little as 14-17 hours. When they impact in the Earth's magnetosphere geomagnetic storms and enhanced aurora occurs. The intensity and distribution of the CMEs depend also on the current period of solar activity. A solar flare is a sudden, large, localised increase of brightness near the Sun's surface. Flares are often, accompanied by CMEs.²² The flare ejects clouds of electrons, ions, and atoms through the Sun's corona.

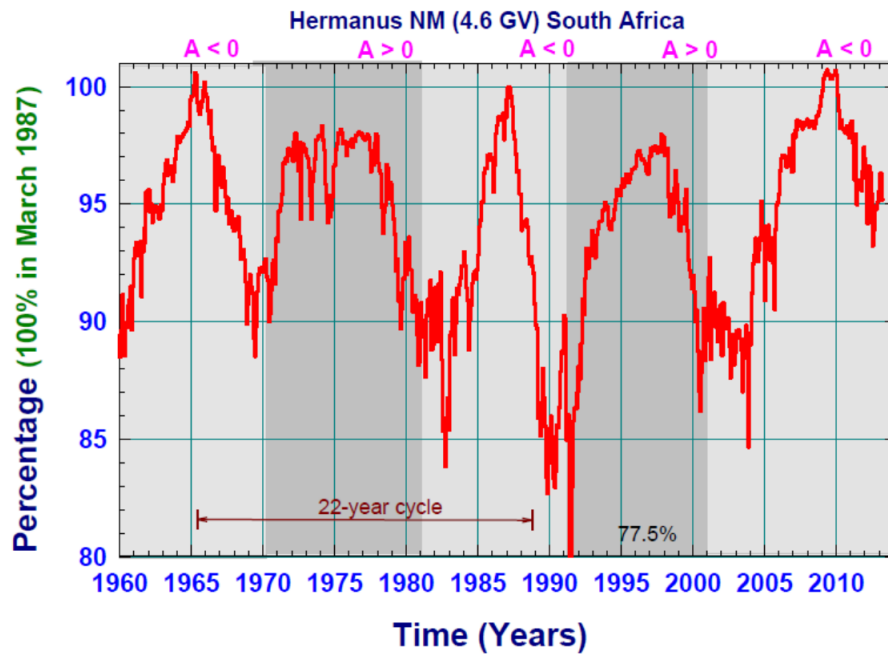


Figure 3 – An illustration of the 11-year and 22-year cycles in the solar modulation of CRs as observed by the Hermanus Neutron Monitor in South Africa corresponding to 100% in terms of percentage in March 1987. positive values of A epochs means the years when HMF is directed in the northern hemisphere, while negative values of A the HMF is directed in the southern hemisphere.

Source: POTGIETER¹⁷

Particles can get accelerated by the magnetic energy released during the flare at relativistic energies creating *Solar Energetic Particles events*. These clouds typically may reach the Earth a few hours after the event. The frequency of occurrence of solar flares changes from several per day during periods of high activity to less than one a week during quiet periods.

The effect of solar modulation can be further refined by the introduction of a charge sign dependent effect. Gradient and curvature drifts due to the geometry of the current polarity of the solar magnetic field affects the motion of opposite sign particles differently.²³ Such effects have to be considered when comparing low energetic the flux of charged particles measured at Earth, i.e after traversing the HS.²⁴ This analysis presents a time dependent flux of electrons and positrons during 5 years of operation of the AMS-02 detector. These results are crucial in the understanding of the time dependence of the solar modulation as well as possible charge sign dependence on CR spectra..

1.1.4 Cosmic ray propagation in the magnetosphere

The last region crossed by CRs before reaching the Earth's atmosphere is the Magnetosphere, the region in which the magnetic field of the Earth dominates the dynamics of CRs. The geomagnetic field, generated by the motion of fluid nickel-iron in the Earth's

outer core, can be modeled by a tilted dipolar field with moment $M = 8.10^{17} Tm^2$, with displacement by ~ 400 km from the centre of the Earth and inclined by $\sim 11^\circ$ with respect to the Earth's axis of rotation.²⁵ Outside the magnetosphere, the dipole field is distorted by the effects of the incoming Solar Wind, as shown in Figure 4. Due to the

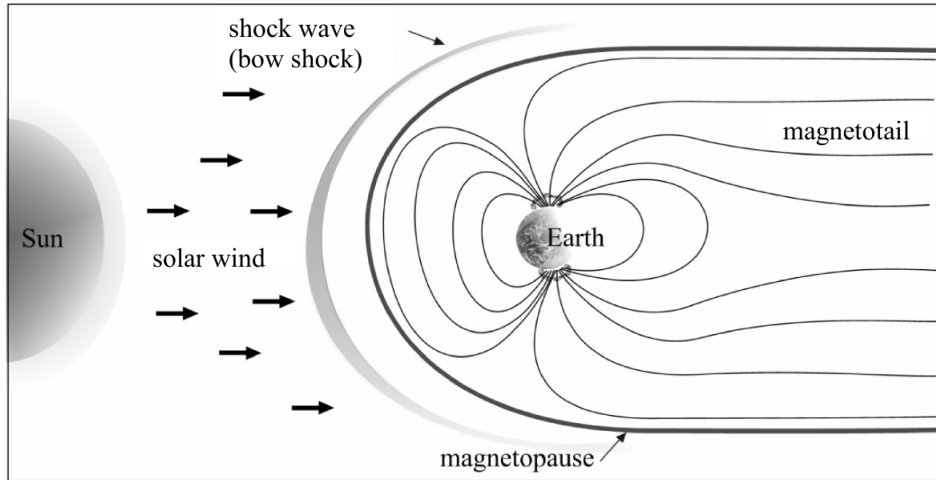


Figure 4 – Schematic diagram showing the structure of the Earth's Magnetosphere. The Solar Wind creates a shock wave and distorts the dipole structure of the geomagnetic field. The Magnetopause is the region that sets the boundary where the Earth's magnetic field dominates over the Solar Wind. It is encountered at $\sim 11 R_H$ from the closest point to the ground, where R_H is the Earth's radius length.

Source: KEYSER et al.²⁶

dipole configuration, the magnetic field on the ground is also distorted as seen in Figure 5. A notable consequence is the appearance of the South Atlantic Anomaly (SAA).

The SAA is the region where the Earth's magnetic field reaches its lowest value.²⁸ In this region, the CR flux is dominated by the low energetic particles trapped by the magnetic field of the Earth. The geomagnetic field also confines the motion of low energetic secondary particles produced by interactions of primary CRs with the local environment. Depending on the particle's rigidity, the intensity of the geomagnetic field and the particle's incoming direction, a galactic CR may not be able to reach the detector. This shielding effect is described by the rigidity cutoff R_c parameter: if the particle's rigidity is below the cutoff, the trajectory cannot be extrapolated to regions outside the Magnetosphere, resulting in a particle that has to be a trapped secondary, as it could not have reached the detector from outside the Magnetosphere. The analytical expression developed by Stormer²⁹ to calculate the value of the cutoff $R_c^\pm(\theta, \phi)$ for a particle in a given geomagnetic altitude and azimuthal angles θ, ϕ in the AMS reference frame is given by equation (1.15),

$$R_c^\pm(\theta, \phi) = \frac{M \cos^4 \lambda}{d^2 [1 + (1 \pm \cos^3 \lambda \cos \phi \cos \theta)]^2} \quad (1.15)$$

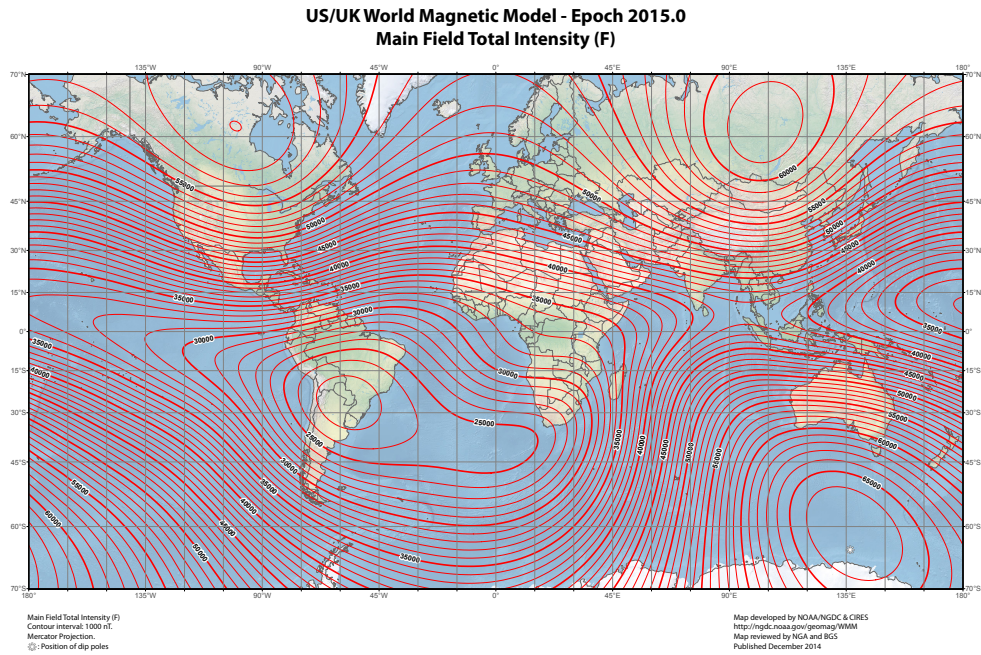


Figure 5 – Total magnetic field isolines at the Earth’s surface, measured in nT. The minimum region (South America) is caused by the Earth’s inner Van Allen radiation belt configuration. It is usually referred to as South Atlantic Anomaly.

Source: [NATIONAL GEOSPATIAL-INTELLIGENCE AGENCY](#)²⁷

where M is the dipole moment, the \pm sign applies to negative/positive charged particles and the arrival location, defined by the geomagnetic coordinates (d, λ) . d is the distance from the dipole centre and λ is the latitude along the dipole.

1.1.5 Astrophysical interpretation of electron and positron fluxes

Over the past decade several measurements of the cosmic ray electrons and positrons suggested intriguing features. The PAMELA satellite first reported³⁰ an "anomalous" raise with energy of the positron fraction, defined as the ratio between the positron flux and the electron plus positron fluxes. This result was later confirmed with high precision and over an extended energy range by the AMS-02 experiment,¹ as shown in Figure 6.

The AMS-02 experiment also provided precise measurement of the electron and positron fluxes in the energy range between 0.5 GeV and 500 GeV (for positrons) and 700 GeV (for electrons). Using the individual fluxes shown in Figure 7 it is possible to point out that electron and positron fluxes are different in magnitude and energy dependence, so that the raise in the positron fraction is actually due to a raise in the positron flux, and not to a loss of electrons.

The raise in the positron fraction is in contrast with the hypothesis that positrons are only secondary particles. Given our current understanding of the cosmic ray propagation

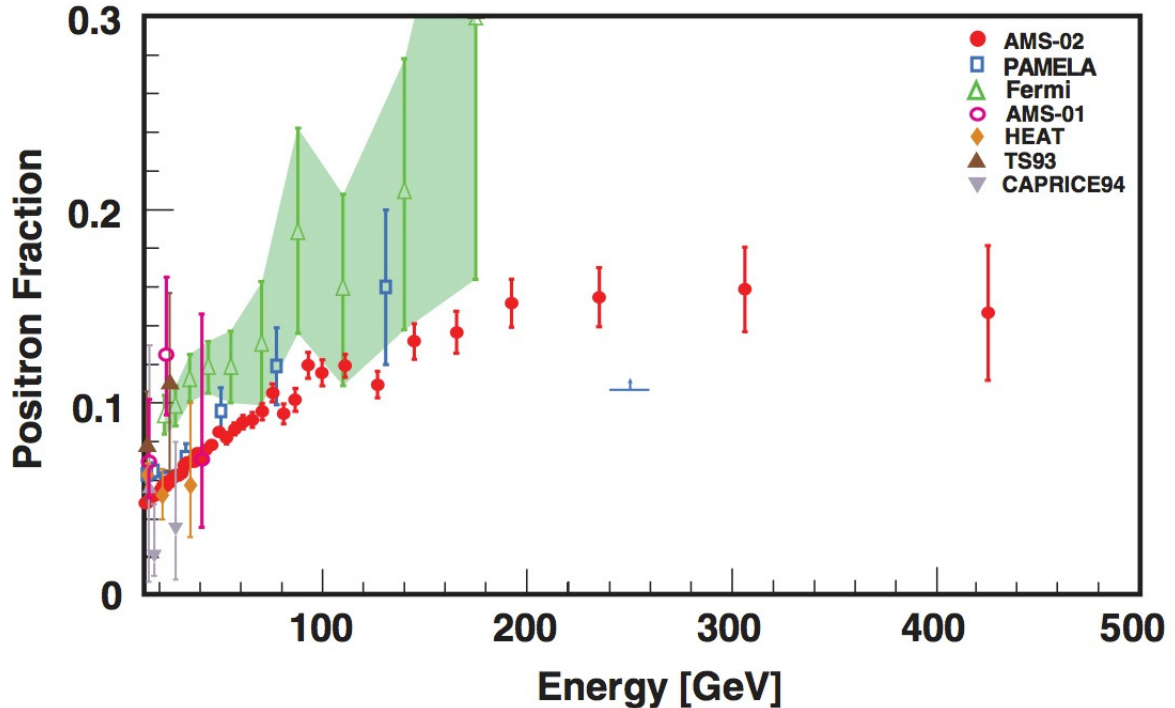


Figure 6 – Positron fraction measured by the AMS-02 collaboration as a function of the energy.

Source: [AGUILAR et al.¹](#)

in the Milky Way, positrons are produced in standard astrophysical processes, namely the propagation of cosmic rays (mainly protons and He nuclei) in the interstellar medium. Figure 8 shows the AMS-02 positron flux compared to the expected secondary flux.³¹

The cosmic ray positron measurements imply the need for a primary component of positrons, namely the existence of a source of positrons in the vicinity of the Solar System. Positron-electron pairs could be produced and accelerated by nearby rapidly rotating neutron stars, i.e. pulsars.³² Besides standard astrophysical mechanisms, exotic scenarios like the annihilation of dark matter (DM) particles in the Milky Way halo could also be probed. Positrons constitute a good channel to search for dark matter, given their low abundance in cosmic radiation^{32–34} On top of the antiparticles from standard astrophysical processes, the messengers of dark matter annihilation would generate distortions in the measured fluxes. It is possible to show that if the positron excess is due to the annihilation of DM in the vicinity of the Solar System, the mass of the DM particle has to be higher than 500 GeV. Moreover, the direct annihilation into lepton pairs seems disfavoured, while direct annihilation into quarks, Z, W, or Higgs boson pairs is reproducing the data, with best-fit masses between 10 and 40 TeV. The interpretation of the data in terms of pulsars is also viable: few pulsars in the vicinity of the Solar system have been identified as possible candidates to satisfy the experimental measurements.

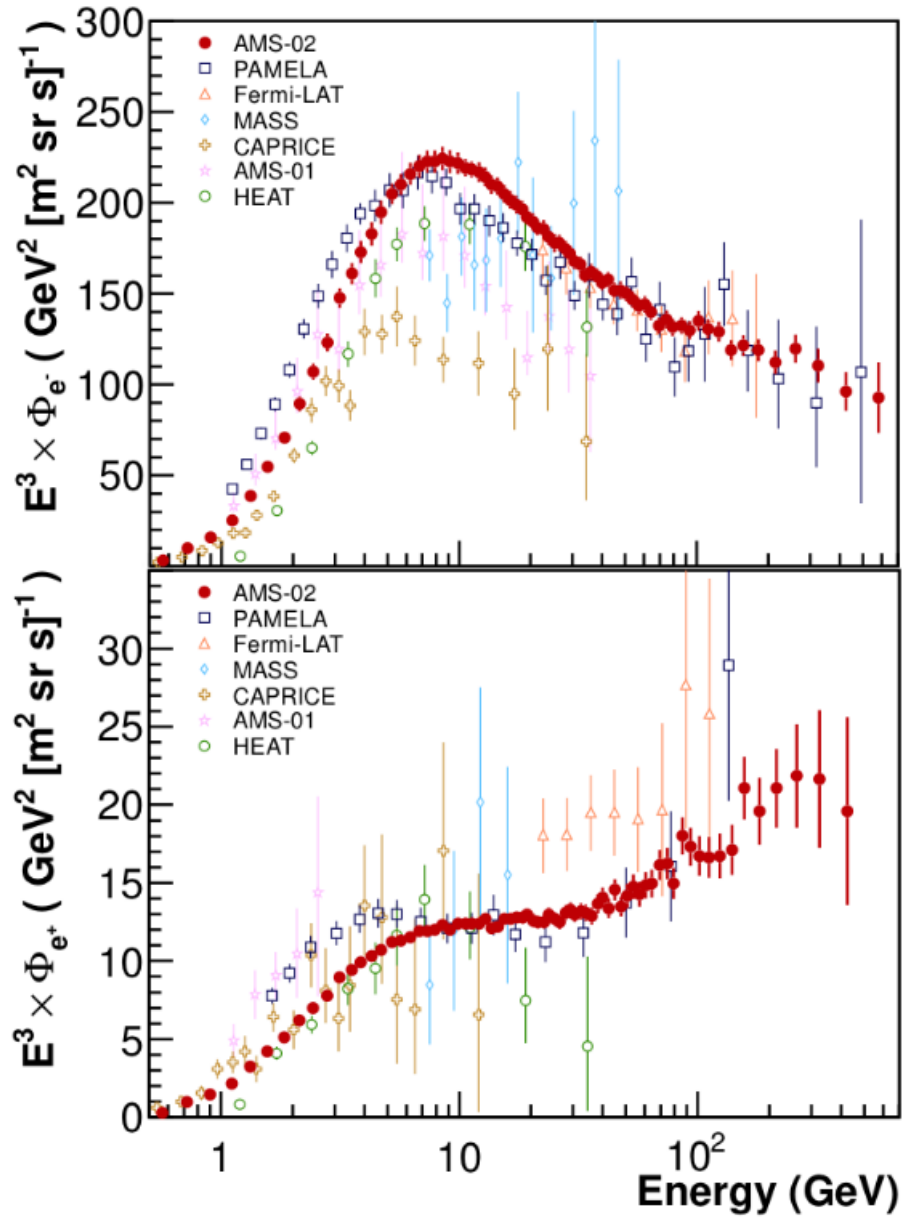


Figure 7 – Cosmic ray electron and positron flux, rescaled by the cube of the energy, as a function of energy. The red dots indicate the AMS-02 data, compared with previous measurements.

Source: [AGUILAR et al.](#)³

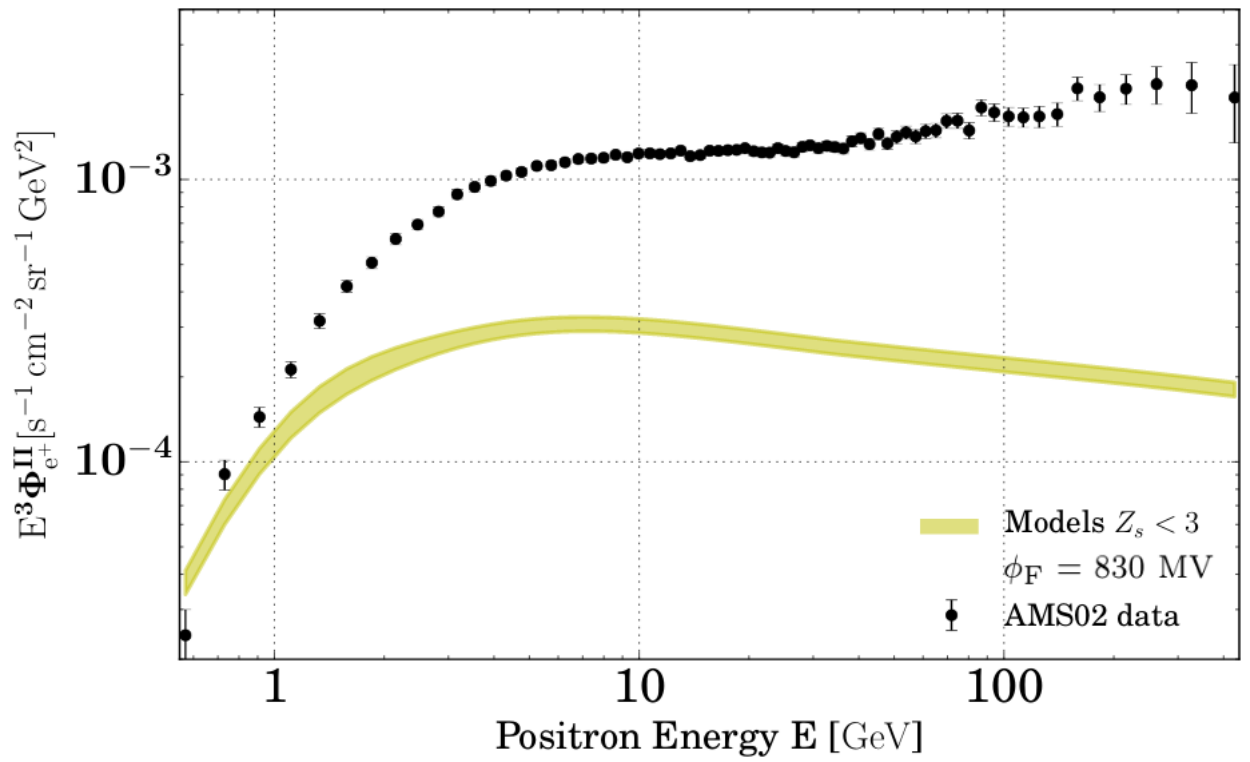


Figure 8 – Positron flux measured by the AMS-02 compared to the expected spectrum from pure secondary hypothesis.

Source: BOUDAUD et al.³¹

1.2 The Alpha Magnetic Spectrometer

The main goal of the Alpha Magnetic Spectrometer (AMS-02) experiment is to carry a precise measurement of the cosmic ray fluxes in the GeV to TeV energy range for different CR species. These measurements are used to better understand the origin and propagation of cosmic rays as well as on the search for dark matter signals and primordial antimatter. Given its large acceptance and long duration of the mission, AMS-02 has also unique capabilities to perform precise long term measurements relevant for solar physics. The AMS-02 has been installed on the International Space Station (ISS) in May 2011 where it will collect CR events until the end of the ISS mission, currently set to 2024. AMS-02 is an improved version of the AMS-01 magnetic spectrometer, which flew on the Shuttle Discovery (STS-91 NASA mission) in June 1998. AMS-02 has been designed and built taking advantage from the experience gathered in particle physics experiments. Its core is composed of a permanent magnet generating a field of about ~ 0.14 T within a cylindrical shaped volume (diameter and height ≈ 1 m). Seven planes of silicon detectors inside this volume and two planes outside the field volume measure the coordinate of the points used to reconstruct the tracks left by charged particles. The magnetic spectrometer is able to measure rigidities from fractions of GV to few TV. Two segmented scintillator planes (TOF) are placed at both ends of the magnet. They measure the time of flight of the particle through the planes and provide part of the trigger of the experiment. An anticoincidence scintillator system (ACC) provides the veto signal in the trigger for particles crossing the detector outside its field of view. The AMS detector particle identification capabilities are completed by three sub-detectors: the Ring Imaging Cherenkov (RICH) detector, below the magnet, for the measurement of the particle velocity and charge; the Transition Radiation Detector (TRD), placed on top, to identify e^\pm and the Electromagnetic Calorimeter (ECAL), at the bottom, for the accurate discrimination between leptons and hadrons and energy measurement. Figure 9 shows a depiction of the detector and its subdetectors.

A relevant goal for AMS concerns the indirect Dark Matter detection. Its large acceptance, long exposure time and precise particle identification capabilities allow to measure the spectra of the cosmic radiation rare components (p^- , D, e^\pm , γ) with great accuracy over an energy range that was never explored before. The large amount of data collected by the experiment for all the charged CR species, including chemical species up to iron and isotopes up to carbon, will improve the understanding of the galactic space environment and help to solve several fundamental questions concerning CR acceleration and propagation. The measurements of low energy CR fluxes during an entire 11 years solar cycle will also help in the understanding of solar physics and in the propagation of CRs in the HS environment. The requirements for a space-borne high energy physics experiment are challenging. Several constraints while designing the detector are imposed

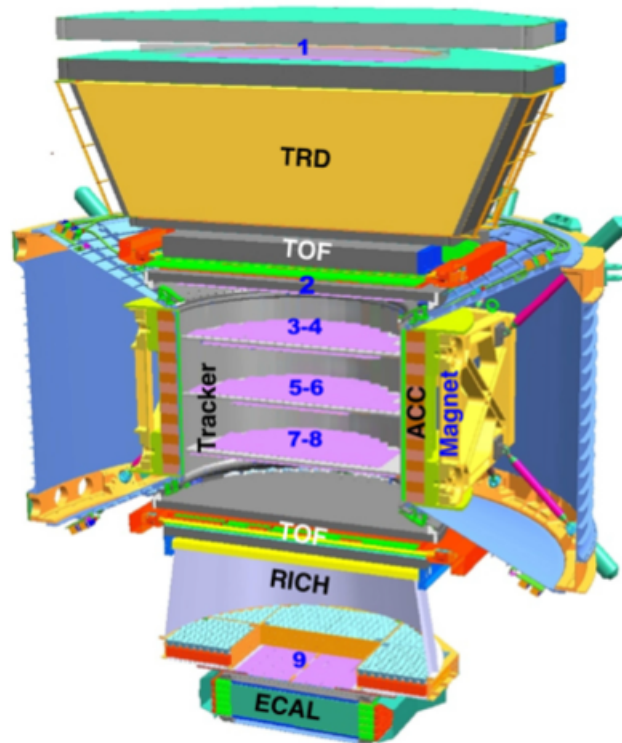


Figure 9 – AMS-02 detector and its subdetectors.

Source: [TING³⁵](#)

by the transport to the Space Shuttle and by the permanence on the ISS, as the strict weight limit of 7 t, the low power consumption requirement (≤ 2 kW) and the limited data rate transfer to ground. In addition, the AMS-02 experiment must work properly in space without any external operation for the whole mission while withstanding vibrations up to 150 dB during shuttle launch and temperature variations between -30° C and $+50^{\circ}$ C in space vacuum. Each sub-detector and electronic component is produced in prototypes tested in order to provide the expected physics performances and to meet the mandatory space safety requirements.

1.2.1 Time Of Flight (TOF)

The AMS Time Of Flight (TOF) system^{36,37} is composed by a total of four layers of scintillator counters, placed in pairs above (Upper-TOF) and below (Lower-TOF) the magnet. The TOF measures the particle's velocity (βc), direction of flight and charge. It also used to provide the main trigger to the whole experiment. The 4 TOF layers are composed (from top to bottom) of 8, 8, 10, 8 paddles. The counters are made of 1 cm thick polyvinyl-toluene scintillators in two different shapes: rectangular for the inner counters (width ~ 12 cm) and trapezoidal for the external counters (width 18 to 26 cm), all having a length between 117 and 134 cm. In each pair of layers, paddles are oriented respectively

in both x and y directions, to provide a two-dimensional measurement with a $12 \times 12 \text{ cm}^2$ resolution (see Figure 10). The scintillation light is collected from both sides of each counter using 2 or 3 photomultiplier tubes (PMT). The anode signal is read out from

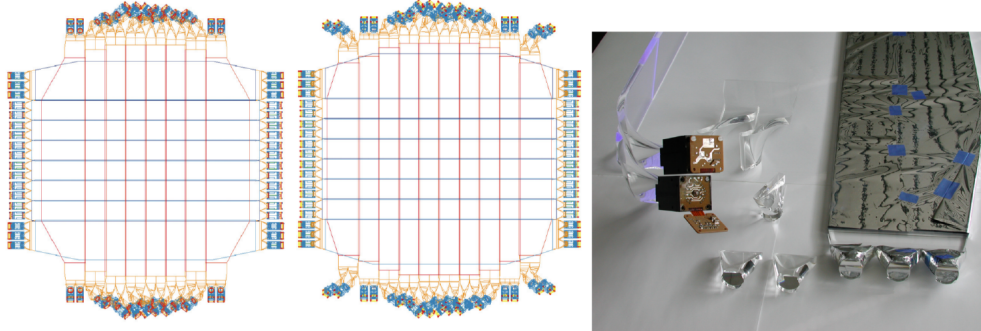


Figure 10 – **Left:** AMS TOF planes configuration for Upper-TOF (left) and Lower-TOF (right). For each pair, paddles are arranged along opposite direction to ensure 2-dimensional measurements. **Right:** TOF scintillating counter, light guides and PMTs.

Source: BINDI et al.³⁸

PMTs and compared to the three different thresholds: Low Threshold (LT, $\sim 20\%$ of a proton Minimum ionising Particle (MIP) signal), High Threshold (HT, $\sim 50\%$ of a proton MIP signal) and Super-High Threshold (SHT, $\sim 400\%$ of a proton MIP signal). HT and SHT signals are used by the Level-1 trigger logic (see Section 2.4) to trigger $Z \geq 1$ particles ("Single charge" trigger) and $Z > 1$ particles ("Normal-Slow ions" trigger). The LT TDC (Time to Digital Conversion) signal is used for timing measurement. The particle velocity $\beta = \Delta s/c\Delta t$ is measured using the time of flight Δt between Upper-ToF and Lower-ToF and the trajectory length Δs . The timing resolution of TOF is $\sim 48 \text{ ps}$ for C nuclei. The resulting TOF velocity resolution $\Delta\beta/\beta$ has been measured using data collected in space to be $\sim 4\%$ for $Z = 1$ particles and decreasing up to $\sim 1\%$ for $Z \geq 4$ (See Figure 11). The precise velocity measurement allows to distinguish downward-going particles from upward-going particles at a level better than 10^{-9} . The anode Analog-to-Digital Converter (ADC) signal is used to measure the particle's energy deposit and consequently to infer the particle charge Z since $(dE/dx \propto Z^2)$.

1.2.2 Transition radiation detector (TRD)

Transition radiation is electromagnetic radiation emitted when a charged particle passes through inhomogeneous media, such as a boundary between two media with different dielectric constants. Particles with a high Lorentz factor, normally light particles such as electrons, induce radiation in the X-rays range.^{40–42} The TRD of AMS is located on top of the detector, between the Layer 1 of the tracker and the planes of the TOF. It is designed for the purpose of identifying particles through the detection of emitted radiation. It is consisted of 20 layers with 8 in X direction and 12 in the Y direction. Each TRD layer is

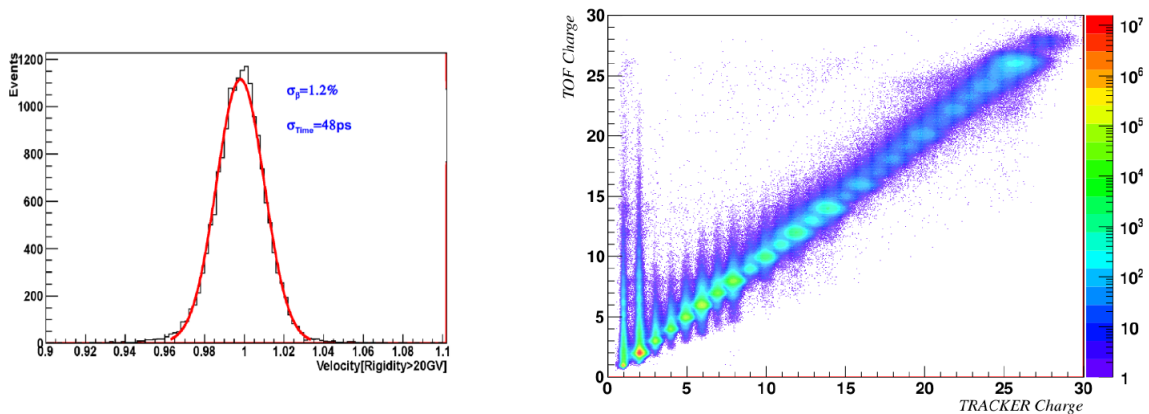


Figure 11 – **Left:** AMS TOF velocity measurement resolution for carbon ($Z = 6$). **Right:** Distribution of TOF and Silicon Tracker charge estimators measured using cosmic particles up to Zn ($Z = 30$). The z scale represents the numbers of collected events. The redundancy of the AMS detector provides measurements of the charge by two independent sub-detectors, reducing systematic uncertainties in the charge separation capabilities.

Source: **Left:** BINDI et al.,³⁸ **Right:** BINDI et al.³⁹

composed of 22 mm of fibre fleece to induce the transition radiation and 16 straw tubes filled with Xe and CO_2 gas mixture to produce ionisation avalanche and converts the X-rays into electric signals. While positrons and electrons produce extra X-rays, protons and heavy nuclei do not. This difference provides means for lepton and proton separation. Leptons hereinafter indicating electrons and positrons.

1.2.2.1 Lepton-hadron separation with TRD

The different behaviour of leptons and protons in the TRD was studied with test beams and Monte Carlo (MC) simulations, where protons and electrons show different measurement features. By the parameterization of those features, a TRD likelihood ratio (TRD_{lhr}) is developed based on the signal amplitude detected in each layer of TRD, E_{TUBE} . The likelihood functions are normalised probability functions, defined as:

$$\begin{aligned}
 \text{Protons : } P_p &= \sqrt[n]{\prod_i^n P_p^{(i)}(E_{TUBE})} \\
 \text{Electrons : } P_e &= \sqrt[n]{\prod_i^n P_e^{(i)}(E_{TUBE})}
 \end{aligned}
 \tag{1.16}$$

where n is the number of TRD layers used in the measurement. Thus, the TRD likelihood ratio estimator is given by

$$TRD_{lhr} = -\ln\left(\frac{P_e}{P_e + P_p}\right)
 \tag{1.17}$$

The dependence of the proton rejection power with rigidity is shown in Figure 12.

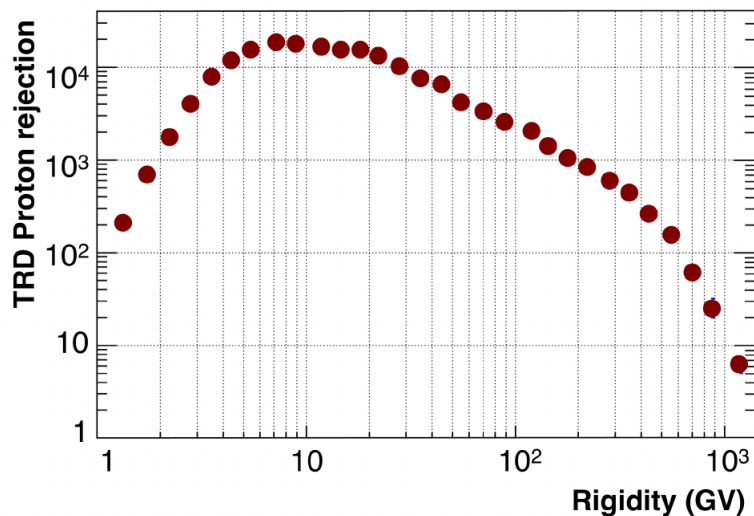


Figure 12 – Proton rejection measured with data collected by AMS, while keeping 90% efficiency on the signal. The rejection factor is defined as $\epsilon_{electron}/\epsilon_{proton}$, where $\epsilon_{electron}$ and ϵ_{proton} are respectively efficiency of TRD_{lhr} cut for electrons and protons.

Source: AGUILAR et al.¹

The rejection factor is defined as $\epsilon_{electron}/\epsilon_{proton}$, where $\epsilon_{electron}$ and ϵ_{proton} are respectively efficiency of TRD_{lhr} cut for electrons and protons. At higher rigidities protons also start to induce X-rays, which results in the decrease of efficiency. An example of the TRD separation power is given in Figure 13.

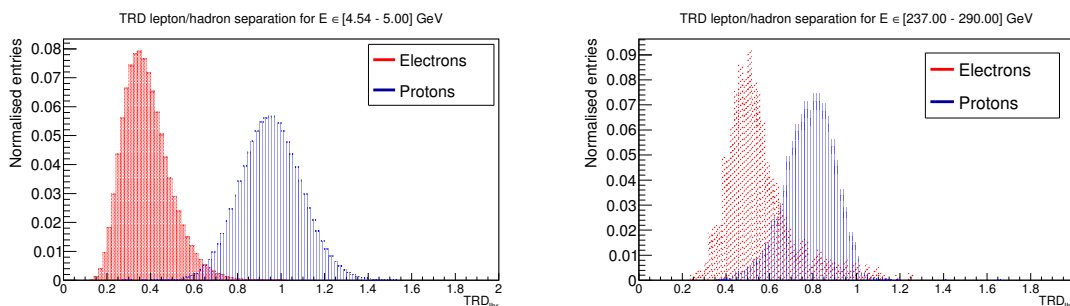


Figure 13 – TRD_{lhr} distribution example for electron-like events and proton-like events for the energy interval [4.54 - 5.00] GeV (left) and [237.00 - 290.00] GeV (right). The separation gets worse as the energy increases

Source: By the author

1.2.3 AntiCoincidence Counter (ACC)

The Anti-Coincidence Counter (ACC)^{43,44} is composed of 16 paddles with dimensions $220 \times 830 \times 8 \text{ mm}^3$ arranged on a cylinder that surrounds the inner Tracker. The light coming from scintillation panels is collected in wavelength shifter fibres of 1 mm diameter and then routed through clear fibres up to the 16 PMTs (8 on the top and 8 on the bottom side) similar to the TOF. The high efficiency and degree of homogeneity of the

scintillating fibres ensure a reliable and fast ACC veto trigger signal for high inclination particles that cross the detector outside the field of view. The veto efficiency is measured to be 100% at the level of 10^{-5} , in agreement with the design specifications.

1.2.4 Permanent magnet (PM)

At the centre of the AMS detector lies the permanent magnet. Although AMS-02 was initially designed to use a superconducting magnet, the extension of the ISS mission duration up to 2024 made it necessary to replace the superconducting magnet with the AMS-01 prototype permanent magnet. The magnet is composed of 6400 $5 \times 5 \times 2.5 \text{ cm}^3$ Nd-Fe-B blocks. The blocks are distributed in 100 circle shaped layers, each formed by 64 blocks, and assembled in a toroidal structure of 1 m height with inner and external radius $r_i = 111.5 \text{ cm}$ and $r_e = 129.9 \text{ cm}$ respectively. This configuration results in $B = 0.149 \text{ T}$ dipole field within the magnetic walls. The external field has been designed to be less than 10^{-2} T in order to minimise the interferences with electronic boards and detectors next to the magnet, also avoiding the mechanical torques on the ISS.⁴⁵ The resulting dipolar magnetic field is sketched in Figure 14. The AMS coordinate reference frame is also centered in the centre of the magnet. The cylindrical symmetry of the magnetic lines defines the z axis, passing through the center of the magnet and pointing towards the top of the detector. The x axis points along the magnetic lines. The y axis completes the right-handed Cartesian coordinate system. Using this definition, the curved motion of particles passing through the magnet is confined to the x-y plane, also called the bending plane.

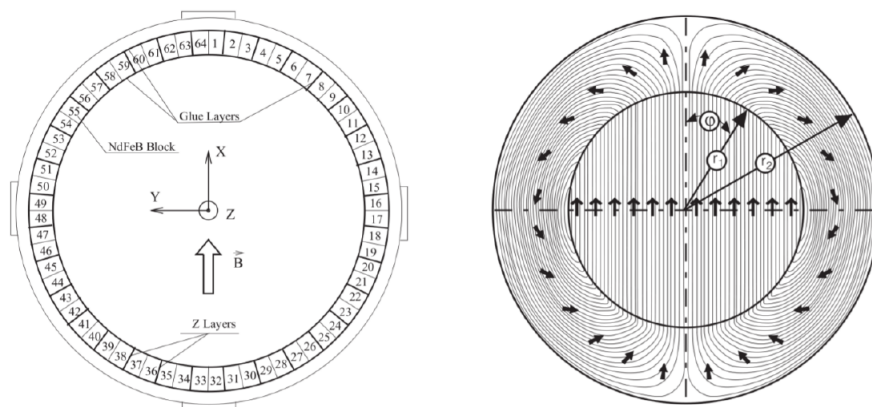


Figure 14 – **Left:** AMS magnet configuration. 64 Nd-Fe-B blocks are distributed in the toroidal structure to provide an uniform dipole field in the magnet inner volume. Superimposed in the picture is the AMS coordinate reference frame. **Right:** Magnetisation vector. Its flux is confined in the magnet volume, providing a negligible leaking field.

1.2.5 Silicon Tracker

The Silicon Tracker system⁴⁷ is used in the AMS-02 experiment to make a measurement of the trajectories of charged particles sampling their crossing positions at various z coordinates. The main elements of the tracking system are the $2264 \times 72 \times 41 \times 0.3 \text{ mm}^3$ silicon micro-strips sensors. On each face of the sensor, metallic strip implants run in perpendicular directions, providing a two-dimensional measurement for each sampling. On the junction side (or p-side), p^+ strips are placed with a (readout) implantation pitch of (110) $25.5 \mu\text{m}$. On the opposite side, the k-side, n^+ strips are placed with a (readout) implantation pitch of (208) $104 \mu\text{m}$, which is oriented in the perpendicular direction. The p-side is used to measure the crossing y coordinate, the k-side is used to measure the crossing x coordinate. The capacitive coupling between the strips and the analog readout achieve a single point resolution of 10 (30) μm on the y (x) side for $Z = 1$ particles. The readout component of the Silicon Tracker is called "ladder". Each ladder consists of 7 to 15 wire-bonded silicon sensors. The energy deposit is read out for each ladder by 1024 readout channels: 640 on the p-side, 384 on the k-side. The readout electronics is placed directly on the front end board at the end of the ladder. The number of ladders composing the tracking system is 192, for a total of $\sim 200,000$ readout channels and a total active area of 6.4 m^2 . The ladders are arranged among 9 layers (see Figure 15). The top layer

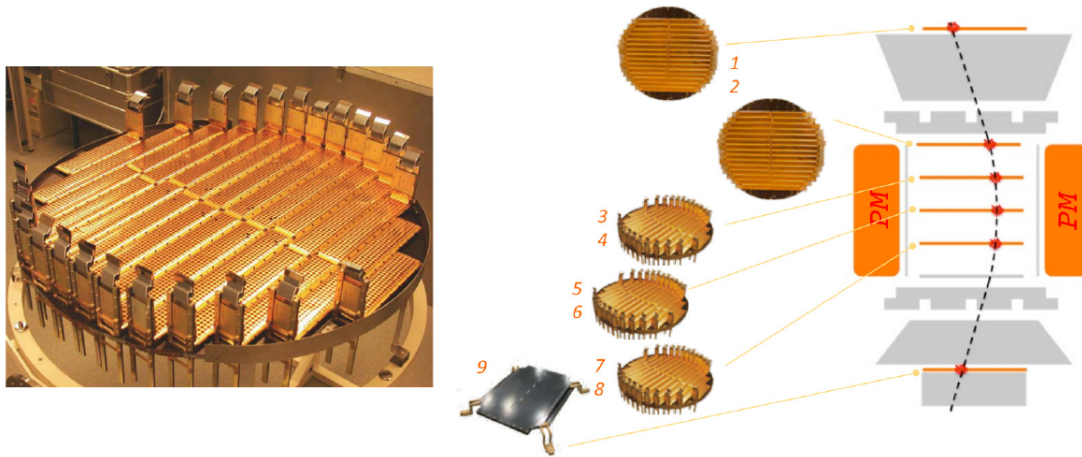


Figure 15 – **Left:** One inner layer of the Silicon Tracker. Each layer is composed of several readout units (ladder). On the end of each ladder, the front-end electronics is installed in vertical. **Right:** Positions of the Silicon Tracker planes. L1 and L9 compose the so-called "external Tracker", while L2 to L8 constitute the "inner Tracker".

Source: ZUCCON⁴⁷

(L1) is located on top of the TRD. The bottom layer (L9) is located between the RICH and the ECAL. The other 7 layers (L2 to L8) form the "inner Tracker": L2 is located below the TOF, just above the magnet, while L3 to L8 are inside the region covered by the magnet volume. Due to the high number of readout channels, the Tracker front end

electronics produces ~ 200 W of heat. In order to ensure optimal performance of the detector and keeping the temperature lower than the maximum limit of 30° C, the heat has to be radiated to outer space. The Tracker Thermal Cooling System (TTCS)⁴⁸ is a CO₂ two-phase-loop thermal cooling system which is used to keep the Tracker electronic and Tracker layer temperatures stable within 1° C. The electronics is also thermally connected to thermal bars to keep the temperature stable. Liquid CO₂ close to the boiling point is pumped through the bars, whose heat is absorbed by the CO₂ before and during the boiling phase. The boiling CO₂ exiting from the bars is in thermal contact with the incoming CO₂ to bring it as closest as possible to the boiling point. This procedure makes the two-phase-loop more efficient than a single-phase loop. The outgoing boiling fluid radiates the heat to outer space through dedicated radiators. The whole TTCS system is completely double redundant to be operated safely in space. The ionisation losses in the sensors ($dE/dX \propto Z^2$) is used to estimate the charge Z of crossing particles, by the collection of the electron-hole pairs which migrates to opposite sides of the sensor. The dynamic range of the electronics allows a measurement of charges up to iron ($Z = 26$) and above (see Figure 16) while the charge misidentification probability is estimated to be 10^{-4} for nuclei up to Oxygen ($Z = 8$).⁴⁹ In order to maximise the Tracker resolution,

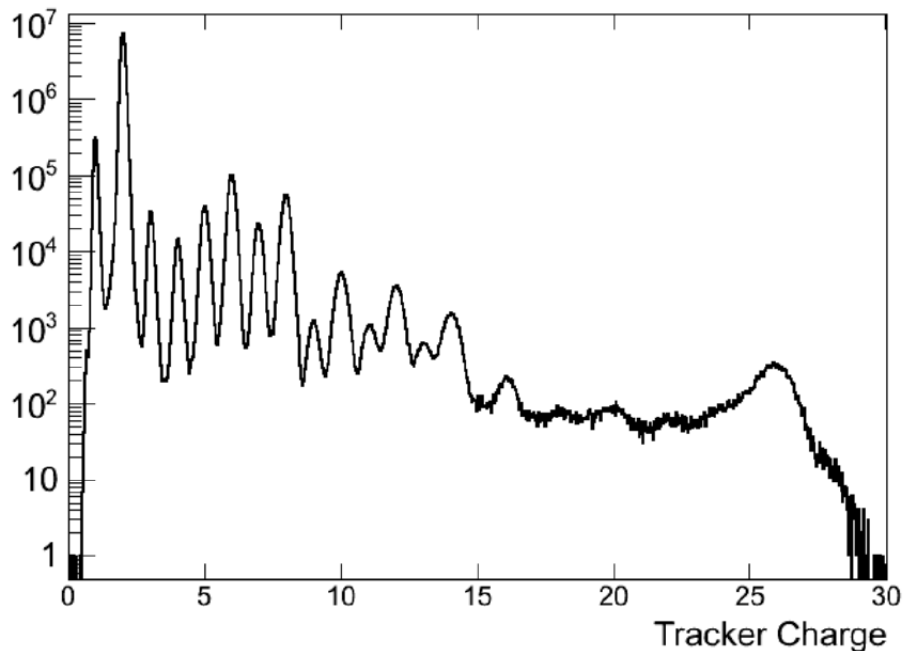


Figure 16 – Charge distribution for cosmic nuclei measured by the Tracker for ISS data. The misidentification probability from neighboring species is 10^{-6} for carbon ($Z = 6$) and 10^{-8} for oxygen ($Z = 8$). Nuclei can be distinguished up to iron ($Z = 26$), whose peak in the picture is well evident due to its natural abundance.

Source: [AMBROSI et al.](#)⁴⁹

it is necessary to know with precision the position of each sensor to few μm . Since the

mechanical positioning measurement has an uncertainty of $\sim 100 \mu m$ (even higher than the single sensor intrinsic resolution), it is necessary to estimate alignment parameters to be applied during the offline track reconstruction algorithm. First, a static alignment of all the 2284 sensors is performed using cosmic protons to correct for the sensor shifts. A dynamical alignment procedure is also applied to the external layers since their supporting structures suffer deformations and shifts due to the large temperature gradient which they are exposed to (up to $\pm 80^\circ C$). Using cosmic protons to provide a time-dependent correction, the outer plane alignment is known with a precision $\sim 3 \mu m$.⁵⁰ In parallel to the alignment procedure, the 7 inner planes movements are monitored by the Tracker Alignment System (TAS),⁵¹ which consists of 5 laser beams produced by diodes installed on the L2 support structures. The incoming particle rigidity is inferred by the measurement of the track curvature in the magnetic field. A fit to the measured crossing coordinates is applied to extract the trajectory parameters. The accuracy of the curvature measurement depends, on the distance between the uppermost and the bottom-most crossing coordinate measurement. This distance is called "span". The rigidity resolution of the Tracker depends on the Tracker span (see Figure 17). In particular the Maximum Detectable Rigidity (MDR), at which the relative error on the curvature amounts to 100%, is ~ 2 TeV for protons and ~ 3.2 TeV for Helium nuclei in the full span configuration.⁵²

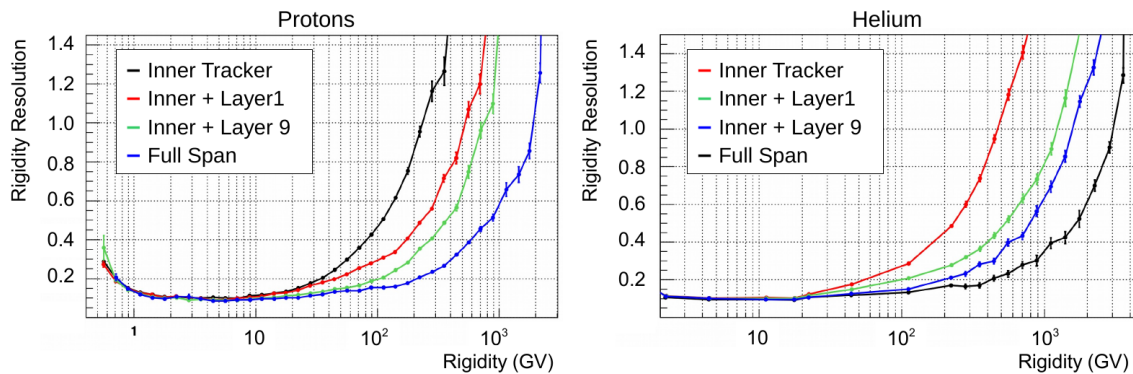


Figure 17 – Rigidity measurement resolution for protons (Left) and Helium (Right) estimated from MC. Different colors identify different Tracker spans. The presence of the external layers used to increase the trajectory lever of arm allows to measure the rigidity of particles crossing the Tracker layers up to the TeV range.

Source: [ZUCCON⁴⁷](#)

1.2.6 Ring Imaging Cherenkov Detector (RICH)

The AMS-02 Ring Imaging Cherenkov detector (RICH)^{53,54} is placed below the lower TOF plane and provides a precise measurements of the β parameter. The detection principle of the detector is based on the Cherenkov electromagnetic emission, produced by a charged particle whose velocity is larger than the phase velocity of the electromagnetic

field in the material. A cone of emission is created along the particle trajectory. The opening angle of this cone is related to the particle's velocity as

$$\beta = \frac{1}{n \cos \theta} \quad (1.18)$$

where n is the refraction index. Moreover, for a particle of charge Ze , the number of radiated photons per radiation length and distance is given by

$$\frac{d^2 N}{d\lambda dx} = \frac{2\pi}{\lambda^2} \alpha Z^2 \sin^2 \theta \quad (1.19)$$

where α is the fine-structure constant. The RICH therefore is also able to provide independent measurement of the particle's charge. The RICH detector consists of a radiator plane, a conical mirror and a photon detection plane. The radiator is composed by a dodecahedral polygon with a 118.5 cm internal tangent diameter. It consists of an array of 2.7 cm thick aerogel tiles with a refractive index between 1.03–1.05, surrounding a central $35 \times 35 \text{ cm}^2$ region equipped with 5 mm thick sodium fluoride (NaF) radiator ($n_{NaF} = 1.335$). A scheme of the detector is shown in Figure 18. The combination of the radiators optimises the

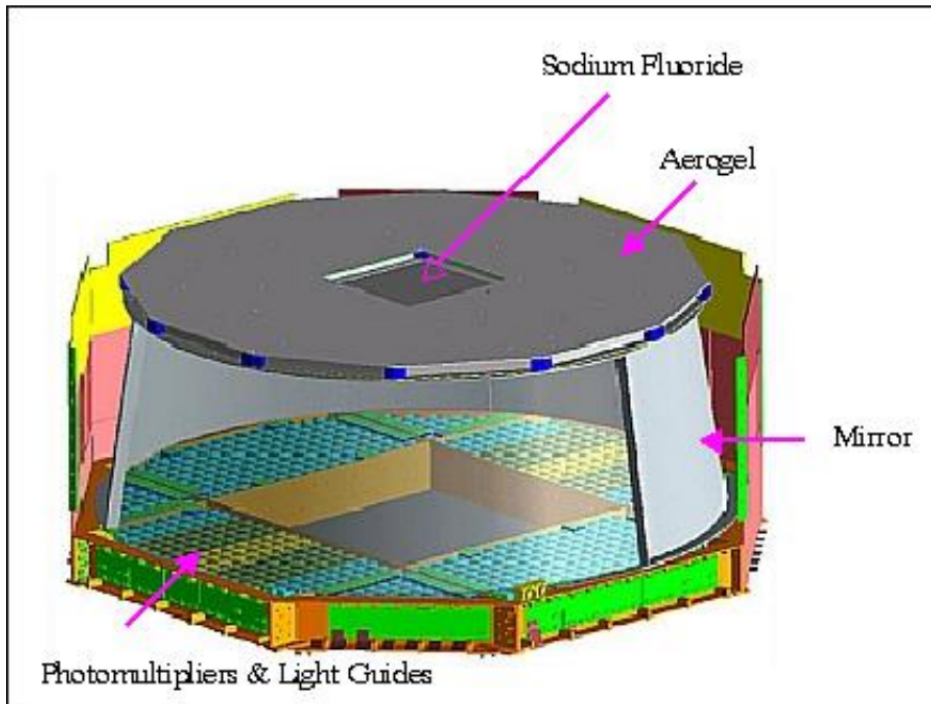


Figure 18 – RICH schematic view.

Source: GRENOBLE⁵⁵

overall counter acceptance ($0.4 \text{ m}^2 \text{ sr}$) since the Cherenkov photons radiated by the NaF in large cones will fall within the detection area. The detector plane has an empty $64 \times 64 \text{ cm}^2$ area in its centre, matching the active area of the electromagnetic calorimeter located

below. Outside the "ECAL hole", 680 4×4-multi-anode PMTs are arranged to cover the circular 134 cm diameter surface at the basis of the conical mirror. The radiator and the detection plane are enclosed in the volume of a conical reflector multi-layer structure on a Carbon fibre reinforced composite substrate. The mirror increases the RICH's acceptance reflecting high inclination photons and provides the necessary photon drift ring expansion. The measurement provided by RICH has a resolution $\sigma\beta/\beta \sim 0.1\%$ for unitary charge particles, and $\sigma\beta/\beta \sim 0.01\%$ for ions. It also provides particle's charge measurement through photon counting for nuclei charges up to iron ($Z = 26$), with a charge resolution below 0.5 charge units for light nuclei (see Figure 19).

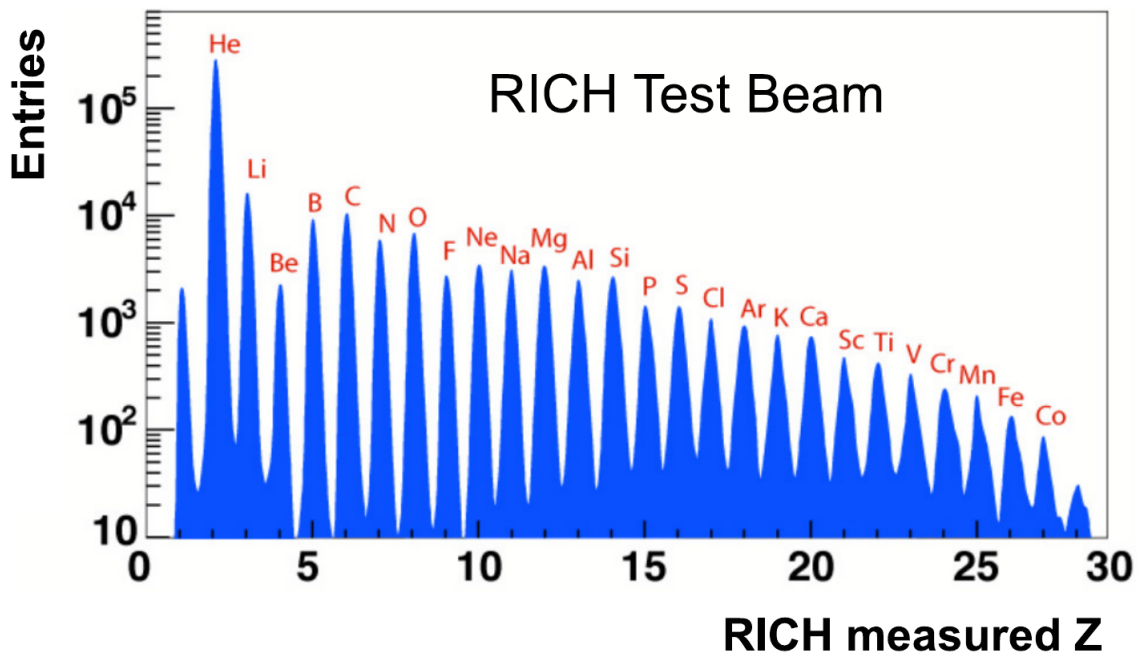


Figure 19 – Measurement of nuclei charges from a RICH test beam. The RICH provides the charge measurement up to iron ($Z = 26$), with a resolution better than 0.5 charge units for light nuclei.

Source: GIOVACCHINI⁵⁶

1.2.7 Electromagnetic Calorimeter (ECAL)

The AMS ECAL is a lead-scintillating fibre sampling calorimeter.⁵⁷ Particles crossing the active volume of the ECAL release their energy and produce light collected by photomultipliers (PMTs) at the fibre's end. The structure^{58,59} is developed to maximise the X_0/λ ratio (X_0 is the electromagnetic interaction length and λ the nuclear interaction length). It consists in a lead-fibre-glue volume ratio of 1:0.57:0.15, an average density of $\sim 6.8 \text{ g/cm}^3$ and a radiation length X_0 of about 1 cm. The ECAL length corresponds to $\sim 17X_0$ and to only $\lambda \sim 0.6$. The active volume is built up by a pile of 9 superlayers (SL) consisting of 11 grooved 1 mm lead foils interleaved by 1 mm plastic scintillating fibres.

The fibres are glued using optical cement running, in each superlayer, in one direction only. Each SL is designed as a square parallelepiped with 68.5 cm side and 1.85 cm height, for a total active dimension of $68.5 \times 68.5 \times 16.7 \text{ cm}^3$, corresponding to $\sim 17X_0$ for perpendicular incident particles (Figure 20). Each SL is read out on one end only by 36 PMTs, alternately arranged on the two opposite sides to avoid mechanical interference. The PMTs are shielded from magnetic fields by a 1 mm thick soft iron square parallelepiped tube, which also acts as mechanical support for the light collection system. Each PMT



Figure 20 – ECAL active volume (pancake). 9 superlayers are piled-up for a total of 50,000 1 mm scintillating fibres running in opposite directions. The total $68.5 \times 68.5 \times 16.7 \text{ cm}^3$ pancake volume consists of a lead-fibre-glue volume ratio of 1:0.57:0.15, for an average density of $\sim 6.8 \text{ g/cm}^3$.

Source: VAGELLI⁶⁰

accommodates four $8.9 \times 8.9 \text{ mm}^2$ anodes. The anodes define the ECAL granularity, for a total of $18 \times 72 = 1296$ readout cells. The 3D imaging of the electromagnetic shower development is achieved by alternating 5 SLs with fibres along the x axis and 4 SLs with fibres along the y axis. The ECAL Molière radius, measured to be *sim* 2 cm, corresponds approximately to 1 PMT width. In order to obtain the necessary sensitivity on minimum ionising particles ($\sim 7 \text{ MeV/cell}$) and to measure energies up to 1 TeV ($\sim 60 \text{ GeV/cell}$) using standard 12-bit ADCs, the digitisation is performed by the front-end readout system at two different gains, with a gain ratio of about 33. Besides the eight signal from anodes, each PMT's last dynode signal is also read out and its information used to have a redundant signal in case of anode breakdowns and also to build up the ECAL standalone trigger. Each ECAL PMT response is equalised by setting the PMT gain to a common value and correcting the residual response of each cell to hadronic MIP particles offline.⁶¹ Electrons, positrons and photons reaching ECAL interact starting an electromagnetic shower. The mean longitudinal profile of the energy deposit by an electromagnetic shower is well described by a gamma distribution⁶²:

$$\left\langle \frac{1}{E} \frac{dE(t)}{dt} \right\rangle = \frac{(\beta t)^{\alpha-1} e^{-\beta t}}{\Gamma(\alpha)} \quad (1.20)$$

where $t = x/X_0$ is the shower depth in units of radiation length, $\beta \sim 0.5$ is the scaling parameter and α the shape parameter. The total thickness of the ECAL ($\sim 17 X_0$) allows the containment of 75% of the shower energy deposit for 1 TeV e^\pm . The energy of the incoming particle is measured applying corrections for the rear and lateral energy leakage, and for the anode efficiency, to the deposited energy. These corrections ensure the energy linearity to be under control to better than 1% up to 300 GeV. The calorimeter energy resolution $\sigma(E)/E$ has been measured during the test beams⁶³ (see Figure 21) and can be parametrized as a function of the particle energy E by:

$$\frac{\sigma(E)}{E} = \frac{10.4 \pm 0.2}{\sqrt{E(\text{GeV})}} \% (1.4 \pm 0.1) \% \quad (1.21)$$

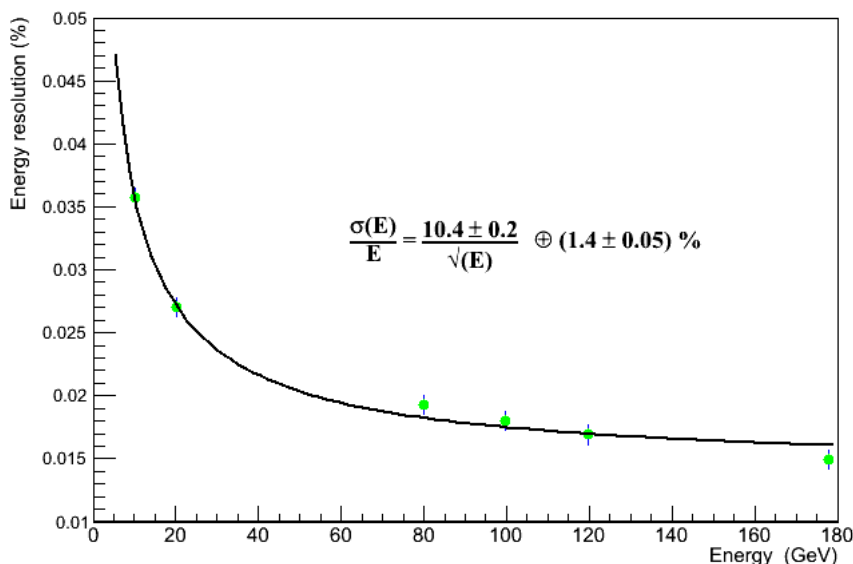


Figure 21 – ECAL energy resolution measured using e^\pm test beams for perpendicularly incident particles.

Source: [DI FALCO](#)⁶³

The ECAL 3D readout granularity allows the precise reconstruction of the shower axis and direction. The ECAL pointing accuracy is a crucial parameter for gamma ray astrophysics. The ECAL angular resolution has also been measured to be better than 1° for energies above 50 GeV.⁶⁴ The ECAL standalone trigger, whose efficiency for non-interacting photons is better than 99% at energies above 5 GeV, allows to measure photons inside the AMS field of view, which did not interact before the calorimeter. Given the amount of radiation length X_0 in front of the calorimeter, more than 60% of photons crossing the detector from the top reach directly the calorimeter without interactions. Photons that interact in the material before the ECAL are instead measured by the detection of $e^- - e^+$ pairs in the Silicon Tracker. The electromagnetic shower starting point, shape and the matching between the deposited energy in the ECAL and the rigidity measured by

the Tracker are used to identify e^\pm while rejecting the hadronic background. The ECAL proton rejection capabilities, measured directly from data, are shown in Figure 22.

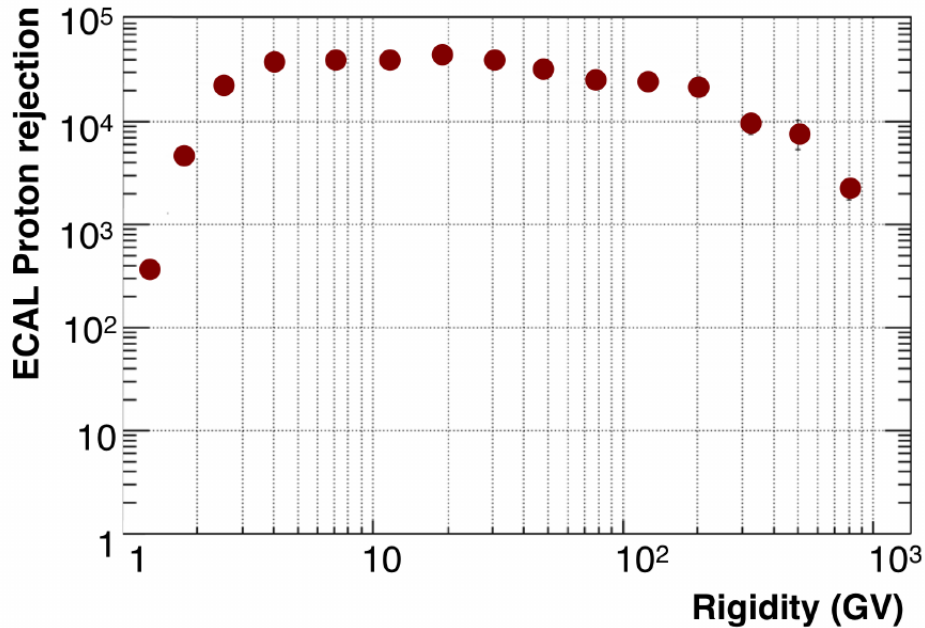


Figure 22 – Proton rejection measured from data collected in space using the ECAL shower topology analysis and the matching between the deposited energy in the ECAL and the rigidity measured by the Silicon Tracker. The efficiency of the selection for e^\pm is 90%. The proton rejection is above 10^4 in almost the whole energy range.

Source: [AGUILAR et al.¹](#)

1.2.7.1 Lepton-hadron separation with ECAL

The signal released in a calorimeter is different for leptons and protons.⁶⁵ When an electron (or a positron) reaches the first layer of ECAL, it starts to emit photons due to the bremsstrahlung. In turn, the photon produces an electron-positron pair through the interaction with the material. The secondary leptons produced can again emit photons. These two processes (bremsstrahlung and pair-production) continue until photons fall below the pair production threshold and energy losses of electrons due to ionisation starts to dominate over the losses due to bremsstrahlung. What has been produced in the end is an electromagnetic shower. The parameterization of the electromagnetic showers in a sampling calorimeter is given by Equation 1.20. When a proton reaches the calorimeter, the behaviour is different. Since the nuclear radiation length λ of the ECAL is 0.6 , $\sim 55\%$ of the protons go through the whole calorimeter losing their energy only through the ionisation process. These kind of protons arrived at ECAL as MIP and the energy that they deposit in the calorimeter is low ($\sim 200\text{-}400$ MeV). Removing the background constituted by MIP protons is trivial. A request on a minimum energy deposited in ECAL of 0.5 GeV or a minimum of 25 hits used for the shower reconstruction are sufficient

requests to remove proton MIP background. At higher energies protons produce a shower in the calorimeter. The hadronic shower has different characteristics compared to the electromagnetic. The hadronic showering process is dominated by a succession of inelastic hadronic interactions. These are characterized by multiparticle production (mostly charged pions and nucleons) and particle emission originating from nuclear decay of excited nuclei. Due to the generation of π^0 that decay into $\gamma\gamma$, there is also an electromagnetic component present in hadronic showers. The signals collected in the 1276 cells are combined to identify electromagnetic-like showers and reject hadronic-like ones. The variables useful for distinguishing between signal and background (like the transverse and longitudinal shower development and the shower maximum) are combined into a MultiVariate Approach (MVA), resulting into a Boosted Decision Tree (BDT).⁶⁶ The BDT has been trained on electrons and proton samples selected from ISS data, without using simulations. The classification tool used in this analysis, $ECAL_{BDT}$, is one of the official tools developed within the AMS-02 collaboration and it is included in the AMS-02 reconstruction software. It relies on 22 variables describing the longitudinal shower development and 39 variables describing the lateral shower development. An example of the $ECAL_{BDT}$ distribution is given in Figure 23.

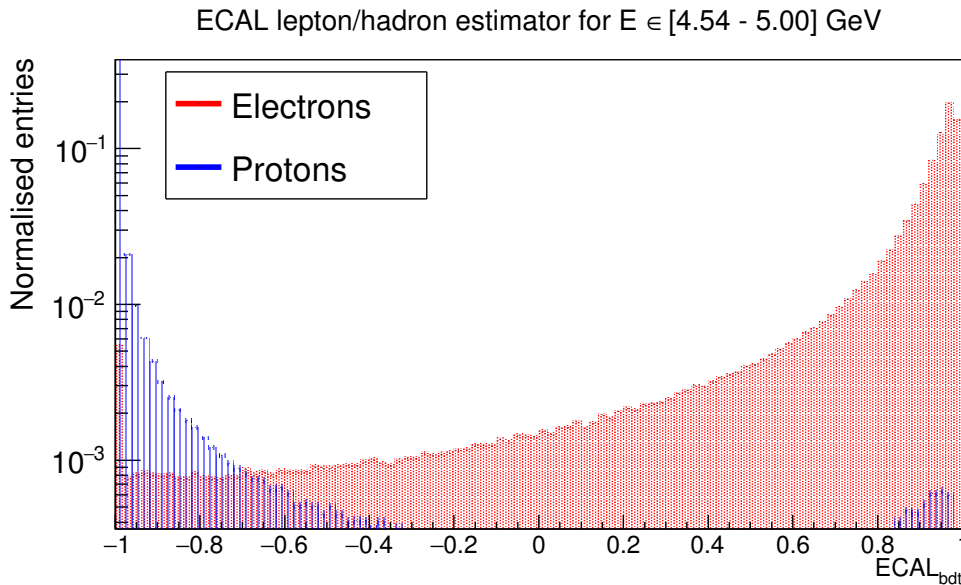


Figure 23 – $ECAL_{bdt}$ distribution example for electron-like events and proton-like events for the energy interval [4.54 - 5.00] GeV.

Source: By the author

2 ELECTRON AND POSITRON FLUX MEASUREMENT

The isotropic fluxes of electron and positron cosmic rays (ϕ_{e^-,e^+}) in the energy bin E of width ΔE is given by:

$$\phi_{e^-,e^+}(E, E + \Delta E) = \frac{N_{e^-,e^+}(E)}{A_{eff}(E)\epsilon(E)T(E)\Delta E} \quad (2.1)$$

Where N_{e^-,e^+} is the number of electrons/positrons measured in the interval E and $E + \Delta E$, A_{eff} the effective acceptance, ϵ the trigger efficiency and T the exposure time. The results presented in this section are obtained using data collected by the AMS-02 experiment between May 2011 and November 2016.

2.1 Event Selection

In order to select events that corresponds to a possible electron or positron event, an event selection is performed combining information collected in different sub-detectors, according to the following criteria:

- Charge cut: Since the analysis is focused on single charged particles, a cut on the charge measured by the inner layers of the Tracker is used. Only events whose absolute charge Z is in the interval : $0.3 < Z < 1.5$ are taken into account.
- ECAL shower exists: Only events that produces 1 or 2 showers inside the ECAL fiducial volume are considered. This criteria is crucial not only to ensure the quality of the energy reconstruction but since one of the methods to further separates the electrons/positrons from the proton background is to rely on a Boosted Decision Tree (BDT) that uses mostly the information measured by the ECAL shower.
- ECAL estimator selection: Only events whose estimator $ECAL_{BDT}$ is bigger than -0.8 are used. This cut is used to reduce the bulk of the proton background to achieve a better precision in the event counting. As it was discussed in section 1.2.7.1.
- Energy-rigidity matching: A cut on the ratio of the energy measured by the ECAL and the rigidity measured by the Tracker is applied to reject events with $E/|R| > 10$. Events with $E/|R| > 10$ are normally coupled with Bremsstrahlung and wrong sign reconstruction, which in turn increases charge confusion.
- Track extrapolation inside ECAL: Only events whose Tracker track extrapolation to the ECAL level are inside the calorimeter fiducial volume are used. This cut ensures that not only events that should hit the ECAL are considered, but also only the events that have enough distance from the borders of the calorimeter to produce

a shower that is fully contained inside the ECAL are taken into account. This cut requires that the distance in the x and y axis of the track extrapolation at the ECAL level to be smaller than 30.6 cm (2 cells away from the borders).

- ECAL-track matching: A cut on the distance between the Tracker track extrapolation on the ECAL level and the ECAL shower starting point is applied to ensure that both events are compatible with the same particle. The cut requires the distance to be smaller than 3.6 cm in the x direction and 7.2 cm in the y direction.
- Relativistic down-going particle: A cut in the variable $\beta = v/c$ measured by the TOF is used to not only restrict to events that are relativistic but also to only select events that are coming downwards from the top of the detector. The cut used requires $0.8 < \beta < 1.5$.
- Single Tracker track: Only events that produced a single Tracker track are considered. This cut is used to reduce the proton background that can generate secondary electrons inside the detector.
- Good track reconstruction: Only events that have a well reconstructed Tracker track are considered. In order to assure that, a cut on the χ^2 of the track reconstruction is applied. The cut requires $\chi_{x,y}^2 < 20$.
- Number of TRD hits and Helium background suppression: A minimum number of hits used in the TRD estimator TRD_{lhr} is required to ensure reliability of the estimator. The cut requires at least 8 hits. A constant cut on the TRD estimator for electron/Helium separation is used to further reduce Helium nuclei background.
- Live-time: A cut on the live-time of the detector, defined as the fraction of time during which the instrument is ready to detect and record an event, is used. The cut requires a minimum value of 0.5 to ensure that the live-time is long enough for the detection to be reliable. This cut also exclude events that were taken when the detector is crossing the South Atlantic Anomaly, a region of the Earth's magnetic field that is lower than its surroundings. This causes a higher rate of cosmic rays events in this region, that are normally not well measured since the detector are not able to handle the amount of events arriving at the same time, which in turn reduces the live-time in this region.

After the event selection, the resulting number of events is 21×10^7 , being mainly composed by electrons, positrons and protons.

2.2 Event counting method

The number of events is extracted by means of a Template-fit method using the RooFit package.⁶⁷ This strategy consists in extracting the number of electrons and positrons from the sample resulting from the event selection. To create the templates for the reference distributions cuts are applied directly in the preselected sample, using the information of the sub-detectors to define a pure sample of electrons and protons. The reference spectra are well described by a Novosibirsk (Novo) function,⁶⁸ which is defined as:

$$f(x) = N \exp \left[- \left(\frac{\ln \left(1 - \frac{x - x_p \eta}{\sigma} \right)}{\sqrt{2} \sigma_0} \right)^2 - \frac{\sigma_0^2}{2} \right] \quad (2.2)$$

where N is the normalization factor, x_p is the peak value, η is the asymmetry parameter, σ is the width and σ_0 is $(1/\sqrt{\ln 4}) \sinh^{-1}(\eta \sqrt{\ln 4})$. The rigidity sign is used to separate the samples of electrons and positrons for the fit. In this case, the major component of background is constituted by protons and Charge Confused (CC) protons (proton events which are reconstructed with wrong rigidity sign) in the samples of positive and negative rigidity, respectively. To define the reference templates, the cuts given in Table 1 are applied to the event selection sample. The fitting procedure is then performed on the TRD likelihood ratio (TRD_{lhr}) distribution discussed in Section 1.2.2.1, creating 3 different template distributions for each energy interval for electrons (signal), protons and CC protons (background).

Table 1 – Definition of the reference spectra for electrons, protons and CC protons. The different electron cuts applied in the $ECAL_{BDT}$ are to ensure that the sample is pure and had enough statistics.

	Electrons	Protons	CC protons
$ECAL_{BDT}$	> -0.8: 0.5 - 80 GeV, > -0.4: 80 - 400 GeV , > 0.2: 400 - 1000 GeV,	< -0.6	< -0.6
$E/ R $	> 0.5	< 0.5	< 0.5
R sign	-	+	-
Fit range	$0.1 < TRD_{lhr} < 0.8$	$0.65 < TRD_{lhr} < 1.5$	$0.7 < TRD_{lhr} < 2.0$

Source – By the author.

Examples of the distributions are given in Figures 24 and 25.

Positrons are expected to have the same signal as the electrons when detected by the TRD, thus the electron reference template, which has a smaller contamination from the background, is used for the fit. Examples of the resulting fits is shown in Figure 26.

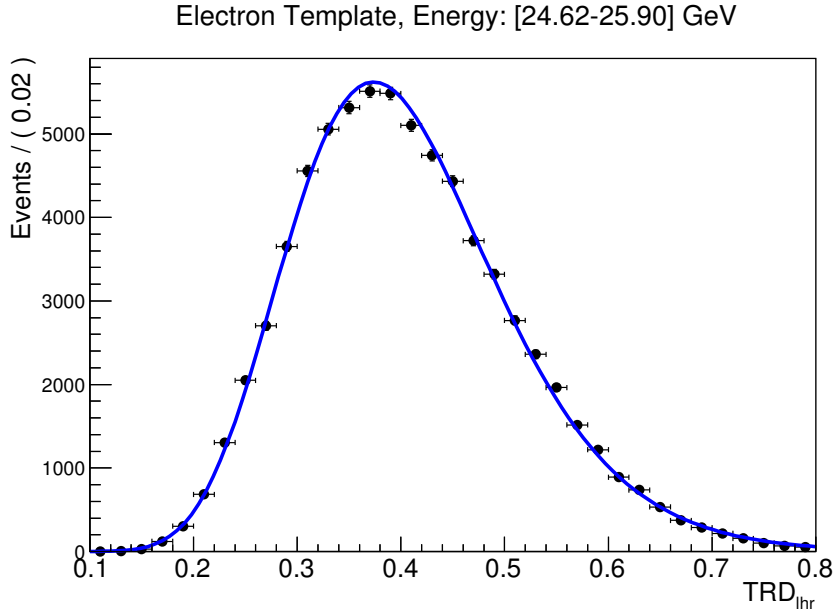


Figure 24 – Electron reference spectrum for the TRD_{thr} distribution for the energy interval [24.62 - 25.90]GeV.

Source: By the author

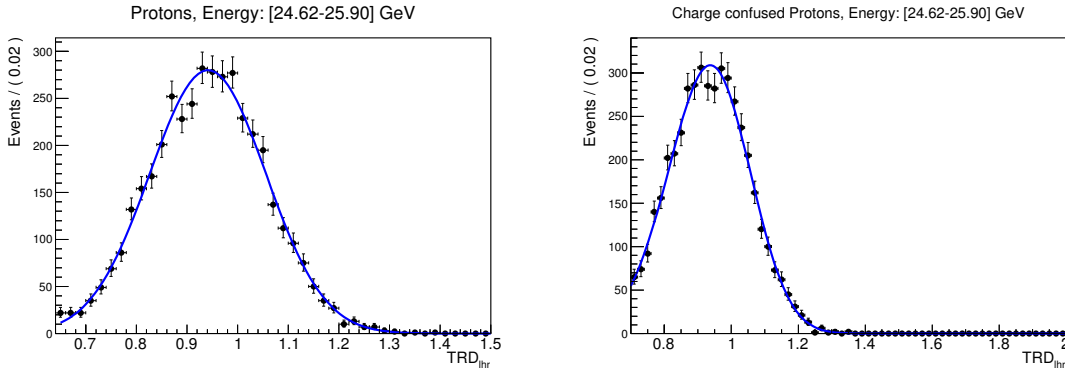


Figure 25 – Proton (left) and CC proton (right) reference spectrum for the TRD_{thr} distribution for the energy interval [24.62 - 25.90]GeV.

Source: By the author

The number of events obtained with the Template-fit needs to be corrected for the charge confusion, i.e, electrons that are reconstructed with wrong charge and identified as positrons and vice-versa. This issue is addressed by correcting the number of measured positive and negative events n_{obs}^{\pm} by a factor to recover the true number of events n_{true}^{\pm} . In order to do that, the following quantity is defined:

$$cc(\Delta E) = \frac{n_{MC}^{+}(\Delta E)}{n_{MC}^{+}(\Delta E) + n_{MC}^{-}(\Delta E)} \quad (2.3)$$

which $n_{MC}^{+}(\Delta E)$ and $n_{MC}^{-}(\Delta E)$ are the number of events in the Monte Carlo electron sample that, after passing the requirements of the event selection, are reconstructed with

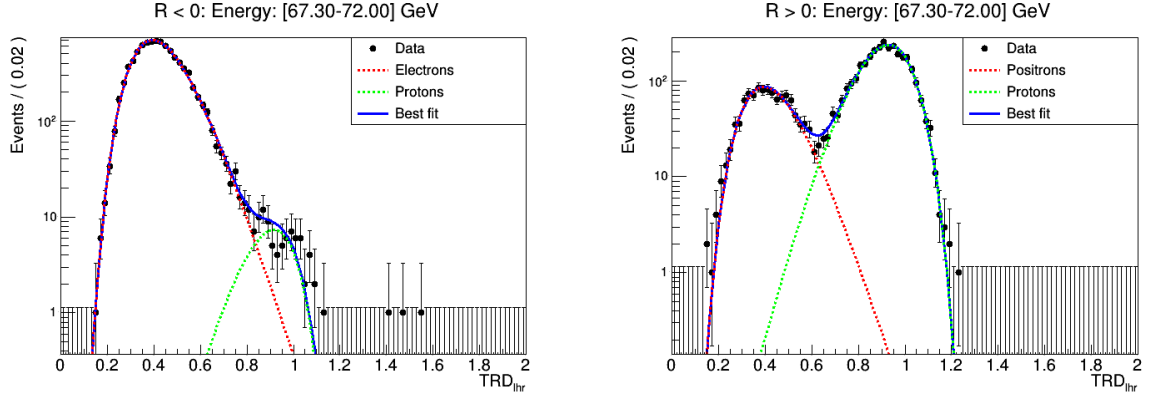


Figure 26 – Fit example on data for both electrons (left) and positrons (right) for the energy interval of [67.30-72.00] GeV.

Source: By the author

positive or negative rigidity in the energy interval ΔE . The energy dependence of CC is shown in Figure 27.

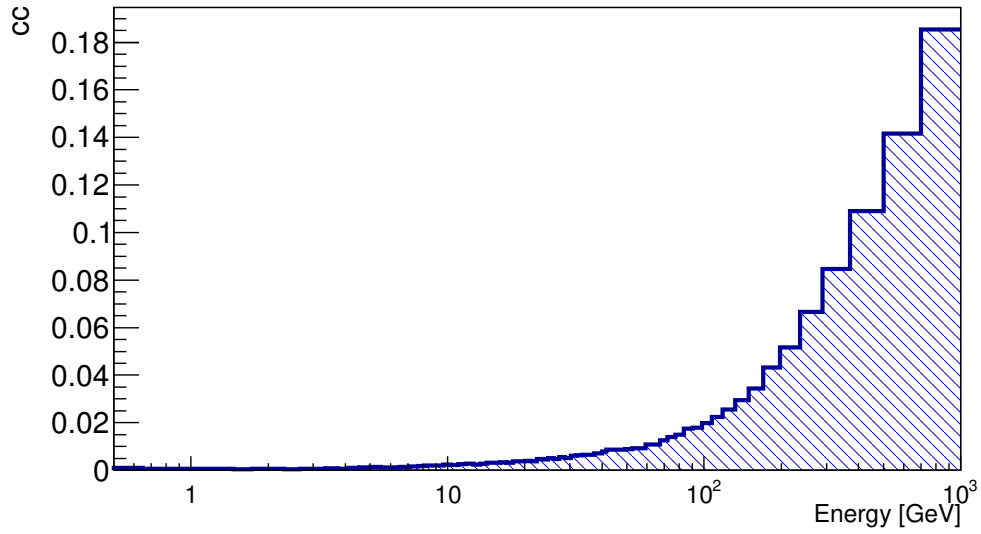


Figure 27 – Charge confusion cc defined in equation 2.3 based in MC simulation as a function of the energy.

Source: By the author

the connection between n_{obs}^{\pm} and n_{true}^{\pm} for electrons and positrons is:

$$\begin{aligned} n_{obs}^+ &= n_{true}^+ \cdot (1 - cc) + n_{true}^- \cdot cc \\ n_{obs}^- &= n_{true}^- \cdot (1 - cc) + n_{true}^+ \cdot cc \end{aligned} \quad (2.4)$$

inverting equation (2.4) results:

$$\begin{aligned} n_{true}^+ &= \frac{n_{obs}^+ \cdot (1 - cc) - n_{obs}^- \cdot cc}{1 - 2cc} \\ n_{true}^- &= \frac{n_{obs}^- \cdot (1 - cc) - n_{obs}^+ \cdot cc}{1 - 2cc} \end{aligned} \quad (2.5)$$

the fraction of wrong reconstructed events, δ^\pm , is:

$$\delta^\pm = \frac{n_{true}^\pm - n_{obs}^\pm}{n_{true}^\pm} \quad (2.6)$$

which in terms of cc is written as:

$$\delta^\pm = cc \left(1 - \frac{n_{true}^\mp}{n_{true}^\pm} \right). \quad (2.7)$$

At around 10 GeV, cc is 0.005. For this same energy, the ratio of positrons and electrons is around 0.05. Substituting these values in Equation 2.7 results in $\delta^+ \sim 10\%$ and $\delta^- \sim 0.5\%$. While this correction is less important for the number of electrons, it makes a huge difference in the real number of positrons as seen in Figure 28.

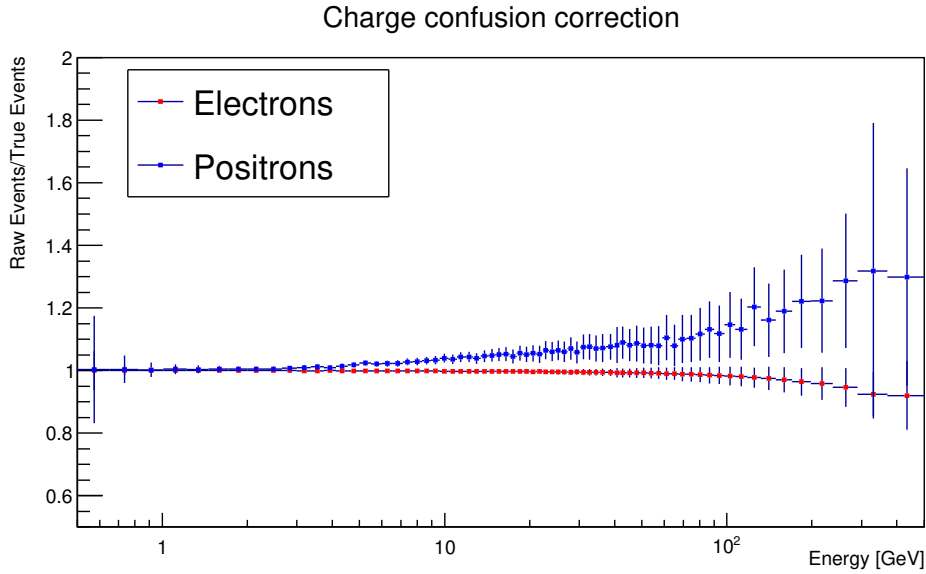


Figure 28 – Ratio between the measured number of events and the corrected number of events. The correction for electrons is as high 15% at 500 GeV while the correction for positrons the correction amount to 30% at 500 GeV.

Source: By the author

2.3 Flux normalisation

In the following section will be described all the correction factors that are needed to be applied to the number of measured signal events in order normalise the number of events for the actual detection area, the selection and trigger efficiencies as well as the exposure time.

2.4 Trigger Efficiency

The main purpose of the AMS-02 trigger logic is to take a fast and efficient decision to start the data acquisition of the signal in the sub-detectors. The decision is tuned to the particle properties. The AMS trigger uses the combined information coming from the TOF, ACC and ECAL sub-detectors, which are analysed inside a dedicated electronics board. The processing of all the different signals takes about $200 \mu\text{s}$ which represents a significant contribution to the dead time of the experiment. That is, the time interval during which the detector is set into a “busy” state and is not able to detect new particles. To minimise this dead time, a complex decision tree architecture is adopted with 2 different stages: the *Fast and Level 1 trigger logic*. Only if the conditions of the Fast trigger stage are satisfied, the Level 1 trigger is evaluated. A brief description of the 2 stages are as follows:

- Fast Trigger: The Fast Trigger (FT) logic is used to make fast decisions that do not contribute to the dead time and eventually activate the Level 1 trigger logic evaluation.
- Level 1: After the existence of a FT is confirmed, the board enters the Level 1 (LVL1) logic evaluation, which takes exactly $1 \mu\text{s}$. The following conditions are then tested:
 - LV1-0: the FT opens a 240 ns gate to latch the signal of charged particles. Only events passing at least 3 out of 4 TOF planes are accepted. The first condition is used to construct the unbiased trigger sample.
 - LV1-1: a more restrictive version of LV1-0 takes into account single charged particles by considering only events with no ACC counts and passing all 4 out of 4 TOF planes are accepted.
 - LV1-2: builds the trigger used for ions with looser conditions on LV1-1 by accepting events whose ACC is less than 5 but still only considering events passing all TOF planes with signal higher than the Super-High Threshold (SHT), which is associated with heavier particles like nuclei.
 - LV1-3: is the slow trigger for heavy ions, which uses the same conditions for LV1-2 but with FT gate opened for a longer period of 640 ns .
 - LV1-4: the electron trigger, uses the same approach as the restricted LV1-0 with 4 out of 4 TOF planes, but also considers the ECAL signal requiring a

minimum amount of neighbouring cells whose energy deposition is higher than the threshold in both x and y super-layers.

- LV1-5: forms the photon trigger, which requires a shower constructed in the ECAL using the angular information for non converting photons detected only in the ECAL.

The triggers LV1-[1-5] are called "Physics Triggers" (PT), since they consider the physical properties of the events that passes through the detector. Only the LV1-0 makes no difference to the type of particle, being then called "Unbiased Trigger" (UT). The trigger efficiency is defined as follows:

$$\epsilon_{trigger} = \frac{N_{physics}}{N_{physics} + 100N_{unb}} \quad (2.8)$$

where $N_{physics}$ is the number of events with at least 1 PT and N_{unb} the number of events that only have the UT. The factor 100 multiplying N_{unb} arises from the fact that this stage is checked once every 100 events in order to decrease the dead time. The result of the trigger efficiency can be observed in Figure 29 as a function of the energy, being the same for both positrons and electrons since both share the same trigger definitions. The trigger efficiency increases with energy until around 2 GeV where it becomes 100% efficient.

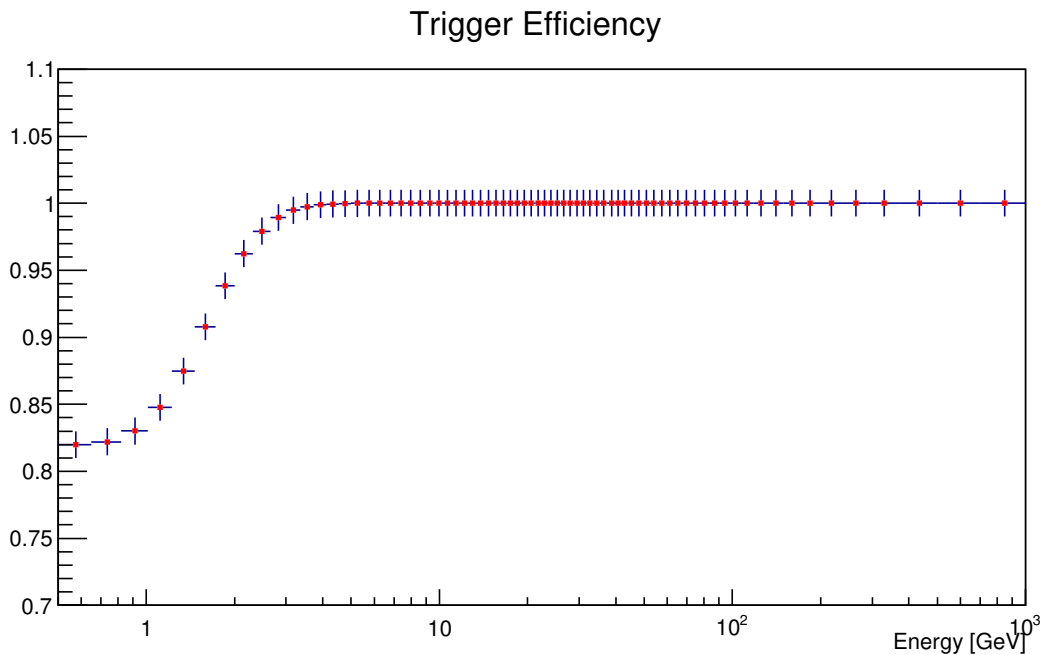


Figure 29 – Trigger efficiency for leptons as a function of the energy.

Source: By the author

2.5 Exposure Time

The number of signal events have to be corrected for the exposure time, i.e. the number of seconds in which the detector was capable of receiving new triggers. Besides this, commission periods such as the TRD gas refill, ISS docking or undocking and times in which the ISS itself enters the field of view of the detector have been removed from the data sample. Given the structure of the magnetic field of the Earth, the exposure time is rigidity dependent, and hence energy dependent, since it also includes the geomagnetic cutoff explained in Section 1.1.4. Given a particular position of the detector inside the magnetic field of the Earth, only particles whose energy is higher than the cutoff are able to be detected by the experiment, being the events with rigidity smaller than the cutoff more likely to be trapped particles in the magnetic field. Since the measurement of the e^\pm is binned, to apply the cut for both positrons and electrons, the maximum value between the positive and negative values of $R_c^\pm(\theta, \phi)$, defined in Equation 1.15, are taken. Hence, the effective cutoff used, $R_{max}(\theta, \phi)$, is defined as:

$$R_{max}(\theta, \phi) = \max\{R_c^+(\theta, \phi), R_{cutoff}^-(\theta, \phi)\} \quad (2.9)$$

The result of the exposure time as a function of the energy are shown in Figure 30.

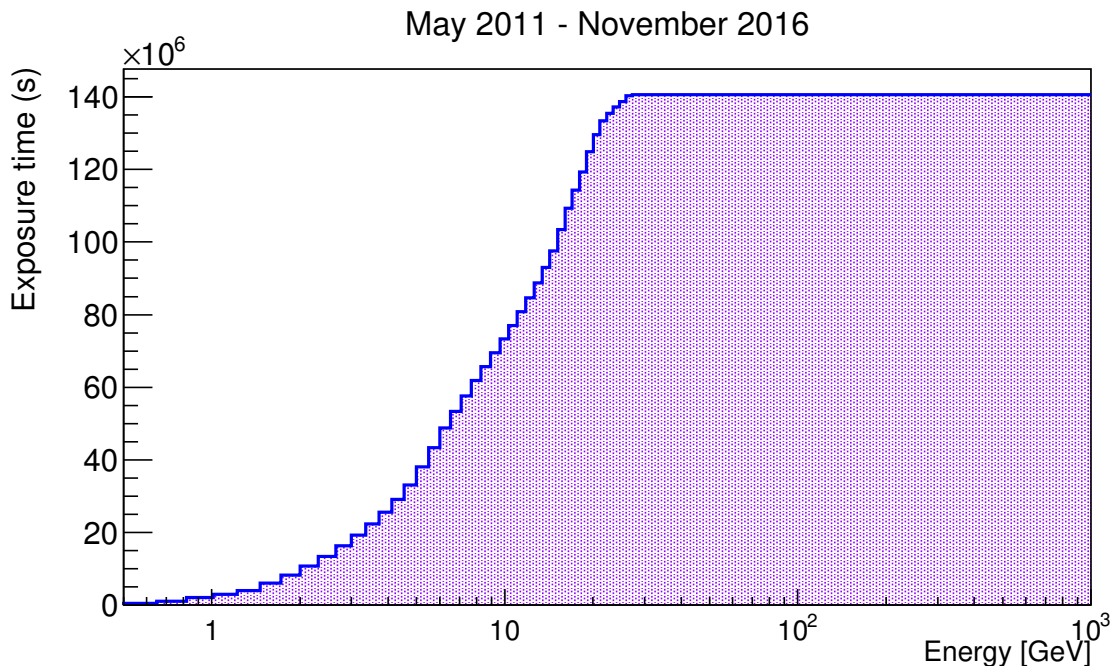


Figure 30 – Exposure time as a function of the energy, for the data taking period included in this analysis, i.e, May 2011 up to November 2016.

Source: By the author

Above around 30 GeV the exposure time is no longer energy dependent, and corresponds to approximately 80% of the time of the 66 months that comprises this analysis.

2.6 Acceptance

The detector geometry and the interactions experienced by the incoming particles within the detector material have to be correctly taken into account to retrieve the value of the real incident flux. The normalisation of the measured number of leptons to the flux on top of the detector is determined by the acceptance factor $A_{eff}(E)$. The effective acceptance A_{eff} is defined as follows:

$$A_{eff}(E) = A_{MC}(E)(1 + \delta(E)) \quad (2.10)$$

where A_{MC} is the Monte Carlo (MC) simulation acceptance and the factor $1 + \delta$ the acceptance correction due to possible discrepancies between the data and MC. The simulations of the AMS detector performance are done by producing the simulated events using all available information about AMS geometry, its environmental conditions and electronics based on the Geant4 package.⁶⁹

The term A_{MC} takes into account the event selection efficiencies as well as the geometrical factor given as:

$$A_{MC}(E) = \frac{N_{sel}(E)}{N_{gen}(E)} \cdot G \quad (2.11)$$

$N_{gen}(E)$ is the number of events that were generated in the MC sample, $N_{sel}(E)$ is the number of events that passes the same event selection that is applied to the data and $G = \pi l^2$ is the geometrical factor representing the generation surface for the MC sample. The MC sample used in this analysis is generated in a square box of side $l = 3.9$ m, which in turn makes $G \approx 47.78 \text{ m}^2\text{sr}$. The results for A_{MC} are shown in Figure 31. The low values at low energies are mostly due to a cut applied to reject events whose Tracker track matches the ECAL shower, since at low energies the bending caused by the magnetic field is higher. A smooth polynomial fit was used to take into account the statistical fluctuations. The correction $(1 + \delta(E))$ is used to correct any discrepancies between the data and MC simulation, since the simulation itself is not perfect. For each cut that was applied in the event selection, a correction called $K_i(E)$ for each cut i is defined as:

$$K_i(E) = \frac{\epsilon_{i,data}(E)}{\epsilon_{i,MC}(E)} \quad (2.12)$$

in which ϵ_{data} and ϵ_{MC} are the efficiencies of the cuts for both data and MC samples. To measure the efficiencies, a control sample of pure electrons has to be chosen from the data. Selection requirements based on the measurements of the same sub-detector, like the Tracker track reconstruction efficiency and single track requirement, are correlated. To properly take into account the correlations between different cuts and to avoid a biased result, the control sample for each given selection requirement is estimated using a events that does not make use of the sub-detector under study. For the aforementioned example, the control sample will be defined without requirements on the signals collected by the tracker.

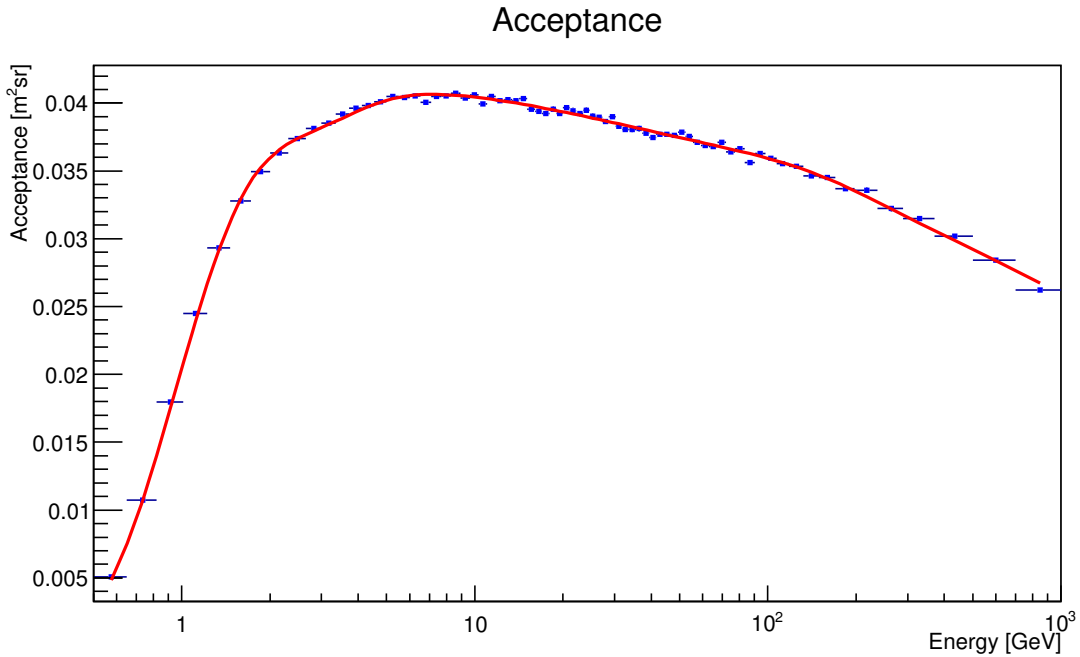


Figure 31 – Selection acceptance based on MC simulation as a function of the generated MC energy. Smoothed polynomial fit performed to take into account the statistical fluctuations

Source: By the author

The total correction is then given by the multiplication of each correction $K_i(E)$:

$$(1 + \delta(E)) = \prod_i K_i(E) \quad (2.13)$$

A clean sample of electrons with enough events to calculate the efficiencies with a high degree of accuracy is increasingly difficult to attain at higher energies. This is even more evident for corrections such as the Tracker track efficiency, since no requirements on the Tracker detector can be used to define the control sample, resulting in signs of proton contamination at higher energies. To address this issue, a log-linear fit is performed in the total correction in the energy range of [0.5 - 200] GeV, since the intrinsic discrepancy between data and MC for lepton selection is not expected to diverge at high energies. The correction then is extrapolated for higher energies. The efficiencies for both data and MC and the correction are shown in Figures 32 - 40.

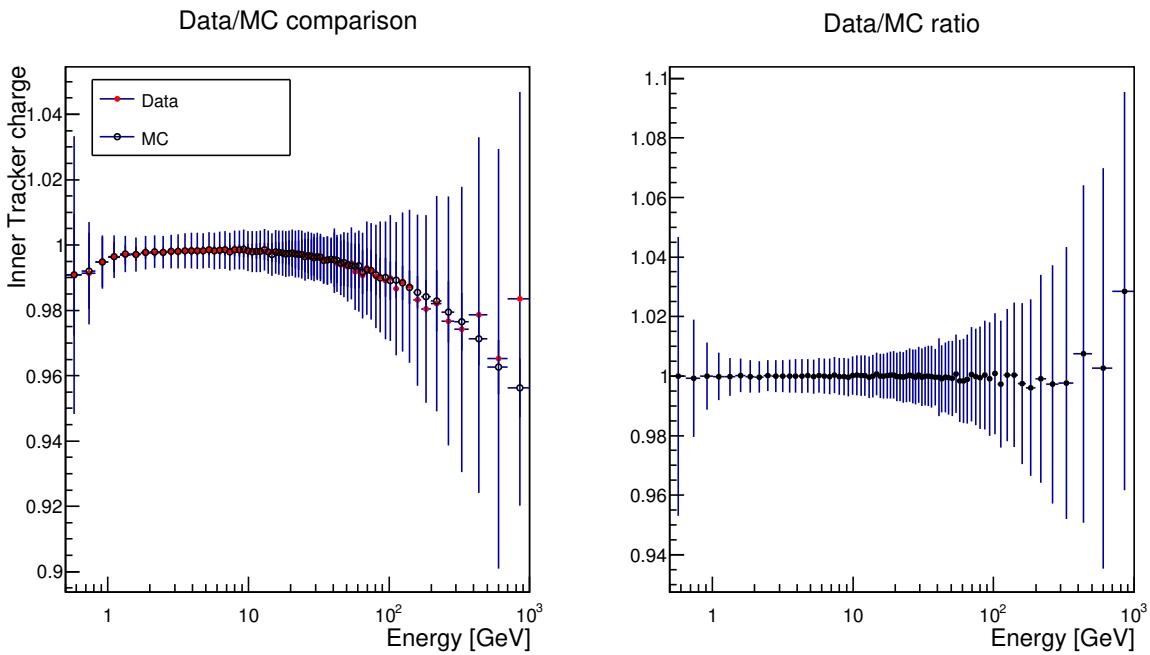


Figure 32 – **Left**: Charge cut efficiencies for both data and MC. **Right**: correction factor $K(E)$ defined in 2.12

Source: By the author

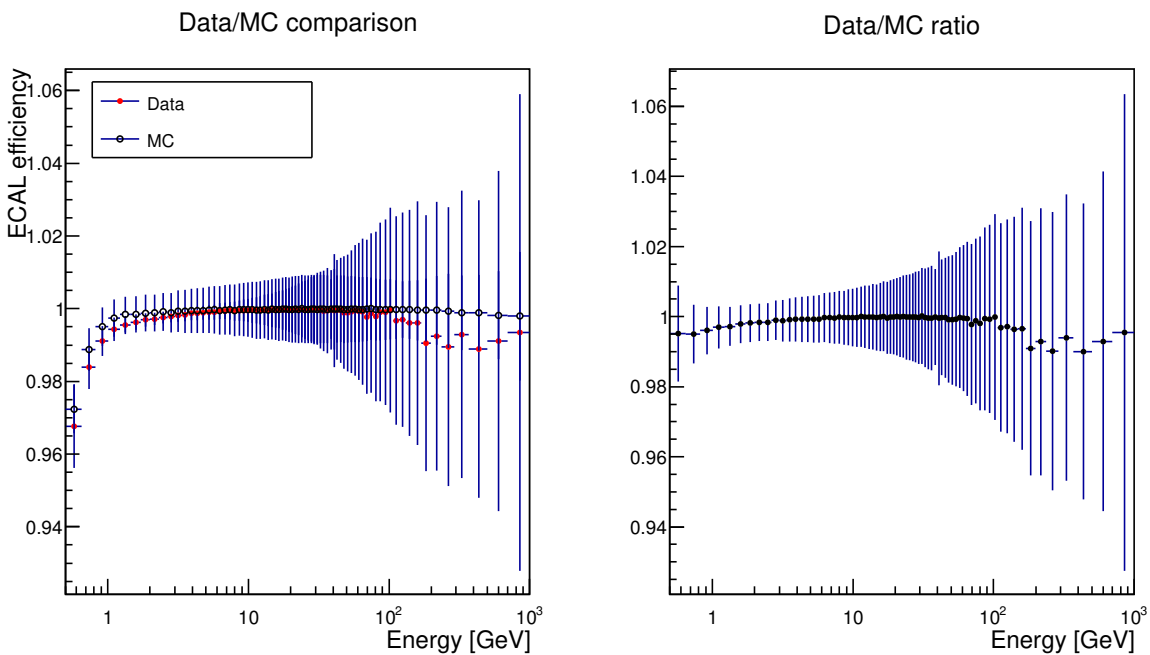


Figure 33 – **Left**: ECAL reconstruction efficiencies for both data and MC. **Right**: correction factor $K(E)$ defined in 2.12

Source: By the author

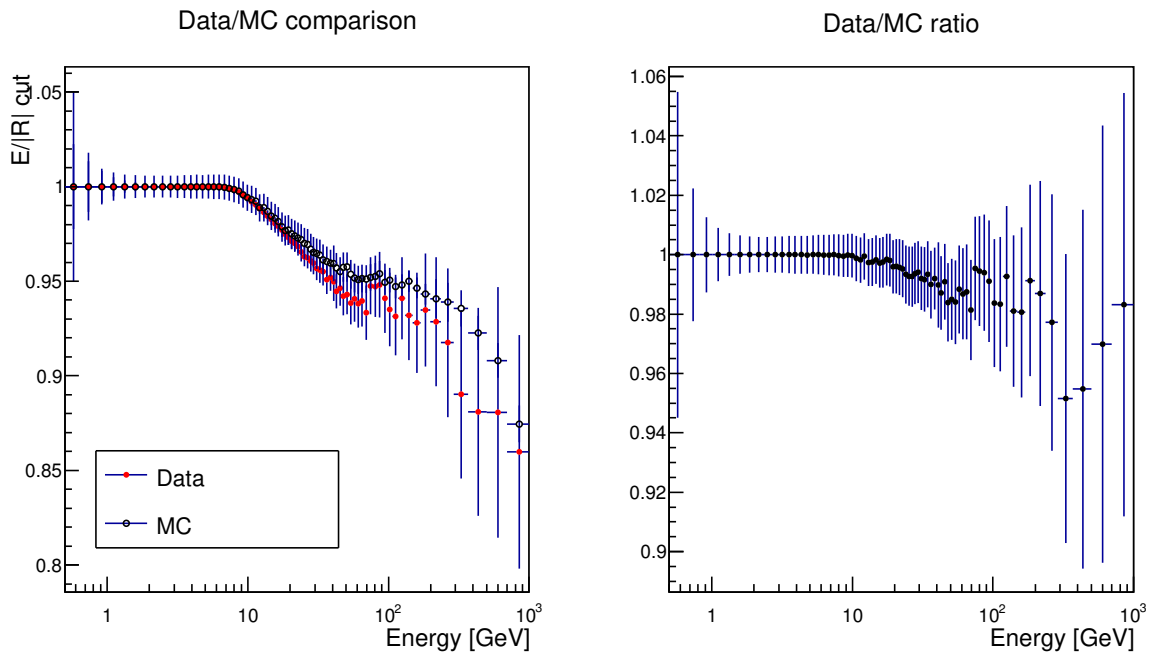


Figure 34 – **Left:** $E/|R|_{\text{cut}}$ efficiencies for both data and MC. **Right:** correction factor $K(E)$ defined in 2.12

Source: By the author

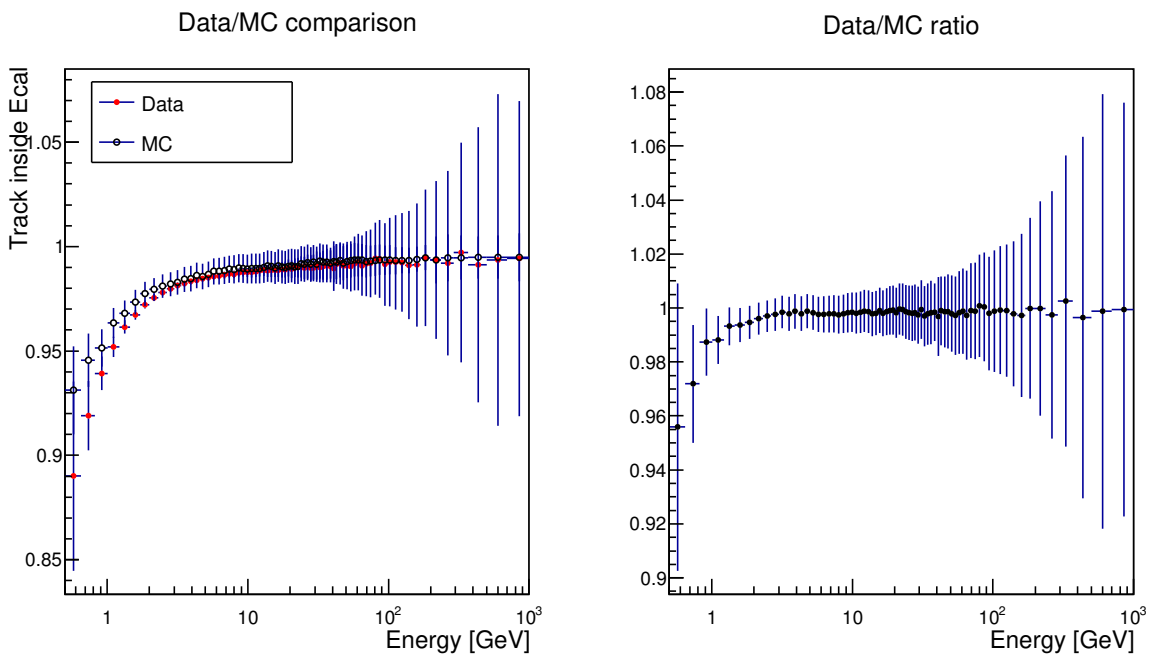


Figure 35 – **Left:** Tracker Track extrapolation efficiencies for both data and MC. **Right:** correction factor $K(E)$ defined in 2.12

Source: By the author

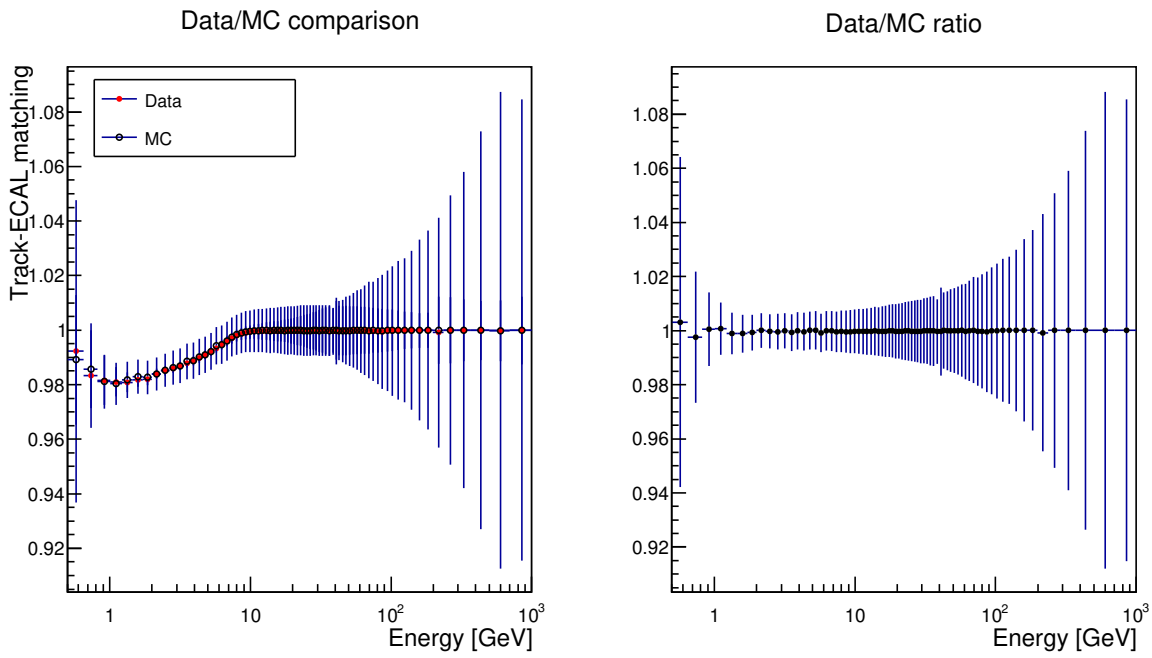


Figure 36 – **Left:** ECAL-track matching cut efficiencies for both data and MC. **Right:** correction factor $K(E)$ defined in 2.12

Source: By the author

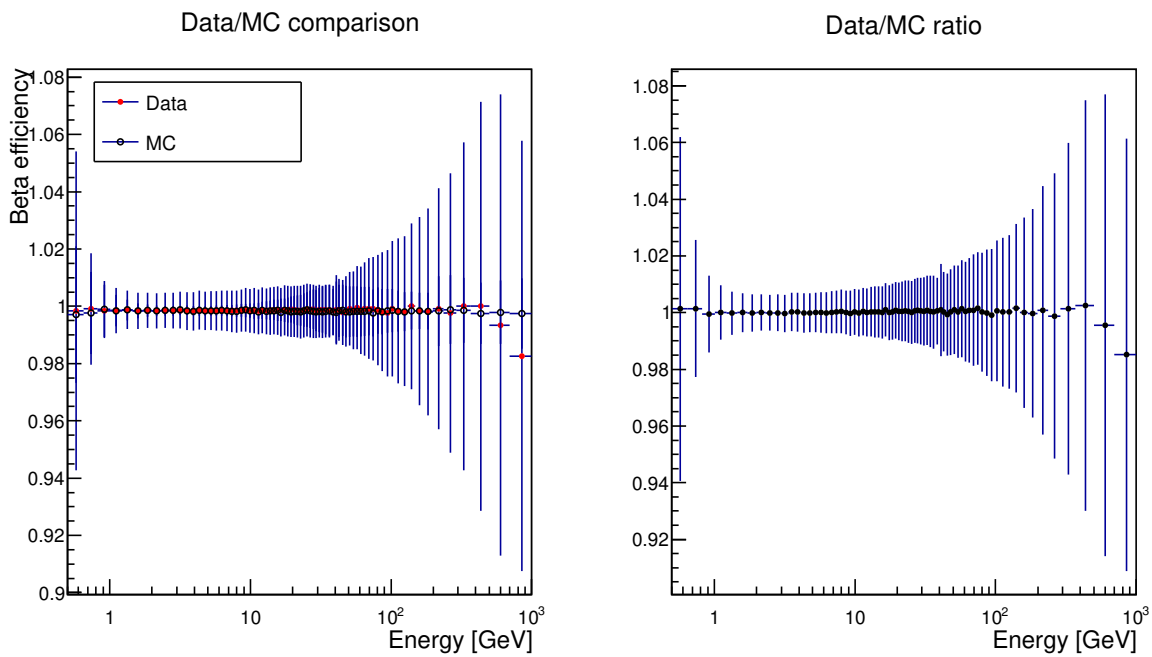


Figure 37 – **Left:** β cut efficiencies for both data and MC. **Right:** correction factor $K(E)$ defined in 2.12

Source: By the author

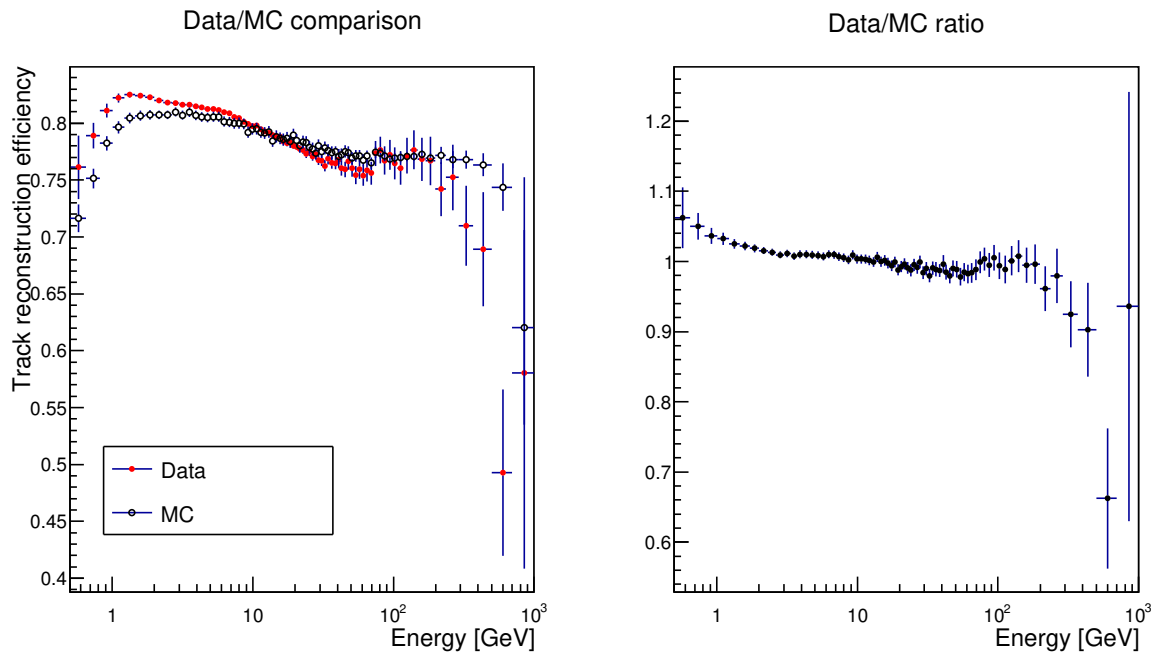


Figure 38 – **Left:** Good track reconstruction cut efficiencies for both data and MC. **Right:** correction factor $K(E)$ defined in 2.12

Source: By the author

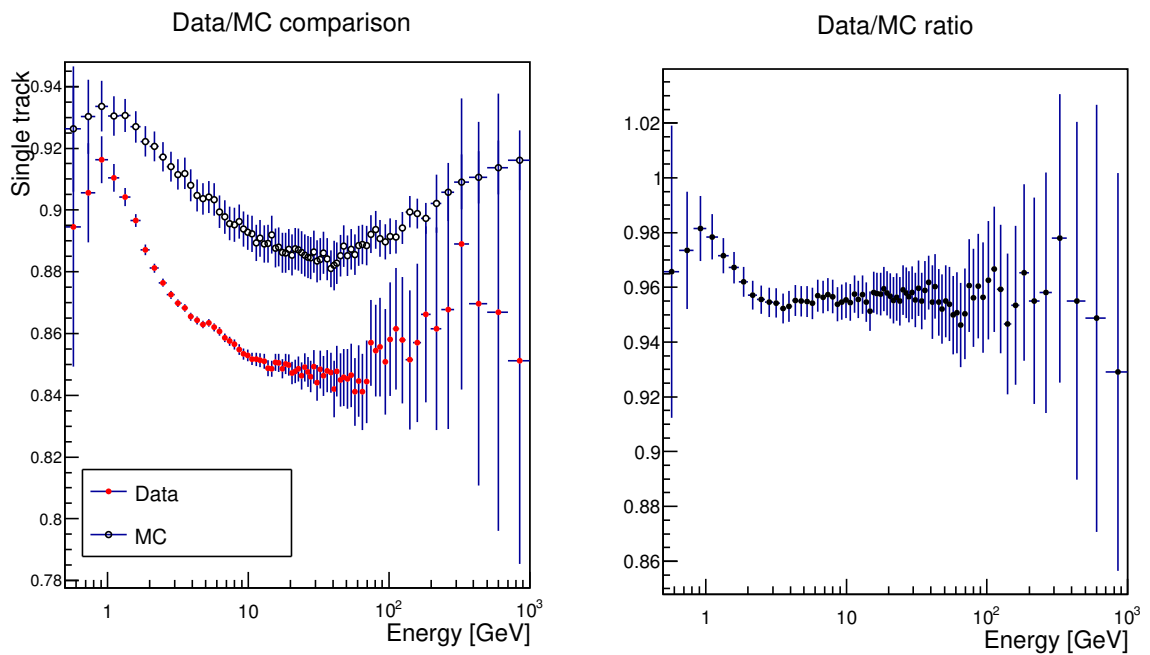


Figure 39 – **Left:** Single Tracker track efficiencies for both data and MC. **Right:** correction factor $K(E)$ defined in 2.12

Source: By the author

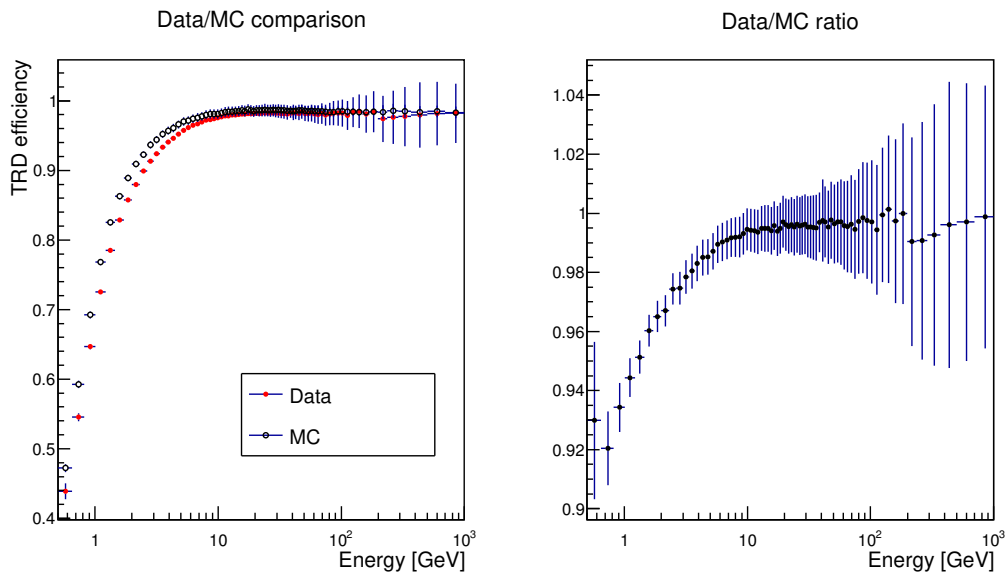


Figure 40 – **Left:** TRD cut efficiencies for both data and MC. **Right:** correction factor $K(E)$ defined in 2.12

Source: By the author

The $ECAL_{BDT}$ agreement between data and MC is poor at higher energies as exemplified in Figure 41.

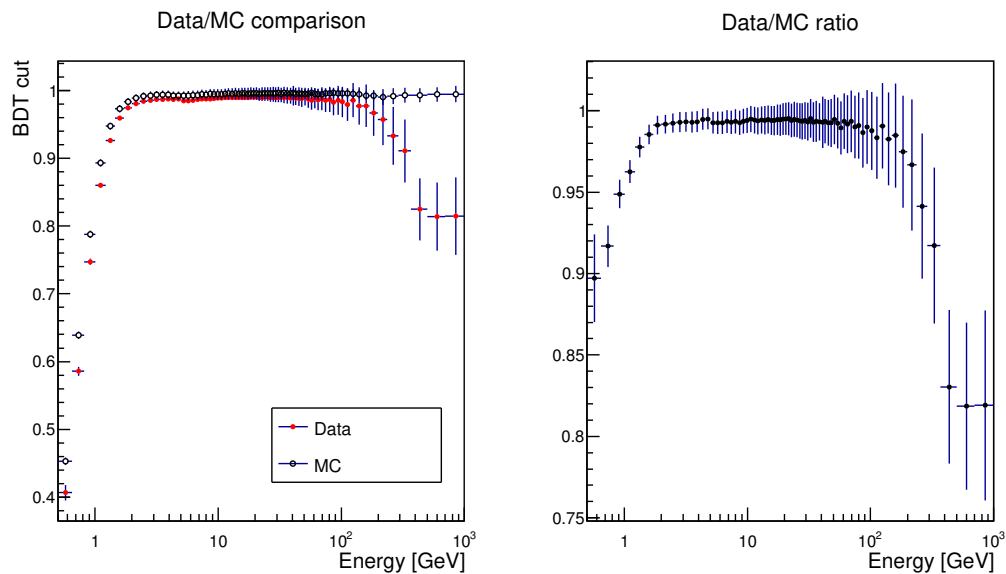


Figure 41 – **Left:** $ECAL_{BDT}$ cut efficiencies for both data and MC. **Right:** correction factor $K(E)$ defined in 2.12

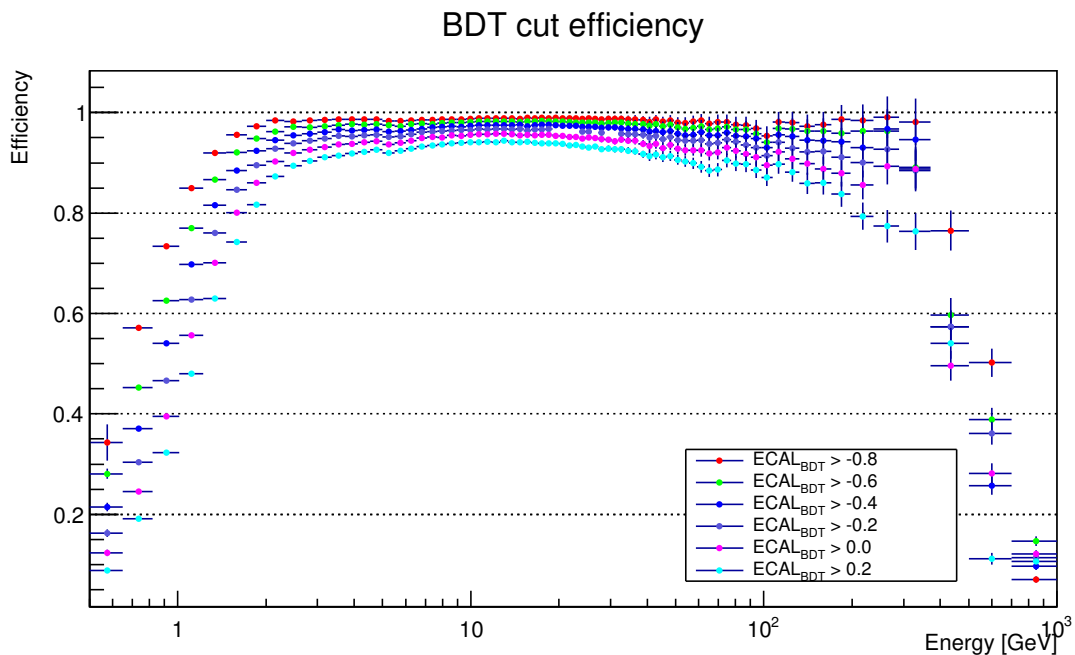
Source: By the author

The description of the shower development in the MC simulation is not accurate enough to provide a satisfactory agreement. The agreement improves at low energies, but the unphysical nature of the $ECAL_{BDT}$ classifier prevents any safe extrapolation at higher

energies. Besides that, without being able to use the *ECAL* detector to select leptons, the control sample efficiency itself gets spoiled by the proton background. To achieve a more realistic result, the *ECALBDT* efficiency is investigated for different cuts, and defined as:

$$\epsilon_{BDT} = N_{e^-}(x)/N_{e^-} \quad (2.14)$$

where $N_{e^-}(x)$ is the number of electron with $ECALBDT > x$ selected from the data sample of electrons N_{e^-} . The main difference is that to count the number of events $N_{e^-}(x)$ and N_{e^-} , the Template-fit method is adopted, which in turn takes into account the contamination caused by protons. The result is given in Figure 42.



Source: By the author

The resulting correction $(1 + \delta)$ is shown in Figure 43, without the $ECAL_{BDT}$ correction which is applied separately. The absolute value of δ increases up to 2 GeV, and smoothly decreases as the energy increases.

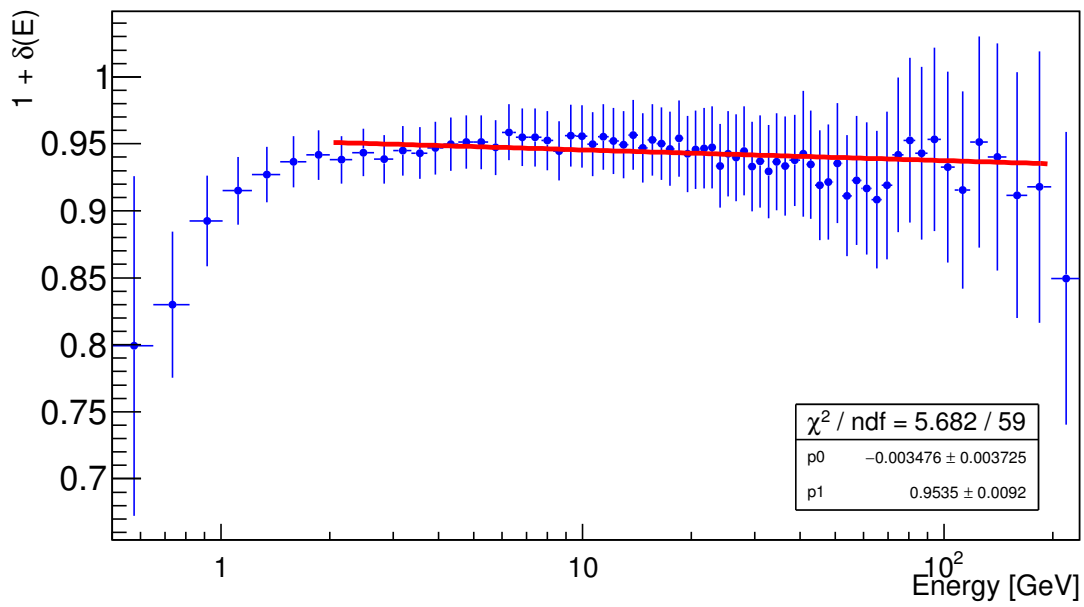


Figure 43 – Correction for Data/MC. Log-linear fit performed in the energy range of [0.5 - 200] GeV and extrapolated for higher energies.

Source: By the author

2.7 Flux Results

Along this chapter, the fluxes will be presented multiplied by a power of the energy to better appreciate the spectral features. The representative value for the bin energy, \tilde{E} , has been evaluated as explained by,⁷⁰ with an input power law spectrum $\Phi \propto E^\gamma$ as follows:

$$\tilde{E} = \left(\frac{E_{max}^{1-\gamma} - E_{min}^{1-\gamma}}{(1-\gamma)(E_{max} - E_{min})} \right)^{-\frac{1}{\gamma}} \quad (2.15)$$

where E_{min} and E_{max} represent the minimum and maximum energy of the bin and a spectral index $\gamma = 3$, representative of the e^\pm spectra has been assumed. The measured cosmic ray electron and positron fluxes are shown in Figures 44, 45, 46 and 47 as a function of energy. The fluxes are re-scaled to the cube of the energy. Figures 44 and 45 show the flux measurements obtained using the same data set that was used in the AMS-02 publication,³ where data collected between May 2011 and November 2013 were used. The left plots show the AMS-02 publication (full dots) together with the result of this analysis (empty dots), while the right plots the ratio between the two measurements.

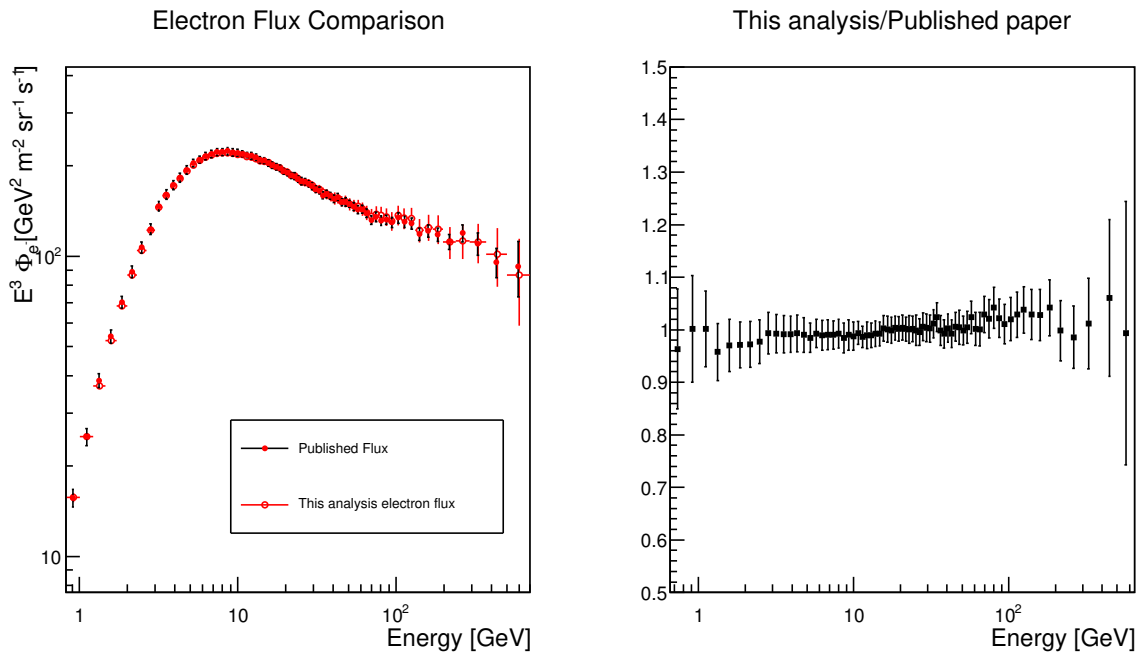


Figure 44 – **Left:** Electron flux reconstruction using the same data set as the last publication by the AMS-02 collaboration. **Right:** Ratio between this thesis result and published.

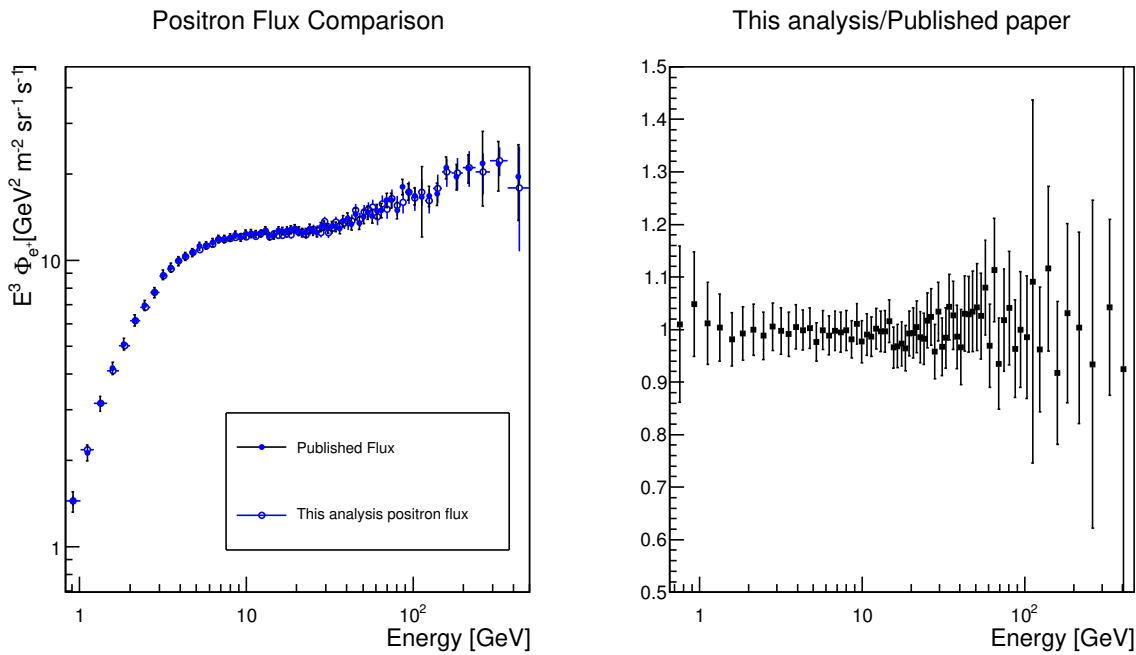


Figure 45 – **Left:** Positron flux reconstruction using the same data set as the last publication by the AMS-02 collaboration. **Right:** Ratio between this thesis result and published.

Source: By the author

Figures 46 and 47 show the cosmic ray electron and positron flux measured with an extended data set, including events collected during 66 months, up to November 2016. This new data set allows to extend the measurement with high statistics up to 1 TeV for electrons and to 700 GeV for positrons, compared to the explored range with respect to the previous published AMS-02 measurement. The left plots show the AMS-02 published results (full dots), together with the result of this analysis (empty dots), and the right plots show the ratio between the two measurements. A discrepancy at low energy is visible for electrons, but not for positrons: the electron flux is systematically lower than the AMS-02 publication. This effect hints to a possible charge effect in the solar modulation. This difference will be investigated in the following sections.

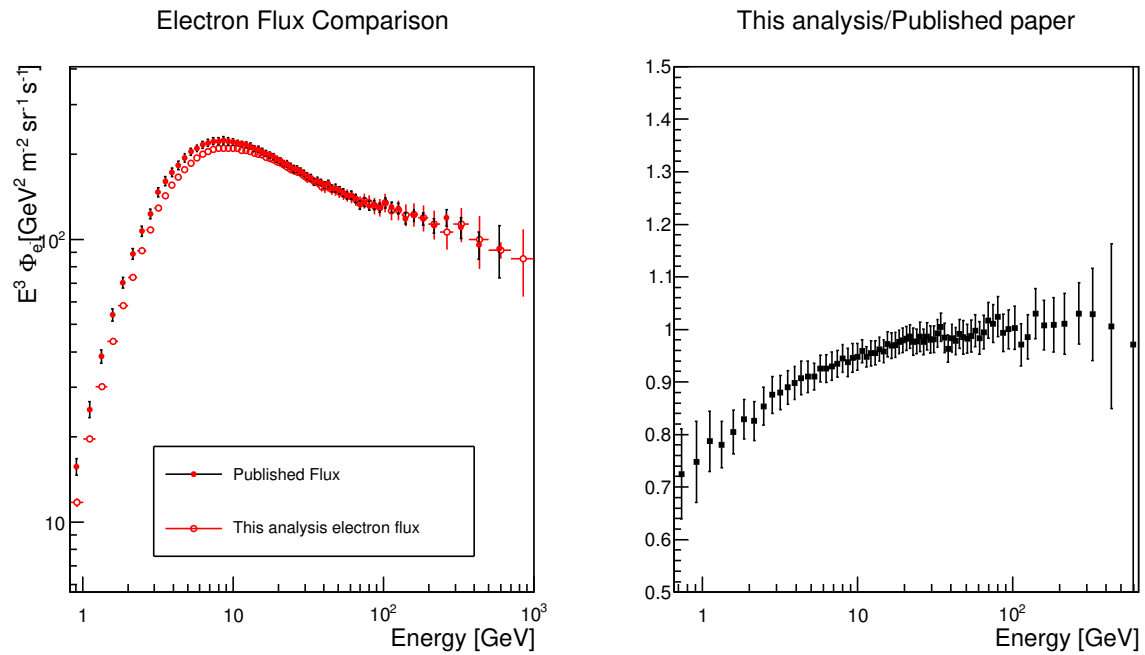


Figure 46 – **Left:** Electron flux reconstruction using 66 months of data compared to the publication. **Right:** Ratio between this thesis result and published. For energies lower than 30 GeV the ratio deviates from the published paper up to 30 % due to solar modulation

Source: By the author

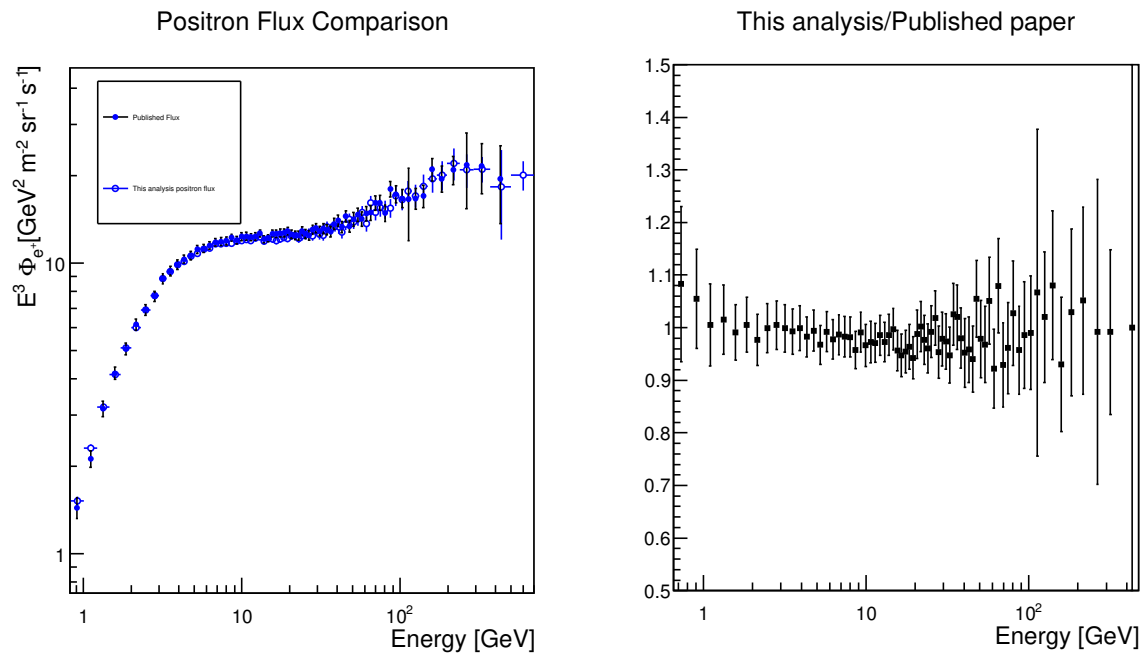


Figure 47 – **Left:** Positron flux reconstruction using 66 months of data compared to the publication. **Right:** Ratio between this thesis result and published. No deviation bigger than 10% is observed.

Source: By the author

3 ELECTRON AND POSITRON FLUXES AS A FUNCTION OF TIME

The second part of this work is dedicated to the measurement of the cosmic ray electron and positron fluxes as a function of time for energies smaller than 40 GeV, i.e, the energy interval in which solar effects are still relevant in the measurement of cosmic ray fluxes. Given the large acceptance and exposure time, the flux measurement is performed dividing the data-set in 74 time bins. For this analysis, each time bin has a width of 27 days, known as Bartels rotation,⁷¹ namely a serial count that numbers the apparent rotations of the sun as viewed from Earth, and is used to track certain recurring or shifting patterns of solar activity.

CRs of all species encounter a turbulent solar wind with an embedded heliospheric magnetic field when entering the heliosphere. This leads to significant global and temporal variations in their intensity and in their energy as a function of position inside the heliosphere. This effect is stronger in low energy CRs, decreasing in intensity as the energy increases. The analysis itself is quite similar as the analysis that was performed on the previous section. The main difference is that now is necessary to address the quantities in equation (2.1) that are also time-dependent. The new equation to consider in this case is then:

$$\phi(E, E + \Delta E, t) = \frac{N(E, t)}{A_{eff}(E, t)\epsilon(E, t)T(E, t)\Delta E} \quad (3.1)$$

each term of equation (3.1) will be described in the following section.

3.1 Time dependent event counting

The Template-fit method is used to compute the number of signal events in each energy and time bin. In this case, the reference distribution also changes with time as seen in Figure 48, hence the fitting procedure should be applied for each energy and time intervals. This raises an issue, the number of events for each time and energy interval is reduced compared to the previous analysis, which in turn makes the shape of the distributions more irregular and not well described by a Novo function.

To solve this issue, a different approach of the Template-fit was adopted. The reference distribution is taken directly from the data sample, fitted using histograms. This method better take into account the irregularities of the distributions being more sensitive to the definition of the templates used, since different definitions will provide slightly different templates and event numbers. In this case, different definitions were used. The definition of the samples are given in Table 2.

All possible combinations of the template definitions were used to fit the data, meaning that 144 fits (12 electron templates \times 12 proton templates) were performed for

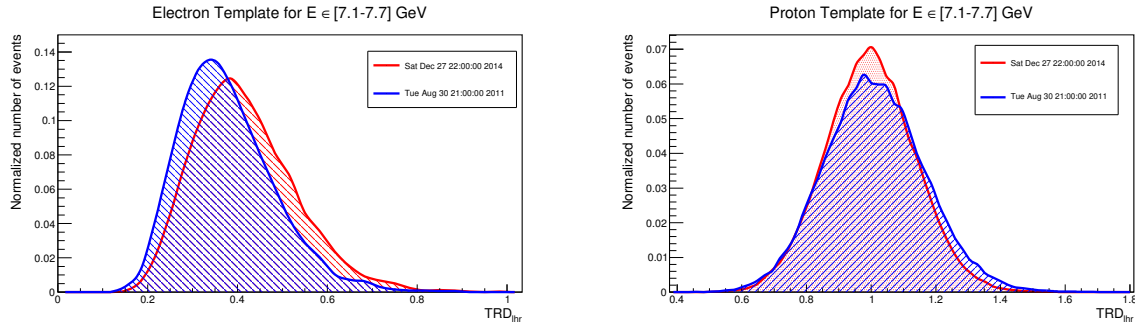


Figure 48 – Reference distribution of TRD_{lhr} for 2 different time intervals for both electron (**Left**) and proton (**Right**) distributions, for the energy interval of $[7.1-7.7]$ GeV.

Source: By the author

Table 2 – Definition of the reference templates for electrons and protons.

	Electrons	Protons
$ECAL_{BDT}$	$> x ; x \in \{0.1, 0.2, 0.25, 0.3\}$,	$< x ; x \in \{-0.4, -0.5, -0.6, -0.7\}$
$E/ R $	$> x ; x \in \{0.0, 0.5, 0.75\}$	$< x ; x \in \{0.0, 0.5, 0.75\}$
R sign	-	+

Source – By the author.

each time and energy intervals. An example of the result is shown in Figure 49 for both electrons and positrons.

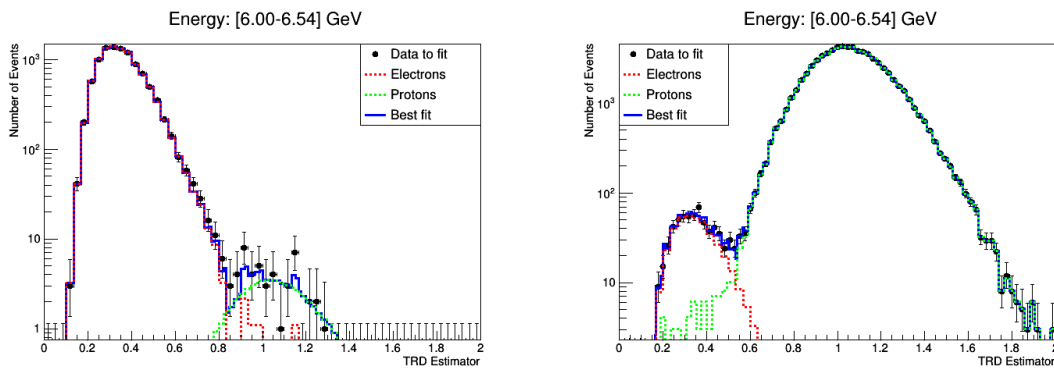


Figure 49 – Time dependent fit example on data for both electrons (**Left**) and positrons (**Right**), for the energy interval of $[6.00-6.58]$ GeV in the period of May 13th to June 9th, 2013

Source: By the author

Due to the many combinations, not every definition results in a good fit. To define the number of events used in the analysis, the best first 15 fits with the best χ^2 -distribution are considered. The resulting number is the mean value of the 15 definitions. An example of the distribution of the best 15 fits are given in Figure 50

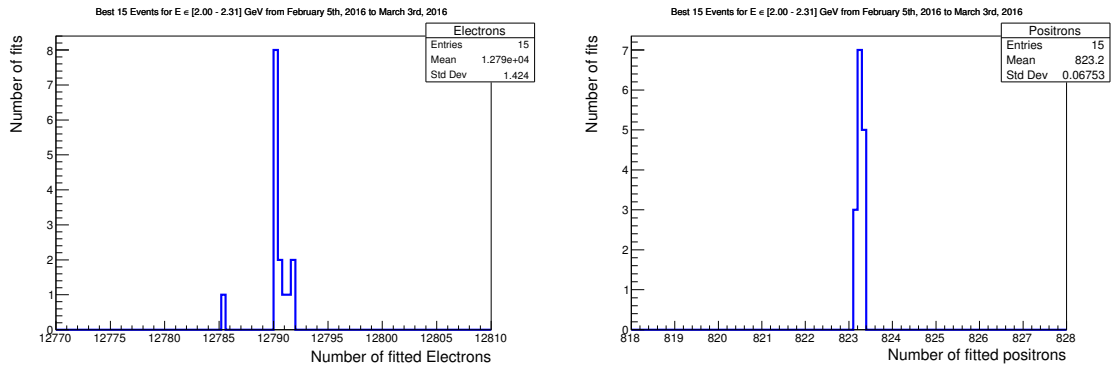


Figure 50 – Number of events for the best 15 fits for electrons (**Left**) and positrons (**Right**), for the energy interval of [2.00 - 2.31] GeV in the period of February 5th, 2016 to March 3rd, 2016

Source: By the author

3.2 Time dependent exposure time

The same procedure to get the exposure time is applied for each Bartels rotation. One example is shown in Figure (51).

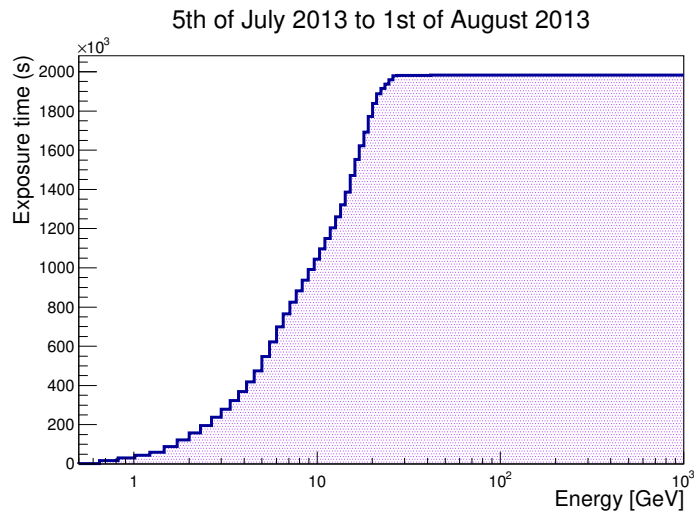


Figure 51 – Exposure time example for a Bartels rotation period.

Source: By the author

The behaviour closely remembers the one observed in Figure 30. The main difference is in the absolute value above around 30 GeV. The efficiency of the exposure time is studied by comparing the value of the distribution plateau and dividing by 27 days. This result is shown in Figure (52).

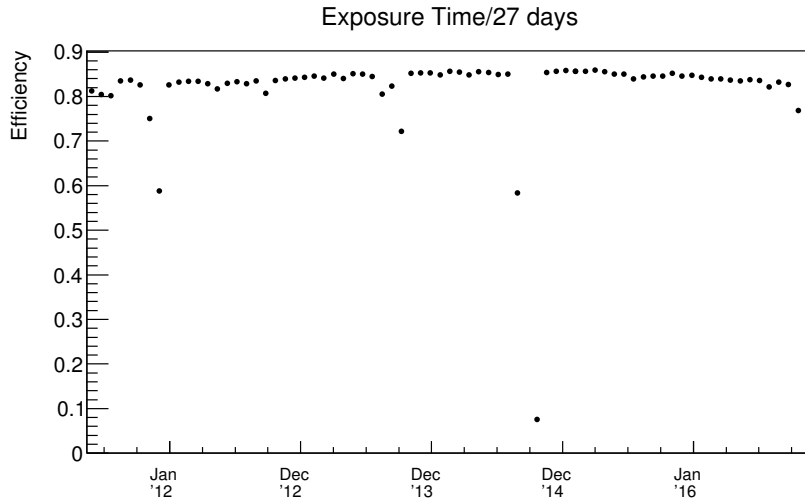


Figure 52 – Exposure time efficiency for each Bartels rotation.

Source: By the author

The Exposure time is stable and around 80% of the total time for every time bin. The effect of detector operations and sub-detector maintenance are visible during some time intervals, and the corresponding events are not considered in this analysis.

3.3 Time dependent effective acceptance

The official AMS-02 Monte Carlo simulation that is used in the present analysis to estimate the detector acceptance and the correction obtained from the data-MC comparison does not take into account the time evolution of the detector efficiencies. The time dependence of the effective acceptance will be discussed in this section. The naive approach for this result would be to calculate the efficiencies for each cut used in each time and energy intervals. However, due to the limited number of events in each Bartels rotation, the definition of a control sample of electrons from the data would be affected by severe statistical fluctuations. This control sample also has to be as pure as possible to avoid any bias in the correction. Unfortunately, if the selection criteria from the control sample are too tight, the number of events left to use would be too small to have a robust result. To avoid this conundrum, a different strategy to reduce the statistical fluctuations is applied. The cuts used in the preselection are divided into 3 categories:

- **Time independent:** Cuts in which there is no time dependence throughout the whole period of analysis
- **Time dependent cuts uncorrelated with energy:** Cuts that do have a time component but this component is uncorrelated with the energy behaviour.
- **Time dependent cuts correlated with energy:** Cuts which the time dependency is correlated with the energy.

The variable $\rho(\Delta E, \Delta t)$ defined in Equation 3.2 is used to assess the time dependence of each individual selection criteria.

$$\rho(\Delta E, \Delta t) = \frac{\epsilon(\Delta E, \Delta t)}{\epsilon_t(\Delta E)} \quad (3.2)$$

Where $\epsilon_t(\Delta E)$ means the mean value of $\epsilon(\Delta E, \Delta t)$ averaged over time. If the cut is time independent:

$$\epsilon(\Delta E, \Delta t) = \epsilon_t(\Delta E) \Rightarrow \rho(\Delta E, \Delta t) = 1 \quad (3.3)$$

hence, the distribution of $1 - \rho(\Delta E, \Delta t)$ should follow a normal distribution centred around 0. For each individual selection criteria the ρ variable was computed and the distribution of $1 - \rho(\Delta E, \Delta t)$ was obtained and fit to a gaussian. Six cuts, whose distributions are shown in Figures 53, 54 and 55, belong to this category, namely:

- Trigger efficiency
- Ecal Shower existence
- Track extrapolation inside ECAL
- Track-ECAL matching
- TOF β
- Charge cut

For these cuts there is no time dependence and the data/MC correction is taken from 2.6

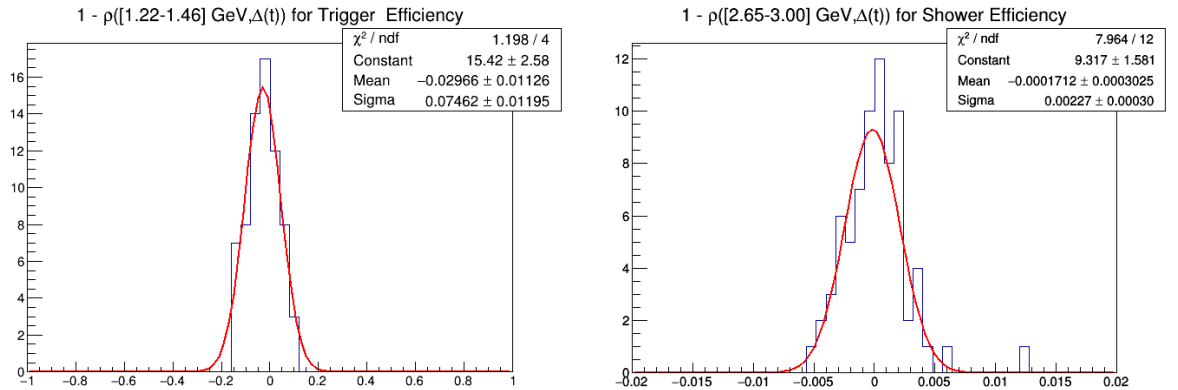


Figure 53 – $(1 - \rho)$ distribution example for Trigger (**Left**) and ECAL (**Right**) efficiencies for the energy interval of [1.22 GeV - 1.46 GeV] and [2.65 GeV - 3.00 GeV] respectively. Gaussian fit performed in both distributions.

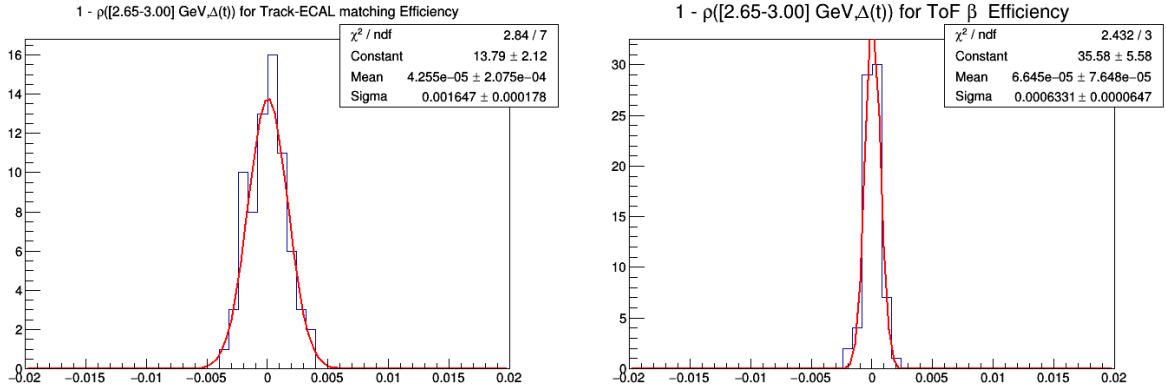


Figure 54 – $(1 - \rho)$ distribution example for Track-ECAL matching (**Left**) and β (**Right**) efficiencies for the energy interval of [2.65 GeV - 3.00 GeV]. Gaussian fit performed in both distributions.

Source: By the author

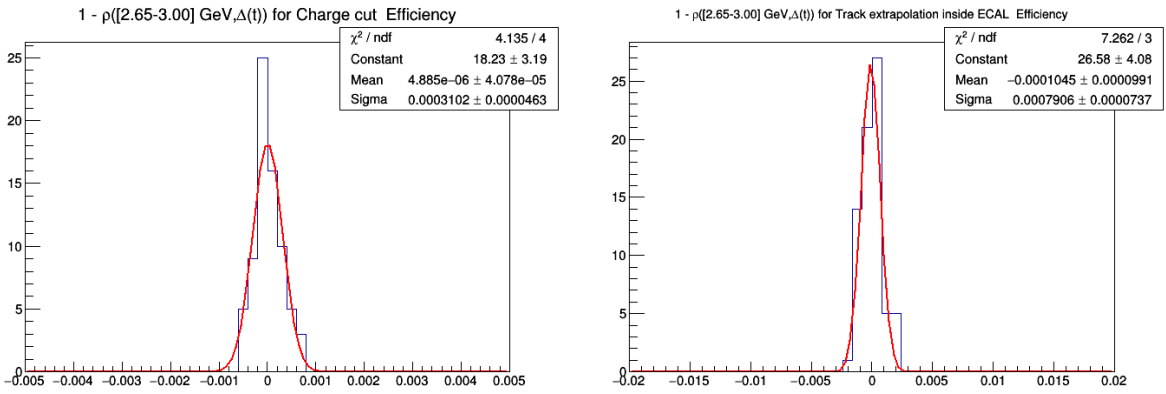


Figure 55 – $(1 - \rho)$ distribution example for Charge (**Left**) and Track extrapolation (**Right**) efficiencies for the energy interval of [2.65 GeV - 3.00 GeV]. Gaussian fit performed in both distributions.

Source: By the author

In the case of time dependent cuts uncorrelated with energy, the efficiency can be further separated as:

$$\epsilon(\Delta E, \Delta t) = f(\Delta E)g(\Delta t) \quad (3.4)$$

taking the mean value of $\rho(\Delta E, \Delta t)$ with respect to time ($\rho_t(\Delta E)$):

$$\rho_t(\Delta E) = g_t \frac{f(\Delta E)}{\epsilon_t(\Delta E)} = \frac{\epsilon_t(\Delta E)}{\epsilon_t(\Delta E)} = 1 \quad (3.5)$$

taking the mean with respect to the energy ($\rho_E(\Delta t)$):

$$\rho_E(\Delta t) = f_E \frac{g(\Delta t)}{\epsilon_{E,t}} = \frac{\epsilon_E(\Delta t)}{\epsilon_{E,t}} \quad (3.6)$$

Combining equations (3.6) and (3.5) results:

$$\epsilon(\Delta E, \Delta t) = f(\Delta E)g(\Delta t) = \frac{\epsilon_E(\Delta t)\epsilon_t(\Delta E)}{\epsilon_{E,t}} \quad (3.7)$$

where $\epsilon_{E,t}$ is the mean value of $\epsilon(\Delta E, \Delta t)$ taken with respect to both energy and time. This means that instead of using only the events for a particular energy and time interval, the efficiency can be described as the product of the mean values of the efficiencies normalised by its total mean value. The cuts in this category are the ones related to the Tracker as observed in Figure (56). This behaviour is expected because during the 5 years of operation, the track reconstruction method undergone modifications, mostly in the beginning of the experiment.

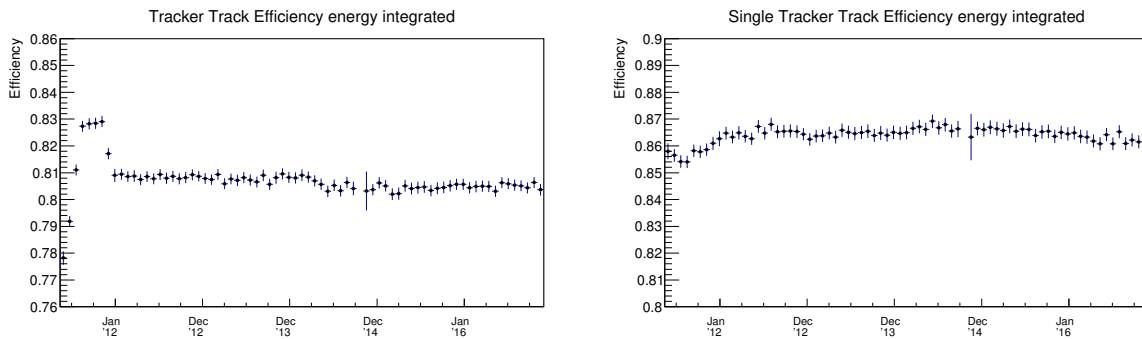


Figure 56 – Tracker Track reconstruction efficiency (left) and Single Tracker track (right) efficiencies energy integrated as a function of time. Both distributions show a time dependent component that is independent of energy.

Source: By the author

The only cut which the time and energy dependencies are correlated is the number of TRD hits and Helium background suppression efficiency, shown in Figure (57). In this case, nothing can be done to increase the number of events for each bin and the correction is performed by considering the efficiencies for each time and energy. An example of each correction is shown in Figure 58 for the time period of 5th of July up to 1st of August. The resulting correction applied is the multiplication of each correction.

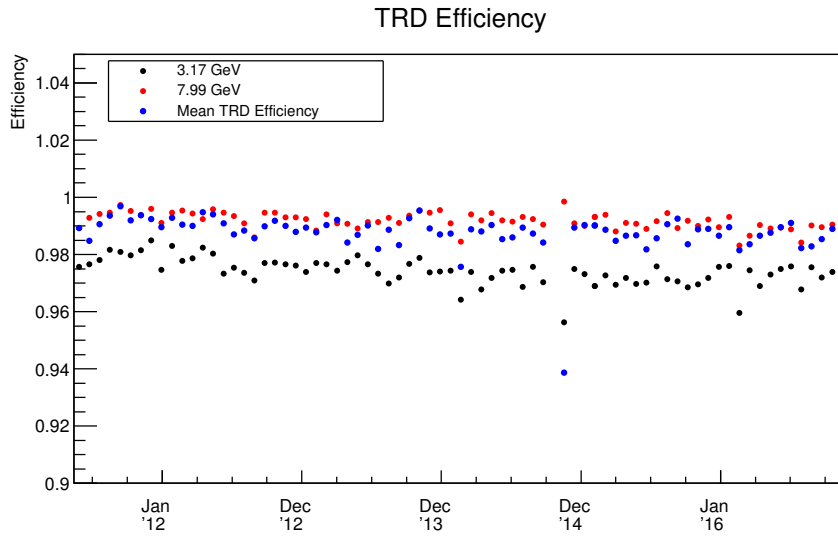


Figure 57 – TRD Efficiency as a function of time for different energies.

Source: By the author

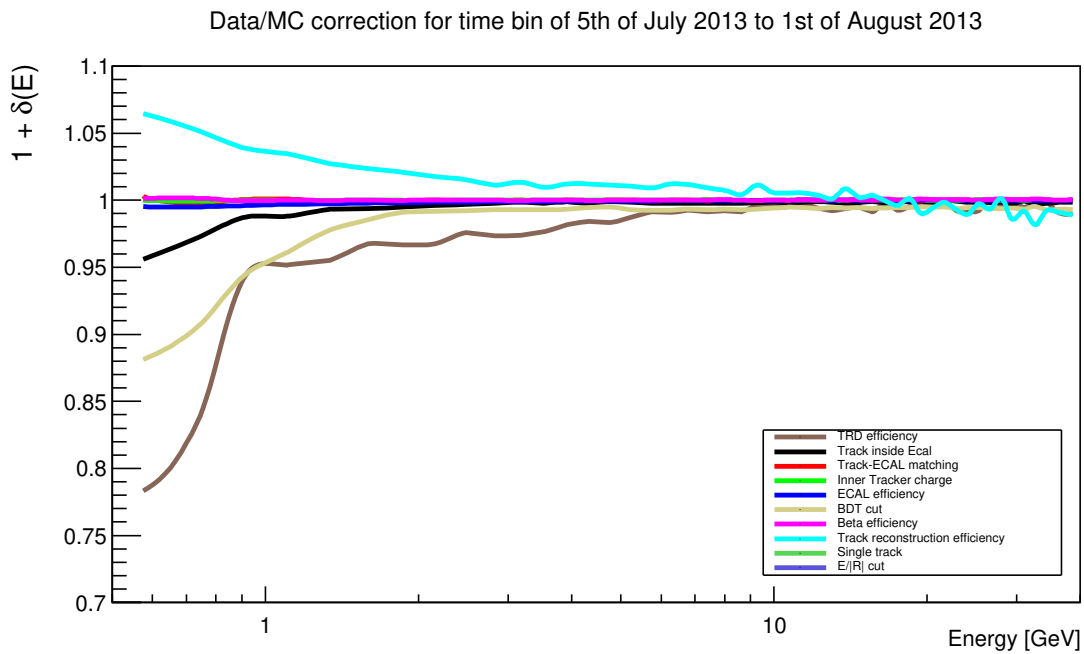


Figure 58 – Correction of each selection criteria in the time interval of 5th of July up to 1st of August as a function of the energy

Source: By the author

3.4 Results

The time dependent electron and positron fluxes, normalised to their respective time-average value, are shown in Figures 59 and 60 as a function of energy. Each line corresponds to a flux measurement for a given Bartels rotation from May 2011 up to November 2016. Variations up to 85% and 70% for electrons and positrons respectively are observed, decreasing in magnitude as the energy increases. Electrons and positrons do not show the same time dependence. Even though both fluxes increase up to November 2012, after that, the positron flux decreases up to January 2014 while the electron kept decreasing further up to March 2015, more than 1 year apart. Since their minimum value, both fluxes start to increase until the end of the analysis. The last positron flux increased up to its highest point (light blue line), while electrons stopped around the same value of the average (yellow line).

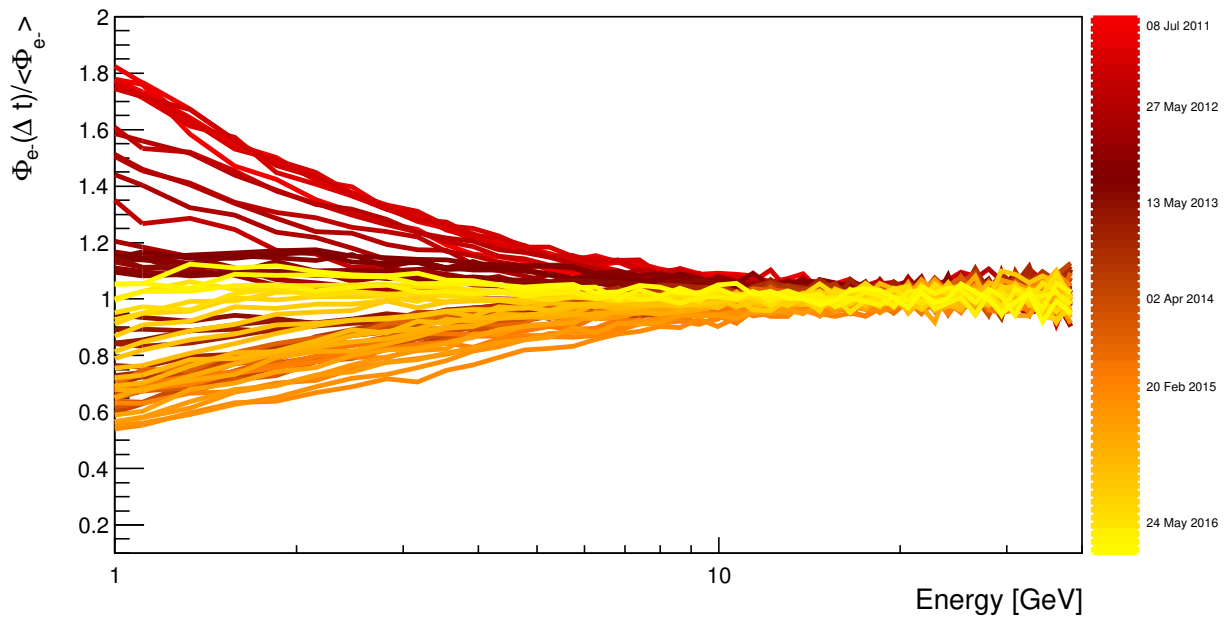


Figure 59 – Time dependent electron flux normalised to the average value as a function of energy. Each line represent one flux measurement for a given time bin.

Source: By the author

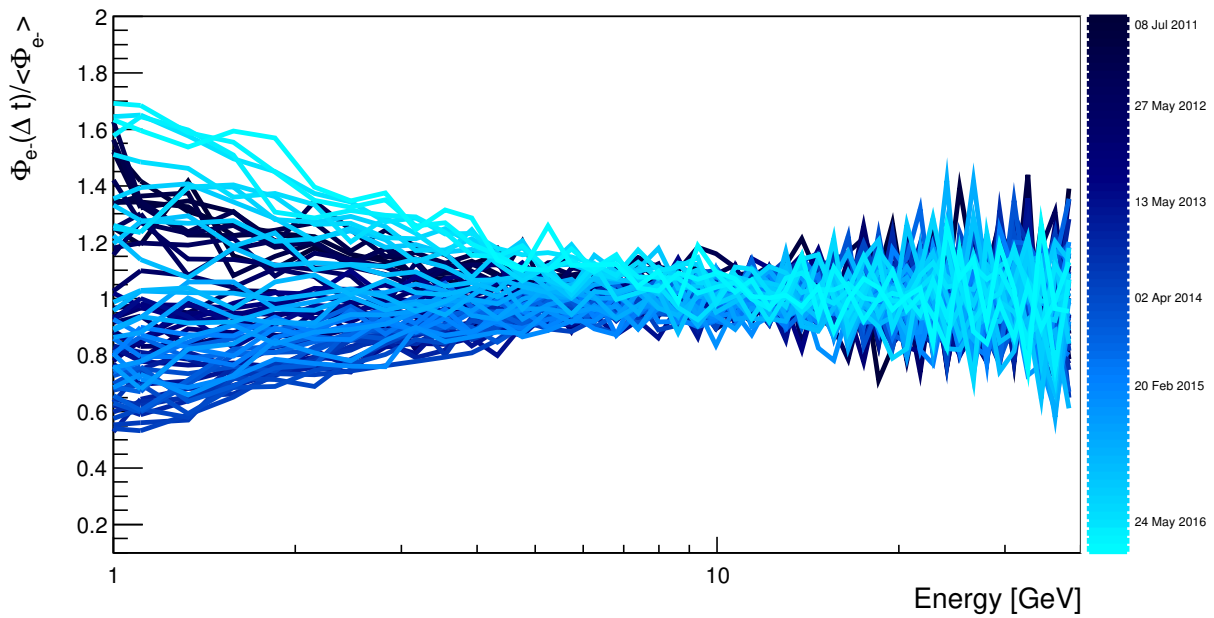


Figure 60 – Time dependent positron flux normalised to the average value as a function of energy. Each line represent one flux measurement for a given time bin.

Source: By the author

3.5 Result interpretation

The data taking period considered for the analysis represents a fraction of the current solar cycle, the number 24th since 1755, which began in January 2008. The first half of the cycle is characterised by the increase in solar activity, as observed in Figure 61 showing the number of sunspots as a function of time.

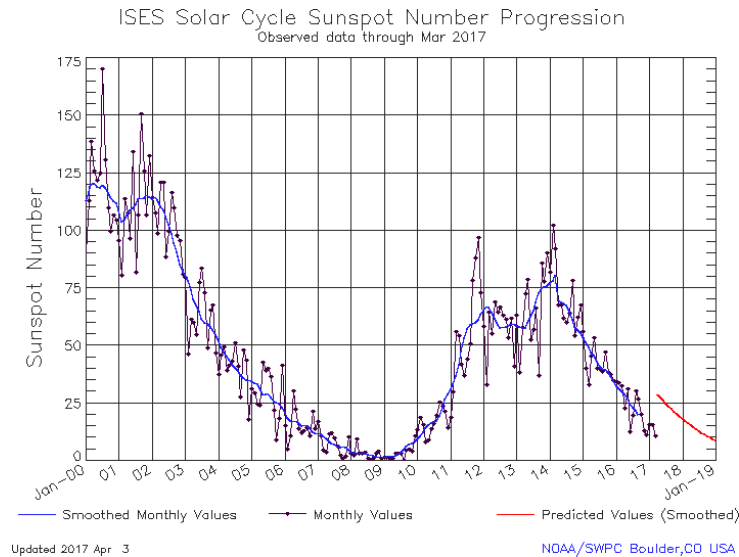


Figure 61 – Monthly measurement of solar cycle 24 by NOAA/Space Weather Prediction Center

Source: [SPACE WEATHER PREDICTION CENTER](#)⁷²

Around the same time of the maximum of solar activity, in October 2013,⁷³ the Sun's magnetic field changes polarity, going from negative to positive polarity ($A < 0$ to $A > 0$) as seen in Figure 62*.

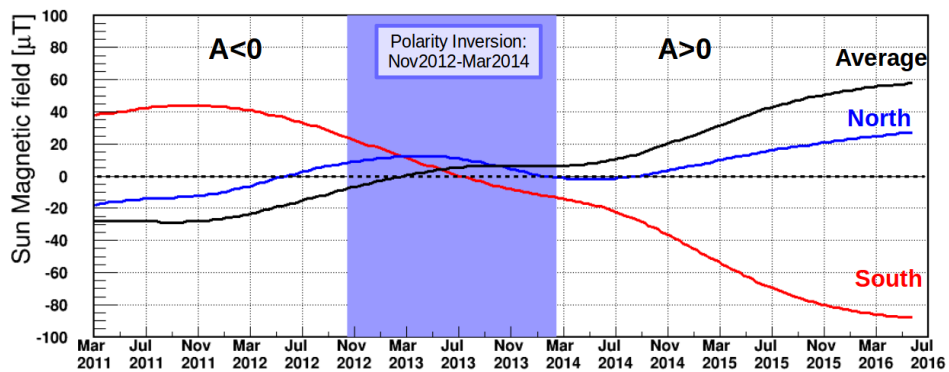


Figure 62 – Sun's magnetic field polarity as a function of time.

Source: C. Consolandi (2016) (Verbal information).

* Presentation given by C. Consolandi during an AMS-02 analysis meeting, CERN.

The equation that describes the propagation of CRs in the heliosphere is given by Parker's equation.⁷⁴

$$\frac{\partial f}{\partial t} = -\vec{V}_{sw} \cdot \vec{\nabla} f + \vec{\nabla} \cdot (K \cdot \vec{\nabla} f) + \frac{1}{3} \vec{\nabla} \cdot \vec{V}_{sw} \frac{\partial f}{\partial \ln R} + Q \quad (3.8)$$

where f is the CR phase space density, K the diffusion tensor. Equation 3.8 takes into account 5 different physical phenomena: convection and drift (first term on the right hand side), diffusion (second term), adiabatic energy losses (third term), and CR sources (final term). For the range of magnetic field strengths observed at Earth, the source term can be safely ignored for CRs with $E > 0.5$ GeV. Additionally, for the energy range of this analysis, adiabatic energy losses dominate. Positive and negative charged particles behave differently under different polarities of the Sun's magnetic field. During periods of positive polarity ($A > 0$), a positive charged particle that originates from the polar regions outside the Heliosphere can rather directly and effectively propagate to the location of Earth, suffering only modest energy losses. In contrast, during periods of negative polarity ($A < 0$), positive charged particles travel toward the inner Solar System largely through regions near the plane of the Solar System, where their movement is dominated by drift along the heliospheric current sheet, i.e, the surface across which the polarity of the Sun's magnetic field changes. A depiction of this behaviour is shown in Figure 63. A more detailed study is given by⁷⁵

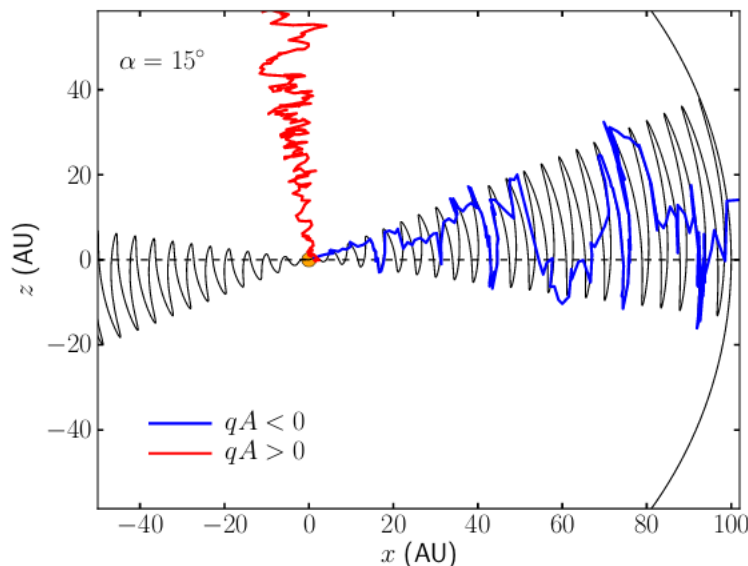


Figure 63 — Depiction of CR propagation in the Solar system. In the negative polarity, positively charged CRs drift along the heliospheric current sheet (shown as the solid blue line for a tilt angle of $\alpha = 15^\circ$), and move across layers of this sheet via diffusion. Positively charged particles diffuse more directly during periods of positive polarity.

Although a detailed description of the current sheet during the Sun's polarity reversal is difficult, a difference in behaviour of the fluxes should be expected and emphasised during this event, since the current sheet gets more wavy. Being this the case, an example of the ratio of the electron and positron fluxes is shown in Figure 64. The ratio presents 3 different regions. The first region is flat. This behaviour continues up to 2 months after the polarity reversal, in which a steady increase of the ratio is observed. At the beginning of 2015 the behaviour appears to change again to the flat regime.

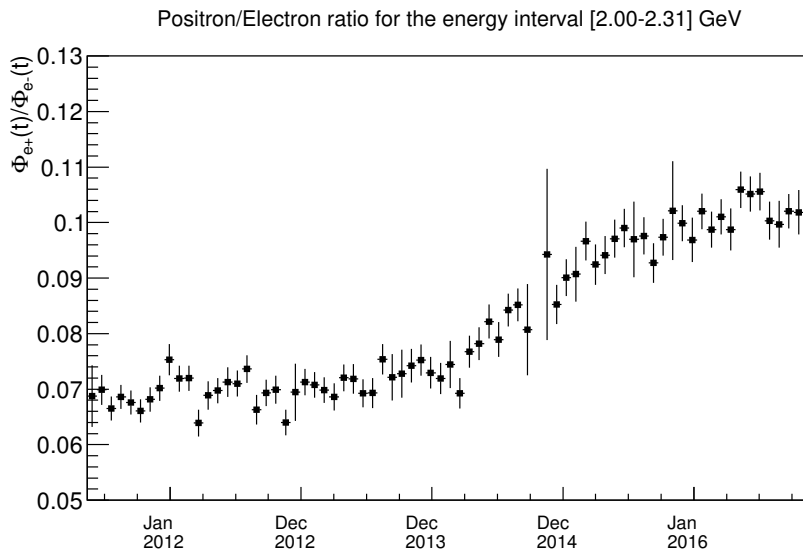


Figure 64 — Ratio of positron and electron fluxes for the energy interval of [2.00-2.31] GeV. 3 regions can be defined in which the ratio is flat, an increasing function of time and starts to get flat once more.

Source: By the author.

This behaviour is explained by the different time the electron and positron fluxes take to reach their minima. Before the positron flux reach the minimum value, both have the same time dependence, hence the ratio is flat. The Electron flux keep decreasing for a longer period of time, while the positron flux starts to increase. This region results in the increase of the ratio until the electron flux also reach the minimum. After that, both positron and electron fluxes increase in the same rate, which in turn results in a flat ratio. To determine the time the breakpoints happen, the ratio of the electron and positron fluxes were fitted with a generic hyperbolic tangent defined as follows:

$$f(x) = \frac{1}{2} \left[(a + b) + (b - a) \tanh \left(\frac{t - t_0}{w} \right) \right] \quad (3.9)$$

where a and b are the asymptotes, t_0 the time the slope changes from increasing to decreasing, and w the width of the interval between the asymptotes, hence the times in which the function changes behaviour is $t_0 \pm w$. An example of the fit is given in Figure 65.

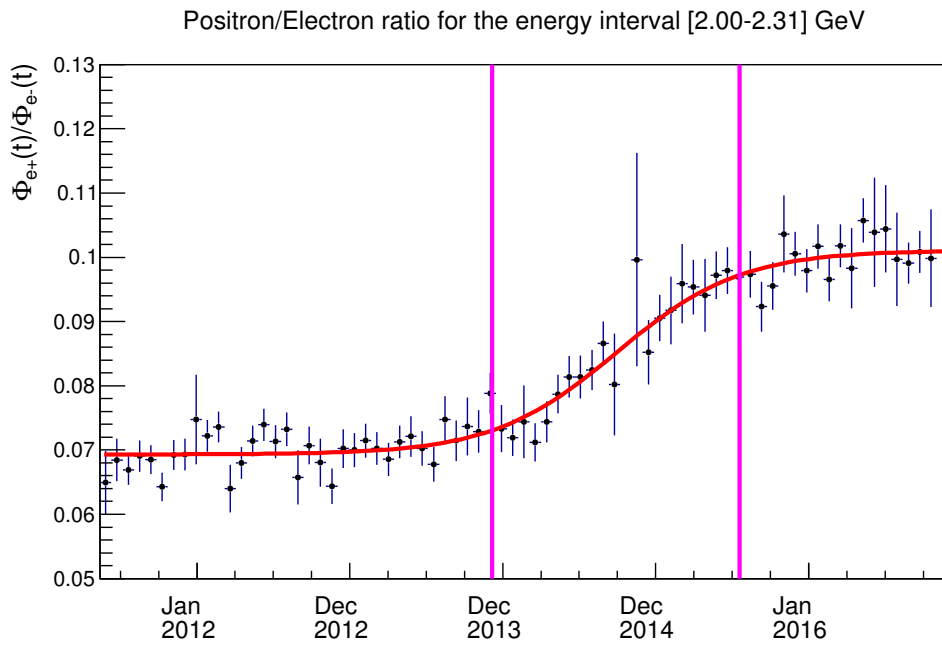


Figure 65 – Fit of the ratio of positron and electron fluxes for the energy interval of [2.00-2.31] GeV using the function defined in 3.9. Magenta lines represent the break times in which the change of behaviour happens.

Source: By the author.

The position of the 2 breaks as a function of energy until 5 GeV is given in Figure 66.

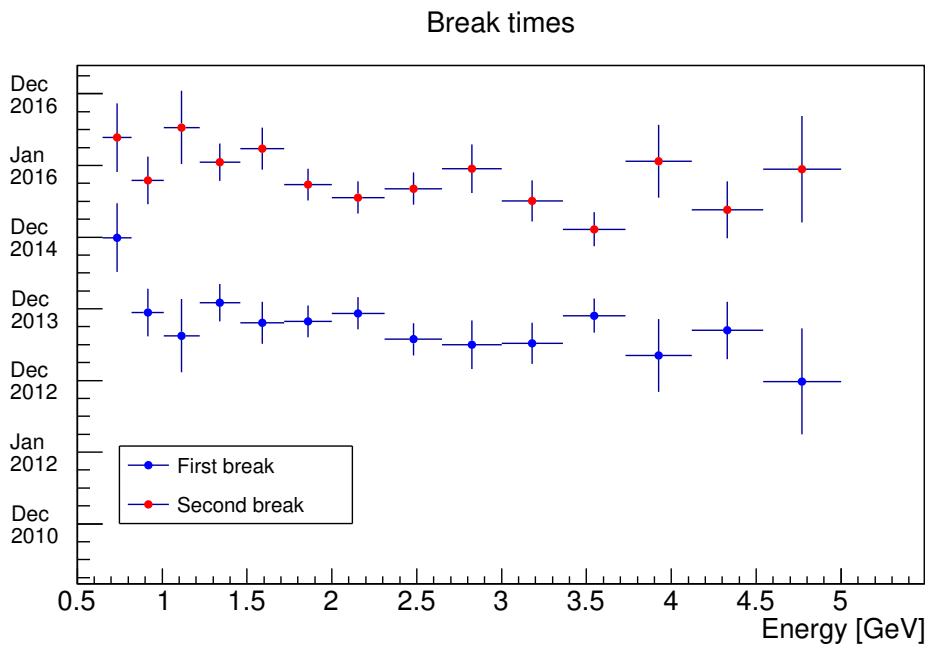


Figure 66 – First and second break times as a function of energy

Source: By the author.

Forbush decreases were also investigated. A Forbush decrease is a rapid decrease in the galactic cosmic ray intensity following a solar flare. The flare ejects clouds of plasma, constituted by electrons protons and Helium nuclei, through the corona of the sun. This plasma typically reaches the Earth within minutes after the event. Its magnetic field is intense enough to sweep some of the galactic cosmic rays away from Earth. Figure 67 shows for the energy interval [2.00-2.30] GeV the variation of the electron and positron fluxes normalised by the first Bartels rotation, as well the time periods which happened some of the strongest solar flares, the X-class, measured by the RHESSI experiment.⁷⁶ Not long after the solar flares, a local decrease of both fluxes is observed, characterising the Forbush decreases.

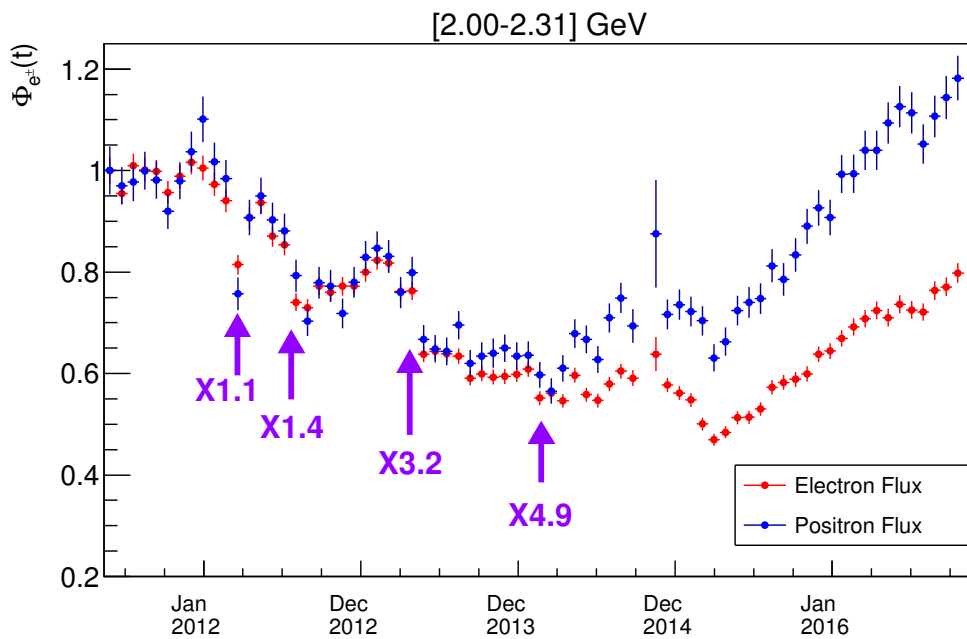


Figure 67 – Electron and Positron fluxes normalised by the first Bartels rotation for the energy interval [2.00-2.30] GeV. X-class flares measurements by RHESSI⁷⁶ also shown by the arrows in magenta.

Source: By the author

The effects of solar modulation gets weaker as the energy increases. After 10 GeV no difference in behaviour is observed between electrons and positrons, as seen in Figure 68

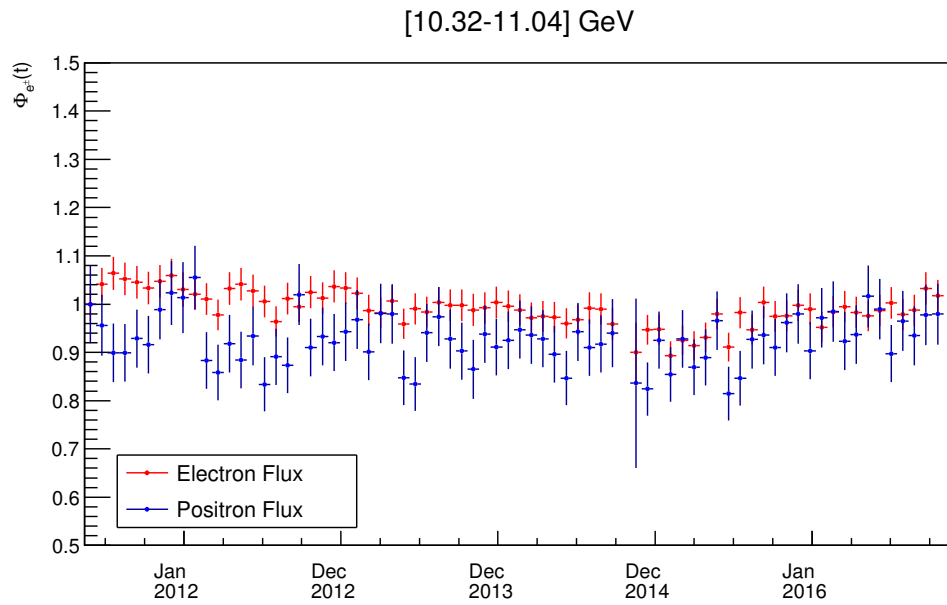


Figure 68 – Electron and Positron fluxes normalised by the first Bartels rotation for the energy interval [10.32-11.04] GeV.

Source: By the author

4 CONCLUSION

The measurement of the spectra of galactic cosmic rays electrons and positrons provides crucial information regarding the origin and propagation of cosmic rays. A correct understanding of galactic fluxes is fundamental for a correct interpretation of the measured data. Cosmic rays spectrum measured near Earth is significantly affected by the solar activity in the low energy part ($E < 20$ GeV). The solar activity changes in time, resulting in a time dependence of the measured fluxes. In this work, a new precise measurement of the electrons and positrons is performed. Using the data collected in the 66 months of the experiment, the energy spectrum was extended compared to the previous publication.³ The low energy behaviour was also studied as a function of time, focusing the analysis in the energy range of $[0.50 - 40.00]$ GeV. The increased data set provided a total of 74 time bins divided in intervals of 27 days, starting from May 2011 up to November 2016.

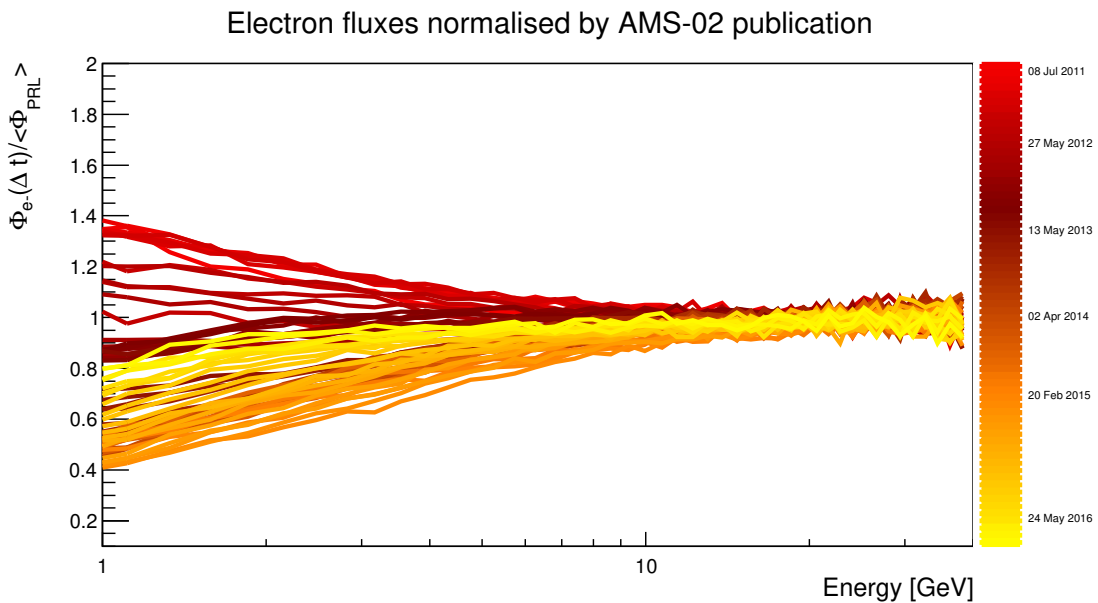


Figure 69 – Time dependent electron flux normalised by the published value as a function of energy. Each line represent one flux measurement for a given time bin.

Source: By the author

A decrease of the e^\pm fluxes with time has been observed which is consistent to solar activity in the period of the measurements. Indeed, up to the maximum in solar activity in April 2014, both electron and positron fluxes are decreasing with energy. The simultaneous measurement of electrons and positrons has also allowed to study differences of the solar modulation effects which are related only to the charge-sign of the particles. The main difference observed is a shift of the point in time in which the fluxes start to increase. The positron flux starts to increase around December 2013, while electrons keep decreasing until

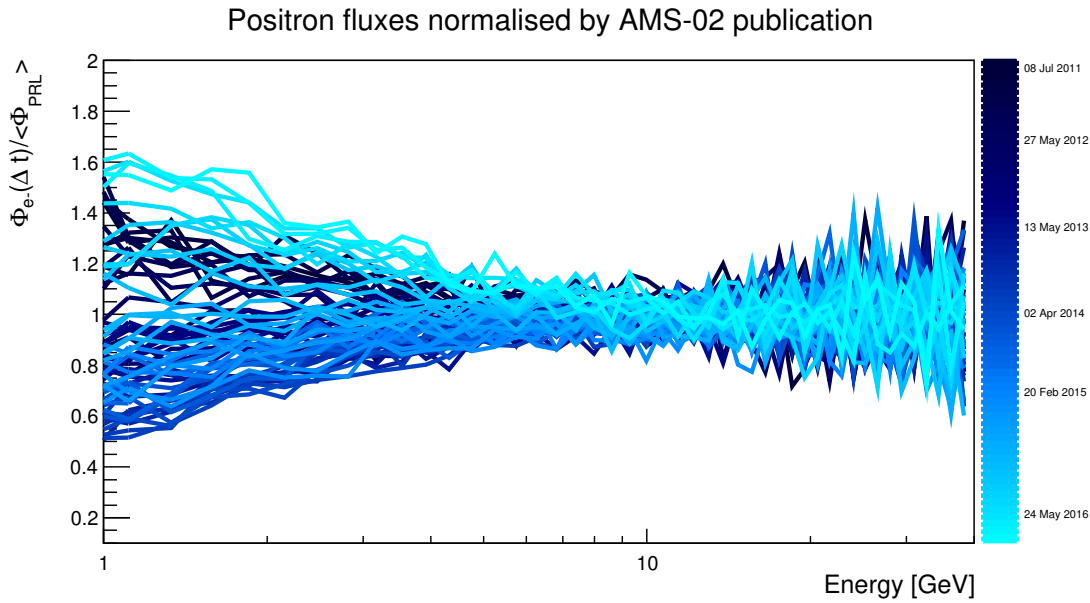


Figure 70 – Time dependent positron flux normalised by the published value as a function of energy. Each line represent one flux measurement for a given time bin.

Source: By the author

March 2015. This behaviour also explains the results the flux reconstruction of chapter 2. The electron flux was lower than the previous published paper, while the positron flux remained the same. Since the positron flux started to increase first, the increment compensates the remaining decrease after the data-set period used in the publication. On the other hand, the electron flux keeps decreasing for a longer period, which in turn results in the overall decrease observed. This is clear in Figures 69 and 70. Both electron and positron fluxes were normalised by the published flux by the AMS-02 collaboration. While the positron fluxes are more spread around 1, the electron fluxes are more concentrated in values smaller than 1.

The study of the time evolution of the flux ratio shows a clear charge sign dependent effect, that can be explained as a transition of an opposite heliospheric magnetic field polarity. Moreover, shorter timescale variations of the GCR spectra were observed due to impulsive solar events. Since AMS-02 will be taking data on the ISS for more than a decade, these and future data will allow deeper studies of GCR fluxes and their time evolution over an entire solar cycle, enabling a better understanding of the solar modulation effect and of the shorter timescale solar activity. The results presented in this report are consistent with the results of other analysis carried out within the collaboration in the same time , and they will be included in a forthcoming publication about the measurement of time dependent electron and positron fluxes with the AMS-02 experiment.

BIBLIOGRAPHY

- 1 AGUILAR, M. et al. First result from the Alpha Magnetic Spectrometer on the International Space Station: precision measurement of the positron fraction in primary cosmic rays of 0.5–350 GeV. **Physical Review Letters**, v. 110, n. 14, p. 141102, 2013.
- 2 AGUILAR, M. et al. Precision measurement of the (e++e-) flux in primary cosmic rays from 0.5 GeV to 1 TeV with the alpha magnetic spectrometer on the international space station. **Physical Review Letters**, v. 113, n. 22, p. 221102, 2014.
- 3 AGUILAR, M. et al. Electron and positron fluxes in primary cosmic rays measured with the Alpha Magnetic Spectrometer on the International Space Station. **Physical Review Letters**, v. 113, n. 12, p. 121102, 2014.
- 4 LONGAIR, M. S. **High Energy Astrophysics**. 3rd ed. Cambridge: Cambridge University Press, 2011. 880 p.
- 5 DELAHAYE, T. et al. Galactic secondary positron flux at the Earth. **Astronomy and Astrophysics**, v. 501, n. 3, p. 821–833, 2009.
- 6 BAADE, W.; ZWICKY, F. Remarks on super-novae and cosmic rays. **Physical Review**, v. 46, n. 1, p. 76–77, 1934.
- 7 FERMI, E. On the origin of the cosmic radiation. **Physical Review**, v. 75, n. 8, p. 1169–1174, 1949.
- 8 ALLEN, G. E. et al. Evidence of X-ray synchrotron emission from electrons accelerated to 40 TeV in the supernova remnant Cassiopeia A. **Astrophysical Journal Letters**, v. 487, n. 1, p. L97, 1997.
- 9 STRONG, A. W.; MOSKALENKO, I. V.; PTUSKIN, V. S. Cosmic-ray propagation and interactions in the galaxy. **Annual Review of Nuclear and Particle Science**, v. 57, n. 1, p. 285–327, 2007.
- 10 BECK, R. **Galactic and extragalactic magnetic fields**. 2009. Available from: <<https://arxiv.org/pdf/0810.2923.pdf>>. Accessible at: 23 Jan. 2015.
- 11 BRUNETTI, G. et al. Alfvénic reacceleration of relativistic particles in galaxy clusters: MHD waves, leptons and hadrons. **Monthly Notices of the Royal Astronomical Society**, v. 350, n. 4, p. 1174–1194, 2004.
- 12 BREITSCHWERDT, D.; SCHMUTZLER, T. **The dynamical signature of the ISM in soft X-rays – I. diffuse soft X-rays from galaxies**. 1999. Available from: <<https://arxiv.org/pdf/astro-ph/9902268.pdf>>. Accessible at: 23 Jan. 2016.
- 13 MAURIN, D. et al. Cosmic rays below $Z = 30$ in a diffusion model: new constraints on propagation parameters. **Astrophysical Journal**, v. 555, n. 2, p. 585–596, 2001.
- 14 STRONG, A. W.; MOSKALENKO, I. V.; PORTER, T. A. **The GALPROP cosmic-ray propagation code**. 2009. Available from: <<https://arxiv.org/pdf/0907.0559.pdf>>. Accessible at: 20 Jan. 2015.

- 15 EVOLI, C. et al. Cosmic-ray propagation with DRAGON2: I. numerical solver and astrophysical ingredients. **Journal of Cosmology and Astroparticle Physics**, n. 02, p. 15, 2017. doi:10.1088/1475-7516/2017/02/015.
- 16 PANOV, A. D. Electrons and positrons in cosmic rays. In: EUROPEAN COSMIC RAY SYMPOSIUM (ECRS 2012), 23., 2012, Moscow. **Proceedings...** Moscow: ECRS, 2013.
- 17 POTGIETER, M. S. Solar modulation of cosmic rays. **Living Reviews in Solar Physics**, v. 10, 2013. doi:10.12942/lrsp-2013-3.
- 18 PARKER, E. N. Dynamics of the interplanetary gas and magnetic fields. **Astrophysical Journal**, v. 128, p. 664, 1958. doi: 10.1086/146579.
- 19 NATIONAL AERONAUTICS AND SPACE ADMINISTRATION. **Voyager- the interstellar mission**. 1977. Available from: <<https://voyager.jpl.nasa.gov/>>. Accessible at: 10 Jan. 2017.
- 20 GLEESON, L. J.; AXFORD, W. I. Solar modulation of galactic cosmic rays. **Astrophysical Journal**, v. 154, p. 1011, 1968.
- 21 DAVIS, A. J. et al. The evolution of galactic cosmic ray element spectra from solar minimum to solar maximum: Ace measurements. In: INTERNATIONAL COSMIC RAY CONFERENCE (ICRC2001), 27., 2001, Hamburg. **Proceedings...** Hamburg: ICRC, 2001.
- 22 KOPP, G.; LAWRENCE, G. The Total Irradiance Monitor (TIM): Instrument Design. In: **The Solar Radiation and Climate Experiment (SORCE)**. New York: Springer, 2015. p. 91–109.
- 23 POTGIETER, M. The charge-sign dependent effect in the solar modulation of cosmic rays. **Advances in Space Research**, v. 53, n. 10, p. 1415–1425, 2014.
- 24 MACCIONE, L. Low energy cosmic ray positron fraction explained by charge-sign dependent solar modulation. **Physical Review Letters**, v. 110, n. 8, p. 081101, 2013.
- 25 LOWES, F.; J., F. Introduction to geomagnetism. **Physics of the Earth and Planetary Interiors**, v. 33, n. 4, p. 336–337, 1983.
- 26 KEYSER, J. D. et al. Magnetopause and boundary layer. **Space Science Reviews**, Berlin: Springer Netherlands, p. 231–320, 2005.
- 27 NATIONAL GEOSPATIAL-INTELLIGENCE AGENCY. **The world magnetic model**. 2015. Available from: <<https://ngdc.noaa.gov/geomag/WMM/>>. Accessible at: 23 Mar. 2016.
- 28 ALLEN, J. A. van. The geomagnetically trapped corpuscular radiation. **Journal of Geophysical Research**, v. 64, n. 11, p. 1683, 1959.
- 29 STØRMER, C. The polar aurora. **Quarterly Journal of the Royal Meteorological Society**, v. 82, n. 351, p. 115, 1956.
- 30 ADRIANI, O. et al. Observation of an anomalous positron abundance in the cosmic radiation. **Nature**, v. 458, n. 7238, p. 607–609, 2008.

-
- 31 BOUDAUD, M. et al. **The pinching method for galactic cosmic ray positrons: implications in the light of precision measurements.** 2016. Available from: <https://arxiv.org/pdf/1612.03924.pdf>. Accessible at: 21 Jan. 2017.
- 32 HOOPER, D.; BLASI, P.; SERPICO, P. D. Pulsars as the sources of high energy cosmic ray positrons. **Journal of Cosmology and Astroparticle Physics**, v. 2009, n. 01, p. 025–025, 2009.
- 33 BERGSTROM, L. Dark matter and imaging air Cherenkov arrays. **Astroparticle Physics**, v. 43, p. 44–49, 2013.
- 34 BOUDAUD, M. et al. **A new look at the cosmic ray positron fraction.** 2015. Available from: <https://arxiv.org/pdf/1410.3799.pdf>. Accessible at: 23 Jan. 2017.
- 35 TING, S. The Alpha Magnetic Spectrometer on the International Space Station. **International Journal of Modern Physics E**, v. 21, n. 08, p. 1230005, 2012.
- 36 BINDI, V. et al. The scintillator detector for the fast trigger and time-of-flight (TOF) measurement of the space experiment AMS-02. **Nuclear Instruments and Methods in Physics Research A**, v. 623, n. 3, p. 968–981, 2010.
- 37 BASILI, A. et al. The TOF-ACC flight electronics for the fast trigger and time of flight of the AMS-02 cosmic ray spectrometer. **Nuclear Instruments and Methods in Physics Research A**, v. 707, p. 99–113, 2013. doi:10.1016/j.nima.2012.12.089.
- 38 BINDI, V. et al. The ams-02 time of flight (tof) system: construction and overall performances in space. In: INTERNATIONAL COSMIC RAY CONFERENCE (ICRC2013), 33., 2013, Rio de Janeiro. **Proceedings...** Rio de Janeiro: ICRC, 2013.
- 39 BINDI, V. et al. Calibration and performance of the AMS-02 time of flight detector in space. **Nuclear Instruments and Methods in Physics Research A**, v. 743, p. 22–29, 2014.
- 40 CHERRY, M. L. et al. Transition radiation from relativistic electrons in periodic radiators. **Physical Review D**, v. 10, n. 11, p. 3594–3607, 1974.
- 41 CHERRY, M. L.; MÜLLER, D. Measurements of the frequency spectrum of transition radiation. **Physical Review Letters**, v. 38, n. 1, p. 5–8, 1977.
- 42 ANDRONIC, A.; WESSELS, J. Transition radiation detectors. **Nuclear Instruments and Methods in Physics Research A**, v. 666, p. 130–147, 2012. doi:10.1016/j.nima.2011.09.041.
- 43 BRUCH, T.; WALLRAFF, W. The anti-coincidence counter shield of the AMS tracker. **Nuclear Instruments and Methods in Physics Research A**, v. 572, n. 1 SPEC. ISS., p. 505–507, 2007.
- 44 DOETINCHEM, P. von et al. The AMS-02 anticoincidence counter. **Nuclear Physics B**, v. 197, n. 1, p. 15–18, 2009.
- 45 AHLEN, S. et al. An antimatter spectrometer in space. **Nuclear Instruments and Methods in Physics Research A**, v. 350, n. 1-2, p. 351–367, 1994.

46 DURANTI, M. **Measurement of the atmospheric muon flux on ground with the AMS-02 Detector**. 2012. Thesis (PhD) — INFN, Perugia, Perugia, 2012.

47 ZUCCON, P. The AMS silicon tracker: construction and performance. **Nuclear Instruments and Methods in Physics Research A**, v. 596, n. 1, p. 74–78, 2008.

48 ZHANG, Z. et al. Stable and self-adaptive performance of mechanically pumped CO₂ two-phase loops for AMS-02 tracker thermal control in vacuum. **Applied Thermal Engineering**, v. 31, n. 17, p. 3783–3791, 2011.

49 AMBROSI, G. et al. **Nuclei charge measurement with the AMS-02 silicon tracker**. 2016. Available from: <[http://inspirehep.net/record/1483710/files/PoS\(ICRC2015\)429.pdf](http://inspirehep.net/record/1483710/files/PoS(ICRC2015)429.pdf)>. Accessible at: 23 Jan. 2017.

50 SADAKAZU, H. Precision measurement of the proton flux with ams. In: INTERNATIONAL COSMIC RAY CONFERENCE (ICRC2013), 33., 2013, Rio de Janeiro. **Proceedings...** Rio de Janeiro: ICRC, 2013.

51 NATALE, S.; SCHAEEL, S. The ams-2 tracker alignment system: design and performance. In: INTERNATIONAL COSMIC RAY CONFERENCE (ICRC2009), 31., 2009, Lodz. **Proceedings...** Lodz: ICRC, 2013.

52 ZUCCON, P. Ams-02 track reconstruction and rigidity measurement. In: INTERNATIONAL COSMIC RAY CONFERENCE (ICRC2013), 33., 2013, Rio de Janeiro. **Proceedings...** Rio de Janeiro: ICRC, 2013.

53 AGUILAR-BENITEZ, M. et al. In-beam aerogel light yield characterization for the AMS RICH detector. **Nuclear Instruments and Methods in Physics Research A**, v. 614, n. 2, p. 237–249, 2010.

54 PEREIRA, R. The AMS-02 RICH detector: performance during ground-based data taking at CERN. **Nuclear Instruments and Methods in Physics Research A**, v. 639, n. 1, p. 37–41, 2011.

55 GRENOBLE, P. D. High precision measurement of the ams-rich aerogel refractive index with cosmic ray. In: INTERNATIONAL COSMIC RAY CONFERENCE (ICRC2013), 33., 2013, Rio de Janeiro. **Proceedings...** Rio de Janeiro: ICRC, 2013.

56 GIOVACCHINI, F. In-flight determination of the ams-rich photon yield. In: INTERNATIONAL COSMIC RAY CONFERENCE (ICRC2013), 33., 2013, Rio de Janeiro. **Proceedings...** Rio de Janeiro: ICRC, 2013.

57 ADLOFF, C. et al. The AMS-02 lead-scintillating fibres electromagnetic calorimeter. **Nuclear Instruments and Methods in Physics Research A**, v. 714, p. 147–154, 2013. doi:10.1016/j.nima.2013.02.020.

58 CADOUX, F. et al. The AMS-02 electromagnetic calorimeter. **Nuclear Physics B**, v. 113, n. 1, p. 159 – 165, 2002.

59 CERVELLI, F. et al. A reduced scale e.m. calorimeter prototype for the AMS-02 experiment. **Nuclear Instruments and Methods in Physics Research A**, v. 490, n. 1-2, p. 132–139, 2002.

-
- 60 VAGELLI, V. **Identification of positrons and electrons in the cosmic radiation with the electromagnetic calorimeter ECAL for the AMS-02 experiment.** 2011. Dissertation (Master) — Perugia University, Perugia, 2011.
- 61 BASARA, L. M. Energy calibration with mip in space and charge measurement with ams02 electromagnetic calorimeter. In: INTERNATIONAL COSMIC RAY CONFERENCE (ICRC2013), 33., 2013, Rio de Janeiro. **Proceedings...** Rio de Janeiro: ICRC, 2013.
- 62 GRINDHAMMER G.; PETERS, S. **The parameterized simulation of electromagnetic showers in homogeneous and sampling calorimeters.** 2000. Available from: <<https://arxiv.org/pdf/hep-ex/0001020.pdf>>. Accessible at: 15 Feb. 2015.
- 63 DI FALCO, S. Performance of the ams-02 electromagnetic calorimeter in space. In: INTERNATIONAL COSMIC RAY CONFERENCE (ICRC2013), 33., 2013, Rio de Janeiro. **Proceedings...** Rio de Janeiro: ICRC, 2013.
- 64 VECCHI, M.; WU, K.; CHANG, Y.-H. A 3-dimensional electromagnetic shower characterization and its application to ams-02 pointing capability. In: INTERNATIONAL COSMIC RAY CONFERENCE (ICRC2013), 33., 2013, Rio de Janeiro. **Proceedings...** Rio de Janeiro: ICRC, 2013.
- 65 LEO, W. R. **Techniques for nuclear and particle physics experiments : a how-to approach.** New York: Springer, 1994. 378 p.
- 66 ROE, B. P. et al. Boosted decision trees as an alternative to artificial neural networks for particle identification. **Nuclear Instruments and Methods in Physics Research A**, v. 543, n. 2-3, p. 577–584, 2005.
- 67 VERKERKE, W.; KIRKBY, D. **The RooFit toolkit for data modeling.** 2003. Available from: <<https://arxiv.org/pdf/physics/0306116.pdf>>. Accessible at: 10 Jan. 2016.
- 68 IKEDA, H. et al. Detailed test of the CsI(Tl) calorimeter for BELLE with photon beams of energy between 20 MeV and 5.4 GeV. **Nuclear Instruments and Methods in Physics Research A**, v. 441, n. 3, p. 401–426, 2000.
- 69 CHOUTKO, V.; the Ams Collaboration. Parallelization of the event processing in the AMS experiment. **Journal of Physics: conference series**, v. 219, n. 3, 2010.
- 70 LAFFERTY, G. D.; WYATT, T. R. Where to stick your data points: the treatment of measurements within wide bins. **Nuclear Instruments and Methods in Physics Research A**, v. 355, n. 2-3, p. 541–547, 1995.
- 71 BARTELS, J. Twenty-seven day recurrences in terrestrial-magnetic and solar activity, 1923–1933. **Journal of Geophysical Research**, v. 39, n. 3, p. 201, 1934.
- 72 SPACE WEATHER PREDICTION CENTER. **ISES solar cycle 24 sunspot number progression.** 2014. Available from: <<http://www.swpc.noaa.gov/products/solar-cycle-progression>>. Accessible at: 02 Dec. 2015.
- 73 SUN, X. et al. On polar magnetic field reversal and surface flux transport during solar cycle 24. **Astrophysical Journal**, v. 798, n. 2, p. 114, 2015.

74 PARKER, E. The passage of energetic charged particles through interplanetary space. **Planetary and Space Science**, v. 13, n. 1, p. 9–49, 1965.

75 CHOLIS, I.; HOOPER, D.; LINDEN, T. A predictive analytic model for the solar modulation of cosmic rays. **Physical Review Letters**, D93, n. 4, p. 43016, 2016.

76 LIN, R. P. et al. The reuven ramaty high-energy solar spectroscopic imager (RHESSI). **Solar Physics**, v. 210, n. 1-2, p. 3–32, 2002.